DISSERTATION

CHARACTERIZATION OF THE SCALE DEPENDENCE AND SCALE

INVARIANCE OF THE SPATIAL ORGANIZATION OF SNOW DEPTH FIELDS,

AND THE CORRESPONDING TOPOGRAPHIC, METEOROLOGIC, AND CANOPY

CONTROLS

Submitted by

Ernesto Trujillo-Gómez

Department of Civil and Environmental Engineering

UMI Number: 3374626

INFORMATION TO USERS

The quality of this reproduction is dependent upon the quality of the copy submitted. Broken or indistinct print, colored or poor quality illustrations and photographs, print bleed-through, substandard margins, and improper alignment can adversely affect reproduction.
In the unlikely event that the author did not send a complete manuscript and there are missing pages, these will be noted. Also, if unauthorized copyright material had to be removed, a note will indicate the deletion.
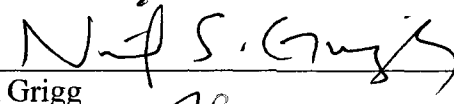
UMI®

COLORADO STATE UNIVERSITY

March 24, 2009

WE HEREBY RECOMMEND THAT THE DISSERTATION PREPARED UNDER

OUR SUPERVISION BY ERNESTO TRUJILLO-GOMEZ ENTITLED

CHARACTERIZATION OF THE SCALE DEPENDENCE AND SCALE

INVARIANCE OF THE SPATIAL ORGANIZATION OF SNOW DEPTH FIELDS,

AND THE CORRESPONDING TOPOGRAPHIC, METEOROLOGIC, AND CANOPY

CONTROLS BE ACCEPTED AS FULFILLING IN PART REQUIREMENTS FOR

THE DEGREE OF DOCTOR OF PHILOSOPHY

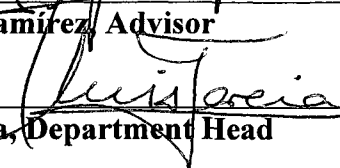Committee on Graduate Work

Kelly J. Elder

Neil S. Grigg

José D. Salas

Jorge A. Ramírez Advisor

Luis García, Department Head

ABSTRACT OF DISSERTATION

CHARACTERIZATION OF THE SCALE DEPENDENCE AND SCALE

INVARIANCE OF THE SPATIAL ORGANIZATION OF SNOW DEPTH FIELDS,

AND THE CORRESPONDING TOPOGRAPHIC, METEOROLOGIC, AND CANOPY

CONTROLS

The spatial organization of snow cover properties (e.g., density, depth, snow water equivalent (SWE)) and its dependence on scale are determined by precipitation patterns and the interaction of the snow pack with topography, winds, vegetation and radiative fluxes, among many others factors. The overarching objectives of this research are to characterize the spatial scaling properties and spatial organization of snow depth fields in several environments at scales between 1 m and 1000 m, and to determine how these properties are related to topography, vegetation, and winds. These objectives are accomplished through (a) the analysis of LIDAR elevation returns (filtered to bare ground/snow, and filtered to top of vegetation), elevation contours, and snow depth contours, (b) the analysis of synthetically generated profiles and fields of snow depth obtained using Fourier filtering and spectral techniques, and (c) simulations performed using a new cellular automata model for redistribution of snow by wind, that accounts for the small-scale interactions between the snow cover and the underlying topography, vegetation and winds patterns.

The analyses of the power spectral densities of snow depth show the existence of two distinct scaling regimes separated by a scale break located at scales of the order of meters

to tens of meters depending on the environment. The breaks separate a highly variable larger-scales interval from a highly correlated smaller-scales interval. Complementary analyses support the conclusion that the scaling behavior of snow depth is controlled by the scaling characteristics of the spatial distribution of vegetation height when snow redistribution by wind is minimal and canopy interception is dominant, and by the interaction of winds with features such as surface concavities and vegetation when snow redistribution by wind is dominant. Further analyses of the snow covers in two adjacent areas, one a sub-alpine forest and the other an alpine tundra, are used to show how and why differences in the controlling physical processes induced by variations in vegetation cover and wind patterns lead to the observed differences in the spatial organization between the snow depth fields of these environments. Using these observations together with synthetic snow depth profiles and fields generated with one- and two-dimensional spectral techniques, we show that the scale at which the break occurs increases with the separation distance between snow depth maxima. Finally, the cellular automata model developed here is used to show that the correlation structure of the snow depth fields becomes stronger as the amount of snow transported increases, while the probability distributions of the fields progress from a Gaussian distribution for small transport rates to positively skewed probabilities for high transport rates. The spatial patterns of the simulated fields, the anisotropy in the two-dimensional correlation structure, and the time progression of the snow cover resemble observations presented in previous studies. These simulation results are used to illustrate the controls that topography, vegetation, and winds have on the spatial organization of snow depth in wind-dominanted environments, and the progression of such properties throughout the accumulation period.

The results obtained in this research have important implications with respect to processes, measurement and model scales. The existence of a break in the scaling of snow depth at scales of the order of meters to tens of meters indicates a switch in the characteristics of the variability above and below the break. Within each scale interval, similar processes are controlling the variability. In forested environments, the location of the scale break is controlled by the separation between trees that induce local minima in the snow surface caused by canopy interception. In environments with significant wind redistribution of snow, the break is associated with the separation between snow drifts and depressions caused by the interactions of the blowing snow with topographic features (e.g., ridges and depressions) and vegetation. If the objective is to reveal small-scale processes such as vegetation interception by individual trees and wind interaction with small features such as surface concavities, trees and rocks, measurement and model scales should be selected within the high-frequency range. In this way, the details of the snow depth surface between the peaks can be revealed. If the objective is to represent the average effect of processes such as canopy interception of snowfall and snow redistribution due to wind, measurement and model scales should be selected within the low-frequency range. For practical purposes in hydrologic applications, accurate description of the small-scale interactions might not be necessary and the detailed information required to reproduce such processes might not be available. Model and measurement scales should be selected according to such objectives. Also, the simulation results show that the statistical properties of snow depth fields throughout the accumulation period in wind dominated environments depend on the transport volumes of snow, which are dependent on meteorological conditions (e.g., winds and

temperature). The inter-seasonal consistency of the spatial organization of snow covers in wind-dominated environments documented in several studies is conditioned to the consistency of wind patterns and wind transport potential. Years with differences in wind regimes and meteorological conditions (e.g., wind speeds and directions, temperatures) will exhibit differences in the spatial statistical properties of snow cover properties (e.g., depth and SWE). The magnitudes of the differences in the spatial statistical properties depend on the magnitudes of the differences in the meteorological conditions.

Ernesto Trujillo-Gómez

Department of Civil and Environmental Engineering

Colorado State University

Fort Collins, CO 80523

Spring 2009

ACKNOWLEDGMENTS

To those who picked me up and kept me going

TABLE OF CONTENTS

LIST OF TABLES

1   General Introduction

Spatial heterogeneity is one of the main features of snow covers in several environments [e.g., *Elder et al.*, 1991; *Blöschl and Kirnbauer*, 1992; *Luce et al.*, 1998]. The spatial organization of snow cover properties is determined by precipitation patterns and the interaction of the snow cover with several different factors such as topography, winds, vegetation, and short and long wave radiation, among others. The spatial patterns in the snow cover developed through these interactions influence melting patterns, soil moisture and vegetation patterns caused by the spatial heterogeneity in water availability. Better understanding of these interactions allows for improvements in snowmelt modeling [e.g., *Luce et al.*, 1998; *Liston and Sturm*, 1998; *Liston*, 1999; *Greene et al.*, 1999], interpolation of point measurements [e.g., *Elder et al.*, 1998; *Erxleben et al.*, 2002; *Erickson et al.*, 2005], downscaling of remote sensing data and model results [e.g., *McGinnis*, 2004; *Weitzenkamp et al.*, 2008], subgrid scale parameterizations [e.g., *Luce et al.*, 1999; *Liston*, 2004], and design strategies for measuring and monitoring snow properties [e.g., *Xu et al.*, 1993].

The spatial organization of snow covers has been studied through the analysis of ground measurements [e.g., *Evans et al.*, 1989; *Elder et al.*, 1991; *Shook and Gray*, 1996; 1997; *Kuchment and Gelfan*, 2001; *Erickson et al.*, 2005], remote sensing measurements [e.g., *Frezzotti et al.*, 2002], and results from snow models [e.g., *Liston and Sturm*, 1998; *Liston et al.*, 1999; *Liston et al.*, 2008]. The analyses of such datasets are limited by the spacing, extent and time continuity of the measurements, and by the spatial resolution

1

and accuracy of the models. In recent years, airborne LIght Detection and Ranging (LIDAR) started to be implemented for measuring the spatial structure of vegetation and snow given its capability for providing high-resolution measurements of these variables at spatial scales previously unavailable (~ 1 m). These high resolution measurements provide a unique opportunity to analyze the characteristics of the spatial heterogeneity of snow in environments with differences in the physiographic characteristics (e.g., topography and vegetation) and atmospheric conditions (e.g., winds, precipitation and temperatures).

The overarching objectives of the research documented here are to characterize the spatial scaling properties and spatial organization of snow cover properties in several environments at scales between 1 m and 1000 m, and to determine how these scaling properties and the spatial patterns observed are related to environmental variables such as topography, winds, and vegetation. These objectives are accomplished through (a) the analysis of LIDAR elevation returns (filtered to bare ground/snow, and filtered to top of vegetation), elevation contours, and snow depth contours collected as part of the National Aeronautics and Space Administration's (NASA) Cold Land Processes Experiment (CLPX) in 2003, (b) the analysis of synthetically generated profiles and fields of snow depth obtained using Fourier filtering and spectral techniques, and (c) simulations performed using a cellular automata model for redistribution of snow by wind, that accounts for the small-scale interactions between the snow cover and the underlying topography, vegetation and winds patterns, specifically developed as part of this research.

The document is organized into three main chapters, each consisting of a self-contained presentation in which specific components of the objectives presented above are addressed. The organization is as follows:

Chapter 2 reports on the analysis of the power spectral densities of high-resolution LIDAR measurements (~ 1 m) distributed within five 1-km^2 areas with significant differences in the characteristics of the spatial variability of the snow cover caused by differences in terrain, vegetation, and wind patterns. The results from the power spectral analysis are complemented by an analysis of maximum wind speeds and directions, and of the separation distance between peaks in the snow depth and vegetation height profiles. Also, the spectral characteristics (e.g., spectral exponents) are compared to wind patterns in search for a relationship between the two. Throughout the discussion section, the results and conclusions obtained in this study are compared to those obtained in the previous point data studies, emphasizing the new insights in the actual knowledge of the spatial variability of snow depth provided by the results presented that have not been previously discussed in the published literature.

In Chapter 3, the differences in the spatial organization of snow depth between a sub-alpine forest and an alpine tundra environment are described and explained based on the analysis of spatial distribution functions, correlation functions, and power spectral densities of high-resolution LIDAR measurements (~ 1 m) obtained within two adjacent 500 m x 500 m study areas located in the Colorado Rocky Mountains. Both of the areas are located in the Alpine ISA of the CLPX and present similar topographic characteristics (e.g., slope and aspect), but different vegetation characteristics and wind patterns. The analysis is complemented by the application of spectral techniques for generating

synthetic one-dimensional profiles and two-dimensional fields that reproduce the scaling characteristics (i.e., spectral exponents and scale breaks) observed in the snow depth fields.

In Chapter 4, a new cellular automata model is introduced for simulating the evolution of snow covers in wind dominated environments, with components that allow for the simulation of the interactions among the snow and topography, vegetation, and wind patterns. Several hypothetical scenarios are simulated to analyze the response of the system to variations in precipitation, topography, and winds. These simulations provide physically based evidence for the characteristics of the spatial organization of snow depth in such wind dominated environments. Also, through these simulations, it is possible to broaden the time frame examined, thus extending the analyses to other times in the season. The scales at which the model works are compatible with the available high resolution LIDAR measurements of snow depth analyzed in previous studies, facilitating the comparison of the model results with real observations.

A summary with general remarks is presented in Chapter 5, highlighting the most relevant findings of this research.

1.1 References

Blöschl, G., and R. Kirnbauer (1992), An analysis of snow cover patterns in a small alpine catchment, *Hydrolog. Process.*, *6*, 99-109.

Elder, K., J. Dozier, and J. Michaelsen (1991), Snow accumulation and distribution in an alpine watershed, *Water Resour. Res.*, *27*, 1541–1552.

Elder, K., W. Rosenthal, and R. Davis (1998), Estimating the spatial distribution of snow water equivalence in a montane watershed, *Hydrolog. Process.*, *12*(10-11), 1793-1808.

Erickson, T. A., M. W. Williams, and A. Winstral (2005), Persistence of topographic controls on the spatial distribution of snow in rugged mountain terrain, Colorado, United States, *Water Resour. Res.*, *41*, W04014, doi:10.1029/2003WR002973.

Erxleben, J., K. Elder, and R. Davis (2002), Comparison of spatial interpolation methods for estimating snow distribution in the Colorado Rocky Mountains, *Hydrolog. Process.*, *16*, 3627-3649.

Evans, B. M., D. A. Walker, C. S. Benson, E. A. Nordstrand, and G. W. Petersen (1989), Spatial interrelationships between terrain, snow distribution and vegetation patterns at an arctic foothills site in Alaska, *Holarctic Ecol.*, *12*(3), 270-278.

Frezzotti, M., S. Gandolfi, F. La Marca, and S. Urbini (2002), Snow dunes and glazed surfaces in Antarctica: new field and remote-sensing data, *Ann. Glaciol.*, *34*(1), 81-88 (88), doi: 10.3189/172756402781817851.

Greene, E. M., G. E. Liston, and R. A. Pielke Sr. (1999), Relationships between landscape, snow cover depletion, and regional weather and climate, *Hydrolog. Process.*, *13*, 2453-2466.

Kuchment, L. S., and A. N. Gelfan (2001), Statistical self-similarity of spatial variations of snow cover: verification of the hypothesis and application in the snowmelt runoff generation models, *Hydrol. Processes*, *15*(18), 3343-3355.

Liston, G. E. (1999), Interrelationships among snow distribution, snowmelt, and snow cover depletion: Implications for atmospheric, hydrologic, and ecologic modeling, *J. Appl. Meteorol.*, *38*(10), 1474-1487.

Liston, G.E. (2004), Representing subgrid snow cover heterogeneities in regional and global Models, *J. Clim.*, *17*, 1381–1397.

Liston, G. E., and M. Sturm (1998), A snow-transport model for complex terrain. *J. Glaciol.*, *44*(148), 498-516.

Liston, G. E., R. A. Pielke, and E. M. Greene (1999), Improving first-order snow-related deficiencies in a regional climate model, *J. Geophys. Res. Atmos.*, *104*(D16), 19559-19567.

Liston, G. E., C. A. Hiemstra, K. Elder, and D. Cline (2008), Mesocell Study Area snow distributions for the Cold Land Processes Experiment (CLPX), *J. Hydrometeor.*, *9*(5), 957-976, doi: 10.1175/2008JHM869.1.

Luce, C. H., D. G. Tarboton, and K. R. Cooley (1998), The influence of the spatial distribution of snow on basin-averaged snowmelt, *Hydrolog. Process.*, *12*, 1671–1683.

Luce, C. H., D. G. Tarboton, and K. R. Cooley (1999), Sub-grid parameterization of snow distribution for an energy and mass balance snow cover model, *Hydrolog. Process.*, *13*, 1921-1933.

McGinnis, G. L., (2004), Estimating climate-change impacts on Colorado Plateau snowpack using downscaling methods. *Prof. Geogr.*, *45*(1), 117-125, doi: 10.1111/0033-0124.00062.

Shook, K, and D. M. Gray (1996), Small-scale spatial structure of shallow snowcovers, *Hydrolog. Process.*, *10*, 1283-1292.

Weitzenkamp, B., T. Sauter, A. Kraemer, R. Roth, and C. Schneider (2008), Spatial downscaling of snow cover as a tool for projections of snow availability for winter sports in 2030 in the Black Forest using Remote Sensing and GIS Methods, *Geophys. Res. Abstr.*, *10*, EGU2008-A-06206.

Xu, H., J. O. Bailey, E. C. Barrett, R. E. J. Kelly (1993), Monitoring snow area and depth with integration of remote sensing and GIS, *Int. J. Rem. Sens.*, *14*(17), 3259 – 3268.

2 Topographic, Meteorologic, and Canopy Controls on the Scaling Characteristics of the Spatial Distribution of Snow Depth Fields

2.1 Abstract

In this study, LIDAR snow depths, bare ground elevations (topography), and elevations filtered to the top of vegetation (topography + vegetation) in five 1-km^2 areas are used to determine whether the spatial distribution of snow depth exhibits scale invariance, and the control that vegetation, topography and winds exert on such behavior. The one-dimensional and mean two-dimensional power spectra of snow depth exhibit power law behavior in two frequency intervals separated by a scale break located between 7 m and 45 m. The spectral exponents for the low frequency range vary between 0.1 and 1.2 for the one-dimensional spectra, and between 1.3 and 2.2 for the mean two-dimensional power spectra. The spectral exponents for the high frequency range vary between 3.3 and 3.6 for the one-dimensional spectra, and between 4.0 and 4.5 for the mean two-dimensional spectra. Such spectral exponents indicate the existence of two distinct scaling regimes, with significantly larger variations occurring in the larger scales regime. Similar bilinear power law spectra were obtained for the fields of vegetation height, with crossover wavelengths between 7 m and 14 m. Further analysis of the snow depth and vegetation fields, together with wind data support the conclusion that the break in the scaling behavior of snow depth is controlled by the scaling characteristics of the spatial distribution of vegetation height when snow redistribution by wind is minimal and

7

canopy interception is dominant, and by the interaction of winds with features such as

surface concavities and vegetation when snow redistribution by wind is dominant.

2.2 Introduction

Spatial heterogeneity has been identified as one of the main features of snow covers in several environments [e.g., *Elder et al.*, 1991; *Blöschl and Kirnbauer*, 1992; *Luce et al.*, 1998]. The spatial distribution of snow is controlled by precipitation patterns and the interaction of the snow with factors such as topography, slope, aspect, vegetation, shortwave and longwave radiation, and wind. These interactions result in a highly heterogeneous snow cover in space and in time. Accounting for this heterogeneity is of paramount importance for hydrologic modeling and for appropriately describing land surface-atmosphere interactions [e.g., *Luce et al.*, 1997, 1998; *Liston and Sturm*, 1998; *Liston*, 1999; *Liston et al.*, 1999; *Greene et al.*, 1999].

Efforts to characterize this variability of snow properties have focused on exploring the statistical relationships between these properties and topographic variables that can be easily obtained by using digital elevation models (DEM's) and other computational tools. *Elder et al.* [1991] attempted to accurately determine the distribution of snow water equivalent (SWE) over a small alpine basin by identifying and mapping zones of similar snow properties on the basis of topographic and radiation parameters that account for variations in both accumulation and ablation. In their study, slope, elevation and radiation were used to obtain regressions of SWE as the dependent variable. Radiation consistently showed higher correlation with SWE, although weak correlations were obtained for all of the variables. *Blöschl and Kirnbauer* [1992] also studied the relationship between snow cover patterns and terrain characteristics, i.e., elevation and slope, in a mountainous area

9

in the Austrian Alps. They noted an increase in snow covered area with increasing elevation and decreasing slope, although no unique relationship to terrain parameters was apparent. Similar examples of this type of study include *Evans et al.* [1989] and *Hoasang and Dettwiler* [1991]. Although these approaches provide insight on how snow cover properties relate to each of these influencing variables, regression type relationships are only able to explain a small percentage of the variability, and no unique relationship can be defined for different environments due to differences in the dominant processes for different locations.

The applicability of such relationships has been explored in the development of methodologies to spatially extrapolate variables, such as snow depth and snow water equivalent, throughout an area based on information obtained from local and limited observations. Included in these efforts are the SWETREE model [*Elder et al.*, 1995; *Elder et al.*, 1998; *Winstral et al.*, 2002], which uses binary decision trees to estimate SWE and snow depth based on redistribution indices, terrain features and radiation. Other approaches involve the application of sub-grid parameterizations of snow distribution, using depletion curves to relate snow covered area with normalized snow water equivalence [*Luce at al.*, 1999, *Luce and Tarboton*, 2001, 2002], and the complex mean geostatistical methodology [*Erickson et al.*, 2005], which uses a kriging scheme with a nonlinear trend model to interpolate snow depth measurements. *Erxleben et al.* [2002] compared several of these spatial interpolation methods for estimating snow distribution in the Colorado Rocky Mountains. Snow depths measured on three 1-km^2 areas were interpolated by using inverse distance weighting, ordinary kriging, modified residual kriging and cokriging, and binary regression trees. Additionally, snow density samples

were interpolated by using linear regressions with elevation, slope, aspect, and net solar radiation, and SWE estimates were obtained by combining these two variables. They found binary regression trees to provide the most accurate estimates of snow depth; however, substantial portions of the variability were left unexplained by the models and none of them outperformed the others in all of the environments. These results illustrate the necessity for a better and more accurate characterization of the spatial and temporal organization of snowcover properties, focusing on the characteristics of the variability for different environments. *Blöschl* [1999] addresses several issues related to the accurate representation of snow cover properties, and the relationships between processes, measurement and model scales. Answers to questions about the nature of the spatial variability of snow properties across several scales, and about how this variability determines the scales at which snow measurements should be obtained still need to be addressed in order to improve our understanding of snow processes and to accurately represent snow cover properties in hydrologic applications.

In recent years, the concepts of fractals and scale invariance have been introduced to analyze the spatial and temporal structure of variables such as rainfall [e.g., *Lovejoy and Schertzer*, 1985; *Tessier et al.*, 1993; *Over*, 1995; *Over and Gupta*, 1996; *Marsan et al.*, 1996; *Kang and Ramírez*, 2001], soil moisture [e.g., *Rodríguez-Iturbe et al.*, 1995], topography [e.g., *Mandelbrot*, 1967, 1982; *Brown*, 1987; *Turcotte*, 1987, 1989; *Huang and Turcotte*, 1989], drainage network slopes [e.g., *Tarboton et al.*, 1988; *Rodríguez-Iturbe and Rinaldo*, 1996; *Molnár and Ramírez*, 1998], and steady-state and transient infiltration rates [e.g., *Meng et al.*, 1996]. In the case of snow properties, these concepts have been applied in the analysis of snow-covered area [e.g., *Shook et al.*, 1993; *Shook*

and Gray, 1997; *Blöschl*, 1999; *Granger et al.*, 2002], snow depth [e.g., *Shook and Gray*, 1994, 1996 and 1997; *Kuchment and Gelfan*, 2001; *Deems et al.*, 2006] and SWE [e.g., *Shook and Gray*, 1997], indicating that such variables exhibit fractal characteristics within a finite range of spatial scales.

Shook et al. [1993] analyzed the perimeter-area and area-frequency relationships of snow and soil patches of melting snowcovers in prairie and alpine environments for different stages during the melting season suggesting that snow and soil patches are fractals. They conclude that snow patches are not random and their size distribution is predictable and can be described by the use of simple power-law equations characterized by their fractal dimension. *Granger et al.* [2002] made use of these power-law relationships to describe snow and soil patches characteristics in the development of a methodology to determine the amount of energy removed by the snow patch surface as warmer air moves over it. *Shook and Gray* [1994, 1996] analyzed the fractal nature of snow depth in shallow snow covers by looking at the variation in the standard deviation of snow depth transects as a function of sample distance. Their results indicate a power-law type increase in the standard deviation up to sampling distances of the order of 20 m, after which the relationship curves towards a horizontal slope in the log-log plot. They conclude that this segmented power-law shape relationship indicates that the spatial distribution of snow depth is fractal at small scales (<30 m) and random at scales larger than this threshold, and that the cutoff length is related to the macroscopic (>100 m) variability of topography. Based on these findings, *Shook and Gray* [1997] implemented a methodology for generating a synthetic snowcover that forms snow patches having fractal properties, based on a fractal sum of pulses technique. In their methodology, the

12

synthetic data generated with the fractal technique are adjusted to resemble the characteristics of natural snowcovers by adjusting the generated frequency distribution to that estimated from field measurements. The statistical properties of the generated snow covers agree well with those of the measured fields, supporting the application of fractal techniques for synthetic generation of snow cover properties. *Kuchment and Gelfan* [2001] extended the analysis of snow depth to straight-line courses from 100 m to several kilometers in length to represent the micro- and meso- scale variability in several types of landscapes and relief, obtaining power law relationships in the variograms concluding that the snow depth fields could be considered statistically self-similar. Similar results were obtained by *Arnold and Rees* [2002] from the analysis of semivariograms of snow depth courses in glacier surfaces, concluding that snow depth distributions on glacier environments also exhibit fractal properties at short spatial separations and become random as separation increases.

In a recent publication, using data derived from LIght Detection And Ranging (LIDAR) observations, *Deems et al.* [2006] analyze the variograms of snow depth, topography and vegetation topography of three 1-km^2 study areas with a strong influence of snow redistribution by wind. From the observed log-log linearity of the variograms, they infer fractal behavior in the elevation, vegetation topography (elevation + vegetation height) and snow depth datasets. Their analyses seem to indicate the existence of two distinct scale regions with fractal distributions for the snow depth and vegetation topography datasets, separated by a scale break that varies between 15 m and 40 m for snow depth, and between 31 m and 56 m for vegetation topography, similar to the results obtained by *Shook and Gray* [1994, 1996], *Kuchment and Gelfan* [2001] and *Arnold and*

13

Rees [2002]. The fractal dimensions obtained for snow depth are of the order of 2.5 for the shorter scale range and 2.9 for the longer scale range. From these values, *Deems et al.* [2006] infer that for the short range there is a balance between high- and low-frequency variations, while at larger distances the distribution of snow depth approaches a spatially random distribution. Regarding the location of the breaks, *Deems et al.* [2006] speculate that the length of the scale break might be related to the overall terrain relief, and that the process change revealed by the breaks in the variograms of the vegetation topography (topography + vegetation height) data potentially influences the scaling behavior of snow depth. From relatively small variations of the fractal dimensions for different directions of the order of 0.1 in the snow depth, *Deems et al.* [2006] conclude that such variations show a strong qualitative relationship to prevailing winds and large-scale topographic orientation.

In this study, the spatial scaling characteristics of snow depth are explored based on the analysis of the power spectral densities of high-resolution LIDAR measurements ($\sim$ 1 m) distributed within five 1-km^2 areas (two of them used in *Deems et al.* [2006]) with significant differences in the characteristics of the spatial variability of the snow cover caused by differences in terrain, vegetation, and wind patterns. Spectral analyses are performed on the 1-km^2 raster fields of snow depth, topography, topography + vegetation height, and vegetation height. The dataset used in this study not only includes environments in which redistribution of snow by wind is dominant, but also includes environments in which snow redistribution is minimal and canopy interception of snowfall is dominant, allowing for the identification of differences in the spectral characteristics between these two types of environments. The results from the power

spectral analysis are complemented by an analysis of maximum wind speeds and directions, and of the separation distance between peaks in the snow depth and vegetation height profiles. Also, the spectral characteristics (e.g., spectral exponents) are compared to wind patterns in search for any relationship between the two. Throughout the discussion section, the results and conclusions obtained in this study are compared to those obtained in the previous point data studies, and in particular those presented in *Deems et al.* [2006], pointing out the new insights in the actual knowledge of the spatial variability of snow depth provided by the results presented here not pointed out in the published literature. A summary description of the scale invariance concepts applied in this study is included in the Appendix section.

2.3   Field Description and Dataset

The data used in this study were collected as part of the Cold Land Processes Experiment (CLPX) in 2003. The CLPX was a cooperative effort of NASA, NOAA and other government agencies and universities designed to advance the understanding of the terrestrial cryosphere, providing information to address questions on cold land processes, spatial and temporal variability of the snow cover, and uncertainty of remote sensing measurements and models [*Cline et al*, 2001]. The study area of the CLPX is conformed by a nested array of study areas at five different scale levels in the state of Colorado and a small portion of southern Wyoming (Figure 2.1). The two first levels correspond to one large and one small regional study areas of 3.5° x 4.5° and 1.5° x 2.5°, respectively. Three Meso-cell study areas (MSA) of 25-km x 25-km and nine 1 km x 1 km intensive study areas (ISA's) conform the third and fourth scale levels, respectively. The last scale level

corresponds to one local-scale observation site (LSOS) of 1 ha. This study focuses on five of the nine 1-km^2 ISA's. The ISA's located in the North Park MSA were not included in this study because their snow-covered area is less than 35% in all cases, while the Alpine ISA located in the Fraser MSA is analyzed in a separate study to illustrate differences between snowpack characteristics in alpine and sub-alpine environments. The areas included here correspond to the Fool Creek (FF) and Saint Louis Creek (FS) ISA's located in the Fraser MSA, and the Buffalo Pass (RB), Spring Creek (RS) and Walton Creek (RW) ISA's located in the Rabbit Ears MSA. A summary of the major characteristics of these areas is presented in Table 2.1.
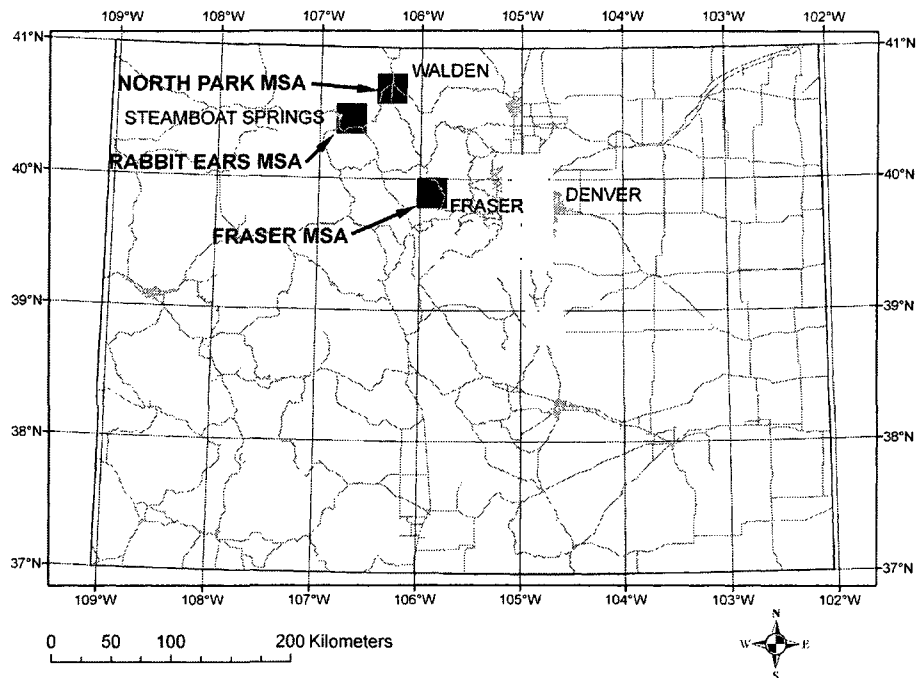
Figure 2.1. Location of the Meso-scale study areas of the CLPX within the state of

Colorado (USA).

Table 2.1. Major characteristics of the Intensive Study Areas (ISA's). Source: *Cline et al.*

[2001].

Name	Site	Characteristics
Fool Creek	FF	Moderately high-density coniferous (spruce-fir) forest, on wet north-facing slope.
St. Louis Creek	FS	Moderate-density coniferous (lodgepole pine) forest, on a flat aspect with low relief.
Buffalo Pass	RB	Dense coniferous forest interspersed with open meadows; low rolling topography with deep snow packs.
Spring Creek	RS	Moderate density deciduous forest (aspen); moderate topography on west-facing slope, with moderate snow packs.
Walton Creek	RW	Broad meadow interspersed with small, dense stands of coniferous forest; low rolling topography with deep snow packs.

The Fool Creek ISA is located in a forested area with a complex topography and variations in vegetation characteristics. Elevations range between 3014 m a.s.l. and 3284 m a.s.l. The ISA is part of the area of the Fraser Experimental Forest where extensive research has been performed on the effect of forest management practices on runoff. These forest management practices have led to a pattern of plots of cut and leave strips that produced differences in coniferous vegetation height. The Saint Louis Creek ISA is located at the lower part of the Fraser Experimental Forest. Elevations range between 2701 m a.s.l. and 2756 m a.s.l. The area presents mild slopes and a uniform coniferous forest cover, except for some small patches of open terrain. The Buffalo Pass ISA has an elevation range of 3053 m a.s.l. to 3233 m a.s.l. A stream that flows from east to west divides the area into a north-facing and a south-facing slopes. The Spring Creek ISA is an area with a more complex topography. The minimum and maximum elevations are 2668 m a.s.l. and 2903 m a.s.l. Aspect variations are a major feature in this ISA, with several south- and north- facing slopes spread over the area. Vegetation cover consists of dense patches of deciduous vegetation, and only a few clusters of coniferous trees. The rest of the area is covered by short vegetation and grass. Finally, the Walton Creek ISA is characterized by mild slopes and open areas. Elevation ranges between 2915 m a.s.l. and 2998 m a.s.l. A small percentage of the ISA is covered by coniferous vegetation, and the valleys are mostly covered by sage and willow shrubs.

This study makes use of LIDAR topographic maps collected for each of the ISA's for snow-covered and snow-free conditions. The data set consists of LIDAR elevation returns (filtered to bare ground/snow, and filtered to top of vegetation), elevation contours (0.5 m), and snow depth contours (0.1 m) [Miller, 2003]. These data were

processed from the LIDAR elevation returns with an average horizontal spacing of 1.5 m and vertical tolerance of 0.05 m. The snow depth contours were obtained by subtracting the two topographic surfaces corresponding to snow-covered conditions close to maximum accumulation (8-9 of April, 2003) and no-snow conditions (18-19 of September, 2003). The contour covers were used to generate Triangulated Irregular Network (TIN) surfaces of the fields in ArcGIS, which then were converted to rasters of 1024 by 1024 grid cells covering the entire 1-km^2 areas with a grid spacing of approximately 1 m for snow depth, bare ground elevations (topography), and elevation to the top of vegetation (topography + vegetation).

2.4   Methods of Analysis

2.4.1   One-Dimensional Power Spectra

One-dimensional power spectra were obtained separately for each of the west to east (x) rows and each of the north to south (y) columns of the fields on each of the ISA's by following the procedure described below. First, the complex coefficients of the discrete Fourier transform of the original series or signal were determined by using:

$$X(k) = \frac{1}{N} \sum_{n=0}^{N-1} x(n) exp[-j(2\pi/N)nk] \qquad (2.1)$$

where k is the wave number (from 0 to $N/2$), N is the total number of data points in the discrete signal $x(n)$, and j is the square root of -1. The power spectrum was then estimated by obtaining the square of the absolute value of the complex coefficients of the discrete Fourier transform as

19

$$\phi(k) = |X(k)|^2 \qquad (2.2)$$

where $\phi(k)$ is the power spectrum of the function $x(n)$. If the mean of the original signal is subtracted from the signal, the sum of the power spectrum over the entire range of frequencies equals the variance of the process. In this way, the power spectrum represents the absolute contribution of each frequency (or scale) to the total variance of the process. If the power spectrum is then divided by the variance, a power spectral density is obtained, where the value of the spectrum corresponds to the percentage of the total variance contributed by each frequency. The individual power spectral densities of the profiles in the x and y directions were then averaged over each direction, reducing the variability of the individual spectra and facilitating the fitting of power laws.

2.4.2 Directional One-Dimensional Power Spectra

In order to examine anisotropic behavior, that is, changes of the behavior of the power spectra of snow depth as a function of direction, this analysis makes use of the directional rasters for which the directions of the x and y coordinates of the lattice coincide with the directions for which the analysis is performed. For example, a rotation of the snow depth contours of 30° with respect to the west to east axis allows for the analysis of the power spectra for a 30°-210° (x-axis) direction, and for a 120°-300° (y-axis) direction. These lines correspond to two perpendicular directions, similar to rotating the east-west and north-south axes by an angle of 30°. These rasters were generated for even intervals of 10° (i.e., 0°-180°, 10°-190°, 20°-200°, ..., 170°-350° with respect to the east axis; equivalent to E - W, N 80° E - S 80° W, N 70° E - S 70° W, ..., N 80° W – S 80° E). Because the power spectral analysis must be performed on a square grid, the rotations of

the contour maps cause a reduction of the available information to a grid of 512 x 512 cells (next power down from 2^{10}) centered in the area. The one-dimensional power spectra for each direction were obtained by following the procedure described in Section 2.4.1.

2.4.3   Mean Two-Dimensional Power Spectra

A similar procedure is followed for the two-dimensional spectral analysis. First, the two-dimensional discrete Fourier Transform is estimated by using

$$X(k,l) = \frac{1}{N^2} \sum_{m=0}^{N-1} \sum_{n=0}^{N-1} x(m,n) exp\left[-j \frac{2\pi}{N} (km + ln) \right] \qquad (2.3)$$

where k and l are the wave numbers in the x and y directions (from 0 to $N/2$), N is the total number of data points in both, the x and y directions, and $x(m,n)$ is the original function. The two-dimensional power spectrum is then obtained by

$$\phi(k,l) = |X(k,l)|^2 \qquad (2.4)$$

The power spectral densities of the fields were obtained by dividing the power spectra by the variance. These two-dimensional power spectral densities were used to obtain mean two-dimensional power spectral densities. An equivalent wave number is assigned to each $\phi(k,l)$ following

$$r = \frac{1}{L} \left(k^2 + l^2 \right)^{1/2} \qquad (2.5)$$

where L is the dimension of the side of the square area for which the analysis is being performed (1000 m in this case). The mean spectral density ϕ_j for each equivalent wave number r is given by

21

$$\phi_j = \frac{1}{N_j} \sum_{i=1}^{N_j} |X_i(k,l)|^2 \qquad (2.6)$$

where N_j is the number of values that satisfy the condition $j/L < r < (j+1)/L$, and the summation is carried out over all the coefficients located in this frequency range.

2.5 Results

2.5.1 Snow Depth

2.5.1.1 One-Dimensional Power Spectra

The log-log plots of the one-dimensional power spectral densities of snow depth are presented in Figure 2.2. None of the one-dimensional power spectra present log-log linearity throughout the entire range of frequencies, although they can be subdivided into two frequency intervals within which the spectra is well represented by a power law. The scale break in each of the sites splits the power spectrum in a low-frequencies (larger scales) interval with a mild slope, and a high-frequencies (smaller scales) interval with a steeper slope. These power spectra with segmented power law indicate that the characteristics of the spatial variability of snow depth can be classified in different frequency regions or scale intervals within which the self-affinity condition (2.A3) (see Appendix) is met. A summary of the average spectral exponents and scale breaks is presented in Table 2.2. The wavelengths that separate these two intervals vary between 8 m and 35 m, with the smallest breaks at Fool Creek, Saint Louis Creek and Spring Creek. For these sites, little difference is observed in the crossover wavelengths in the x and y directions. On the contrary, the corresponding x and y crossover wavelengths for the

Buffalo Pass and Walton Creek fields differ 12 m and 13 m, respectively, indicating some degree of anisotropy on the variability of these snow depth fields. The spectral exponents obtained vary between 0.2 and 1.4 for the low-frequencies intervals, and between 3.1 and 3.6 for the high-frequencies intervals. These large differences between the spectral exponents of the larger and smaller scales intervals indicate marked differences in the nature of the variability of the snow depth cover above and below the scale break. Such differences are addressed in the discussion section.
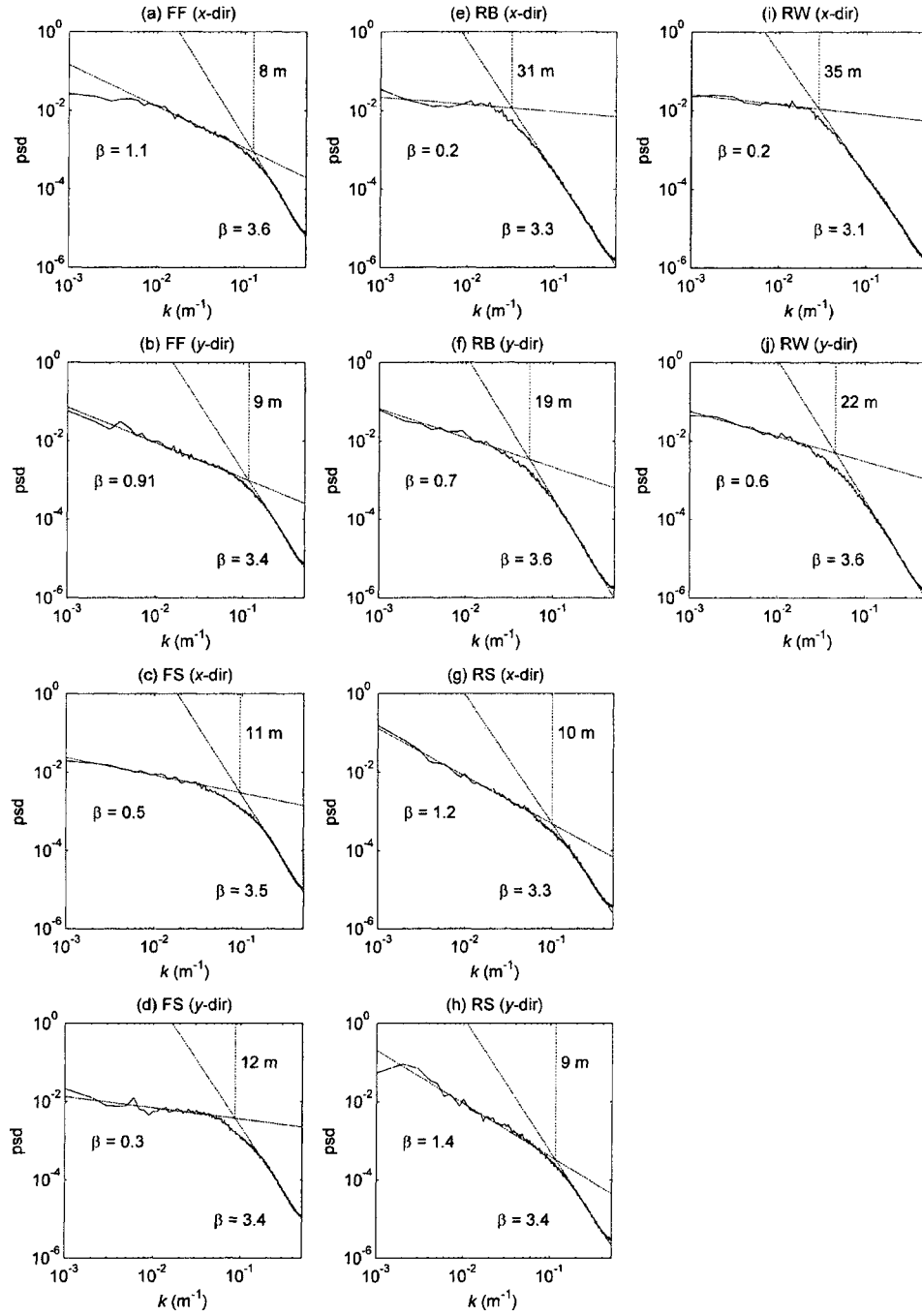
Figure 2.2. Average one-dimensional power spectral densities of snow depth in the east-west (x-dir) and north-south (y-dir) directions. k is the wave number divided by the length of the profiles (1000 m).

Table 2.2. Average spectral exponents and scale breaks of snow depth from the one-dimensional analysis of the non-rotated rasters (1024 x 1024).

	FF	FS	RB	RS	RW
Low-fequencies β	1.0	0.4	0.5	1.3	0.4
High-fequencies β	3.5	3.4	3.5	3.3	3.3
Scale break (m)	8	11	25	9	28

2.5.1.2 Directional One-Dimensional Power Spectra

The distributions of the spectral exponents and scale breaks of snow depth are summarized in Figure 2.3 and Table 2.3. The spectral exponents (Figure 2.3a) vary between 0.06 and 1.17 for the low-frequencies, and between 2.93 and 3.58 for the high-frequencies. Little variations are observed in the high-frequency values with respect to those observed in the corresponding low-frequency exponents. Average values range between 0.4 and 1.1 for the low-frequencies, and between 3.1 and 3.4 for the high-frequencies. The smallest and largest average exponents are found at Buffalo Pass and Spring Creek for the low-frequencies, and at Walton Creek and Saint Louis Creek for the high-frequencies, respectively. The crossover wavelengths (Figure 2.3b) are located at scales of the order of meters and tens of meters. The scale breaks at Fool Creek, Saint Louis Creek and Spring Creek present little variation around the mean, with average breaks between 9 m and 12 m. In contrast, the breaks at Buffalo Pass and Walton Creek exhibit larger variations and are located at larger scales that range between 19 m and 45 m, with average values of 21 m and 34 m, respectively. These variations indicate a more significant heterogeneity and directionality in the snow covers of these two areas.

25
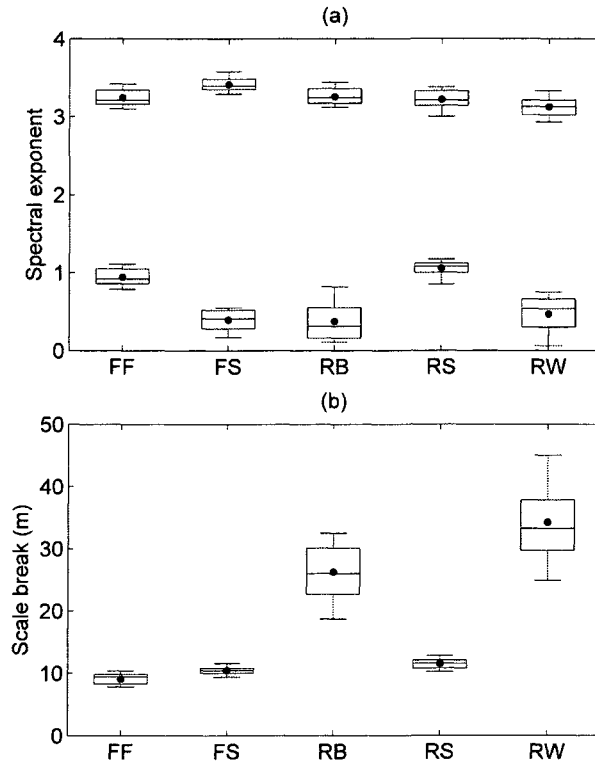
Figure 2.3. Distribution of the characteristics of the directional power spectral densities of snow depth in all possible directions. (a) Spectral exponents for the lower frequencies (smaller values) and higher frequencies (larger values) intervals, and (b) scale breaks. The external lines cover the entire range of the data, the lower and upper limits of the box mark the 0.25 and 0.75 percentiles, while the internal line marks the median. The dots correspond to the mean of the set.

Table 2.3. Average spectral exponents and scale breaks of snow depth from the directional one-dimensional analysis (512 x 512).

	FF	FS	RB	RS	RW
Low-fequencies β					
Mean	0.9	0.4	0.4	1.1	0.5
Standard deviation	0.11	0.12	0.23	0.09	0.23
High-fequencies β					
Mean	3.2	3.4	3.3	3.2	3.1
Standard deviation	0.10	0.09	0.11	0.12	0.11
Scale break (m)					
Mean	9	10	26	12	34
Standard deviation	0.9	0.6	4.1	0.8	6.2

2.5.1.3 Mean Two-Dimensional Power Spectra

The mean two-dimensional power spectral densities of snow depth are presented in Figure 2.4. Spectral exponents and scale breaks are summarized in Table 2.4. Consistent with the results of the one-dimensional spectra, the break in the scaling of snow depth is observed at wavelengths between 7 m and 22 m. At Fool Creek, Saint Louis Creek and Spring Creek, the breaks occur at wavelengths between 7 m and 9 m, while at Buffalo Pass and Walton Creek they occur at 18 m and 22 m, respectively. The spectral exponents vary between 1.3 and 2.2 for the low-frequencies, and between 4.0 and 4.5 for the high-frequencies. These spectral exponents for both intervals differ approximately by a unit with respect to the corresponding one-dimensional exponents.
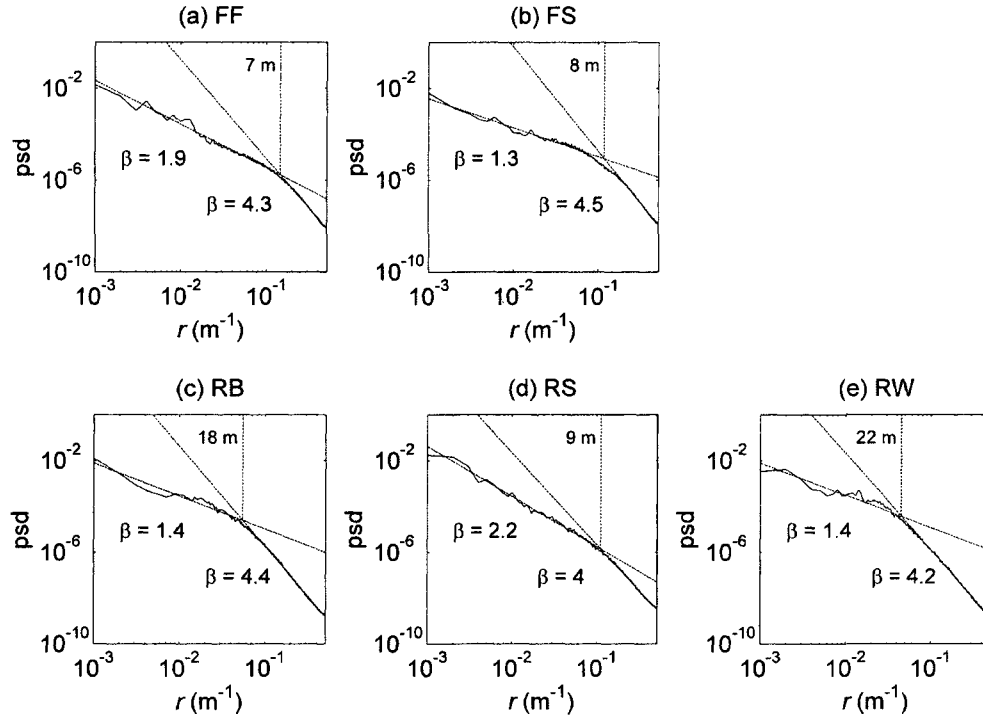
Figure 2.4. Mean two-dimensional power spectral densities of snow depth for all of the study areas. r is the equivalent wave number as in (2.5).

Table 2.4. Exponents and scale breaks for the mean two-dimensional power spectra of snow depth.

	FF	FS	RB	RS	RW
Low-fequencies β	1.9	1.3	1.4	2.2	1.4
High-fequencies β	4.3	4.5	4.4	4.0	4.2
Scale break (m)	7	8	18	9	22

2.5.2 Topography and Topography + Vegetation Height

2.5.2.1 One-Dimensional Power Spectra

The power spectra of topography in all of the study areas behave like $k^{-\beta}$ for the entire range of frequencies. The spectral exponents vary between 1.99 and 2.02, with almost no variations from site to site. Similar scaling behavior has been observed in previous studies of topographic profiles and contour lines, illustrating the vertical self-affinity and horizontal self-similarity of topography [e.g., *Mandelbrot*, 1967, 1982; *Brown*, 1987; *Turcotte*, 1987, 1989; *Huang and Turcotte*, 1989]. In these studies, spectral exponents around 2.0 were found for one-dimensional topographic profiles. Complementarily, the spectra of topography + vegetation height exhibit a distortion of the power law relationship with frequency observed in the spectra of topography. This distortion is more evident at Fool Creek and Saint Louis Creek, which are characterized by taller and denser vegetation. Also, the distortion is sometimes more evident in one of the two directions due to differences in the relative contribution of vegetation to the variability/roughness of the profiles along each direction. When vegetation height is of a similar order of magnitude as the elevation range, the contribution of vegetation to the total variance of the profile increases, leading to a more noticeable distortion in the power spectrum at the smaller scales. On the contrary, when the elevation range is greater than vegetation height, the contribution of vegetation to the variability of the profile is reduced, and little distortion in the power spectrum is perceived. These differences are more evident at Fool Creek, Saint Louis Creek, and Walton Creek, where the elevation range is greater in one direction than in the other. None of the scale breaks in the power spectra of snow depth

can be observed in the power spectra of bare ground elevations, or in the spectra of topography + vegetation. Neither the power spectrum exponents nor the scale breaks of the snow depth fields can be explained based on the power spectrum of the underlying topography and topography + vegetation. If the scale break in the scaling characteristics of snow depth observed at the smaller scales is the product of a switch in the dominant process(es) driving the variability of the snow cover properties, this change is not, at least evidently, explained by the spectral characteristics of either the underlying topography or topography + vegetation.

2.5.2.2 Directional One-Dimensional Power Spectra

The power law exponents of the directional spectra of topography vary between 1.94 and 2.1, with an average of 2.0. Little anisotropy is perceived in the characteristics of the directional spectra. The inclusion of vegetation height in the topographic profiles induces a distortion of the power law relationship in all directions. No scale breaks are observed in the directional spectra of topography or topography + vegetation.

2.5.2.3 Mean Two-Dimensional Power Spectra

Spectral exponents between 2.92 and 2.94 were obtained for the mean two-dimensional power spectra of topography, which differ approximately by a unit with respect to the one-dimensional values. Such spectral exponents are consistent with similar analyses of the mean two-dimensional power spectra of topography [e.g., *Huang and Turcotte*, 1989], in which an average exponent of 2.82 was found for different types of topography.

2.5.3 Vegetation

2.5.3.1 One-Dimensional Power Spectra

The average one-dimensional power spectra of vegetation height are presented in Figure 2.5 and the spectral exponents and scale breaks are summarized in Table 2.5. Vegetation exhibits similar scaling characteristics as the corresponding snow depth covers. A low-frequencies interval with mild slopes and a high-frequencies interval with steeper slopes are separated by a scale break located at wavelengths between 7 m and 16 m. The spectral exponents vary between 0.3 and 1.2 for the low-frequencies, and between 1.9 and 3.4 for the high-frequencies. The breaks at the Fool Creek, Saint Louis Creek and Spring Creek differ from those in the snow depth scaling between 0 m and 3 m, while at Buffalo Pass and Walton Creek the differences vary between 9 m and 15 m, with breaks at larger scales for snow depth. There is a difference in the scaling behavior of the snow covers of these last two areas with respect to that of the corresponding vegetation covers.
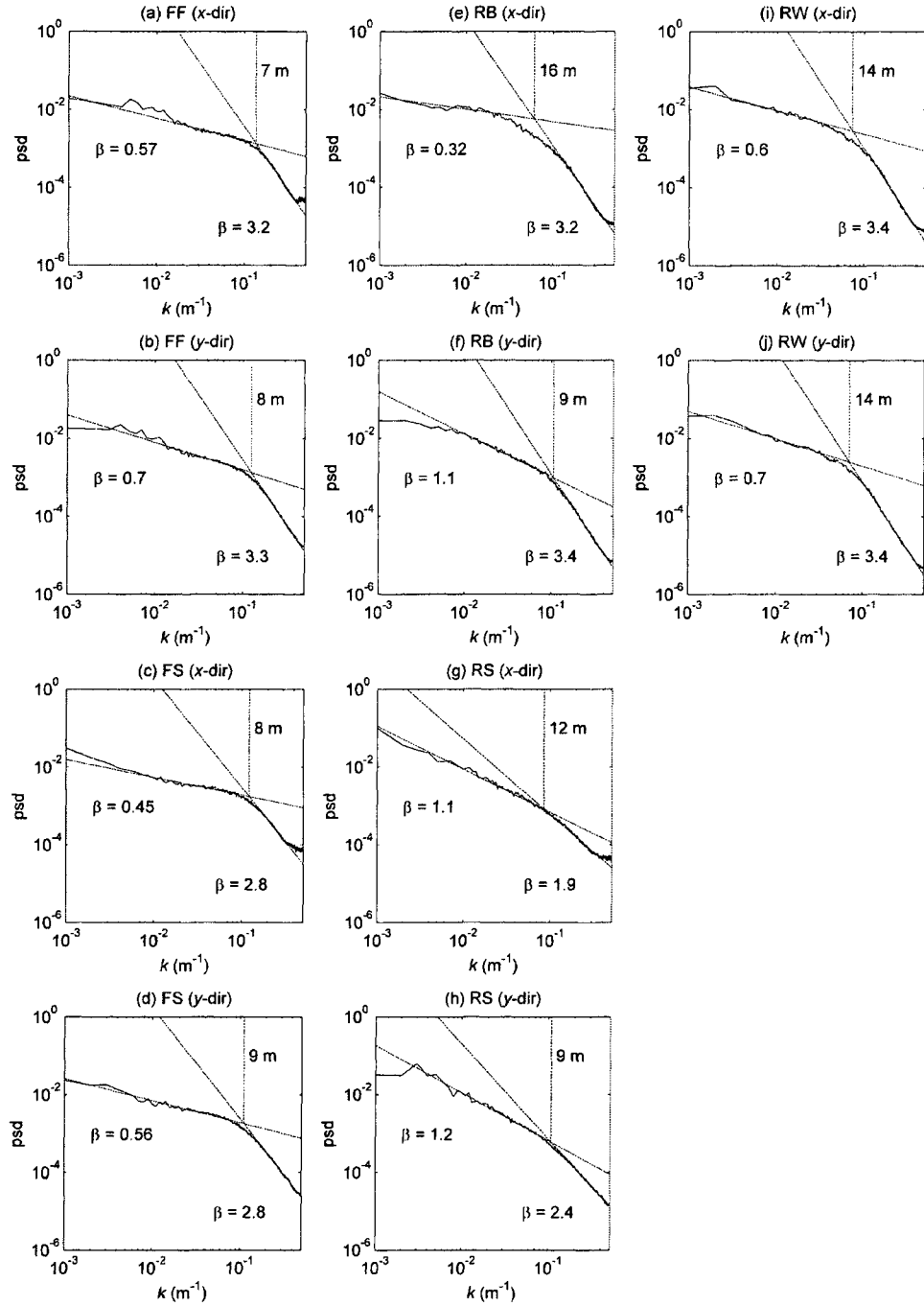
Figure 2.5. Average one-dimensional power spectral densities of vegetation in the east-west (*x*-dir) and north-south (*y*-dir) directions. *k* is the wave number divided by the length of the profiles (1000 m).

Table 2.5. Spectral exponents and scale breaks of vegetation from the one-dimensional spectral analysis.

	FF	FS	RB	RS	RW
Low-fequencies β	0.6	0.5	0.7	1.2	0.7
High-fequencies β	3.2	2.8	3.3	2.2	3.4
Scale break (m)	8	9	13	11	14

2.5.3.2 Mean Two-Dimensional Power Spectra

The spectral exponents and scale breaks in the mean two-dimensional spectra of vegetation height are summarized in Table 2.6. The scale breaks are located between 7 m and 11 m, and the slopes vary between 1.1 and 2.0 for the low-frequencies and between 2.9 and 4.3 for the high-frequencies. The breaks at Buffalo Pass and Walton Creek differ from those in the mean two-dimensional spectra of snow depth by 7 m and 13 m, respectively. The spectral exponents of snow depths for each of the intervals do not correspond exactly to the exponents of vegetation heights due to the differences between the magnitudes of the variations of the snow depth cover and those of the corresponding vegetation cover at each scale.

Table 2.6. Exponents and scale breaks for the mean two-dimensional power spectra of vegetation height.

	FF	FS	RB	RS	RW
Low-fequencies β	1.1	1.4	1.3	2.0	1.7
High-fequencies β	3.8	3.3	4.2	2.9	4.3
Scale break (m)	7	7	11	9	9

2.6 Discussion

Overall, the results from the spectral analyses of snow depth indicate the existence of two distinct scaling regimes within the interval between 1 m and 1 km, each characterized by a distinct spectral exponent. These two regimes are separated by a scale break located at scales of the order of meters to tens of meters. The existence of these scaling regimes is caused by differences in the characteristics of the variability above and below the break. Within each interval, the power spectrum follows a power law dependence on frequency indicating self-affinity in the snow depth covers within finite frequency/scale intervals. This type of scaling behavior with segmented power law spectrum, referred to as bilinear (two intervals) or multilinear (multiple intervals) [*Veneziano and Iacobellis*, 1999], has been observed in several other processes such as rain rate [*Crane*, 1990] and groundwater base flow [*Zhang and Schilling*, 2004; *Zhang and Li*, 2005]. For the case of rain rate, *Crane* [1990] associates the changes in the spectral exponents and the wave numbers at which these breaks occur with the characteristics of the two-dimensional turbulent processes that determine the spatial distribution of rainfall. *Zhang and Schilling*, [2004] and *Zhang and Li* [2005] obtained similar bilinear power spectra for estimated time series of base flow on five different rivers in the state of Iowa (USA). They conclude that the high-frequency variations of the base flow are related to individual rainfall events ranging from a few hours to a few days, while the low-frequency variations are the result of seasonal changes.

For the case of snow depth, similar scale breaks have been observed in previous studies of point data. *Shook and Gray* [1994, 1996] analyzed the standard deviation of snow depth transects in prairie and artic environments as a function of sample size (~

34

sample distance), covering distances up to 1200 m. Their results indicate a power-law type increase in the standard deviation up to sampling distances of the order of 20 m, after which the relationship curves towards a slope of 0.06 in the log-log plot. *Shook and Gray* [1996] defined a 'cut-off' length as the point of intersection between the initial slope and a horizontal tangent to the end of the curve in the log-log plot of standard deviation versus sample distance. This definition is used to compare the scale at which the break occurs in different environments, extending the analysis to transects in two other areas with variations in elevation range. Cut-off lengths between 30 m and 500 m were obtained for the three environments. *Arnold and Rees* [2003] obtained similar results from the analysis of semivariograms of snow depth courses in glacier surfaces. Their results indicate an increase in the variance with separation under scales between 20 m and 30 m in the summer, and between 35 m and 45 m in the spring, after which the semivariograms reach a reasonably flat sill. In a more recent study, *Deems et al.* [2006] analyzed the variograms of the LIDAR snow depths of the Buffalo Pass, Walton Creek and Alpine ISA's. Their results indicate a similar bilinear behavior with a break at scales between 15 m and 40 m. However, *Deems et al.* do not present any conclusive evidence of the link between such bilinear behavior and the physical processes driving the variability of snow depth. Later in this discussion, the relationship between the observed bilinear behavior of the power spectrum of snow depth and controlling variables such as vegetation and wind patterns is determined based on additional analysis of the vegetation height fields and wind data in each of the study areas.

The one-dimensional spectral exponents obtained for snow depth vary between 0.1 and 1.4 for the low-frequencies intervals, and between 2.9 and 3.6 for the high-

frequencies intervals. Such low-frequency exponents indicate that for points separated by distances larger than the corresponding scale break, the snow depth values are weakly correlated, although the correlation is not necessarily zero, and there is some weak long-range persistence. In contrast, the high-frequencies exponents indicate that snow depth values for points separated by distances smaller than the corresponding scale break are highly correlated, and that the snow depth surface becomes smoother below the scale break. The variability is significantly different above and below the break. This spatial organization of snow depth within these two scale intervals is described differently in previous studies. *Shook and Gray* [1994, 1996] describe the distribution of snow depth as fractal below scales between 20 m and 100 m, and random above such scales, based on slope values in the log-log plots of snow depth versus sampling distance of 0.47 for the short range interval, and 0.06 for the long range interval. Similarly, *Arnold and Rees* [2002] conclude from the flattening of the log-log semivariograms of snow depth above separation distances between 10 m and 45 m that snow depth distributions show fractal properties at short separations, and become random as separation increases. *Deems et al.* [2006] also suggest, from fractal dimensions of around 2.5 for the short range and 2.95 for the long range, that the snow depth distributions exhibit fractal properties at short spatial separations and become almost random above the corresponding scale breaks. The scale breaks found in this study are located within the same orders of magnitude as those found in the quoted studies, although the spectral exponents for the low-frequencies indicate that the distribution of snow depth at scales larger than the corresponding break is not completely random, if the term 'random' is used to refer to processes of the white noise type which exhibit horizontal power spectra ($\beta = 0$), indicating equal contributions

from all frequencies to the total variance. The results obtained in this study indicate the existence of some organization at scales larger than the scale break such that the contribution of each frequency to the total variance can be described by a power-law, with an average spectral exponent (including all sites) of 0.65 for the one-dimensional case, and 1.64 for the two-dimensional case. Such exponents indicate a decaying contribution of each frequency to the total variance. This organization is site dependent, and although some of the sites present spectral exponents that are closer to zero, the range of exponents found indicates that the distribution of snow depths above a characteristic scale of the order of meters to tens of meters cannot be generalized as random or uncorrelated.

As expected (see Appendix), the exponents of the mean two-dimensional spectra for the two frequency regions (i.e., the low- and high-frequencies) differ approximately by one with respect to the one-dimensional exponents. Such difference is consistent with the theoretical difference between the exponents of the one-dimensional and two-dimensional power spectra for self-affine fields where all directions in the x-y plane are equivalent, i.e., no scaling anisotropy in the x-y plane [e.g., Appendix; *Voss*, 1985b]. When compared to the directional one-dimensional exponents, the exponents of the mean two-dimensional spectra for the low-frequencies differ between 0.6 and 1.3 for Buffalo Pass, and between 0.7 and 1.4 for Walton Creek. On the other hand, such differences vary between 0.8 and 1.1 at Fool Creek, between 0.7 and 1.1 for Saint Louis Creek, and between 1.0 and 1.3 for Spring Creek. The range of variation of the difference between the exponents of the mean two-dimensional spectra and one-dimensional spectra for the low frequencies is larger for the Buffalo Pass and Walton Creek areas, indicating a more

significant scaling anisotropy in such fields for the larger scales. On the contrary, no significant scaling anisotropy is observed in the high-frequencies exponents for all of the areas, with ranges of variation of the order of 0.3 in all of the five ISA's.

In search for explanations for the observed segmented power law spectrum of snow depth, a similar scaling analysis was performed on the fields of topography, topography + vegetation and vegetation height. The topographic fields contain information about the variations in elevation, slope and surface roughness which affect precipitation patterns, wind dynamics, redistribution of snow by avalanches, and energy fluxes due to variations in slope and aspect, among others. The fields of vegetation height contain information about the small-scale characteristics of the vegetation cover such as the separation between individual trees, height and area covered by the foliage, as well as larger scale characteristics such as the location of tree clusters and their average characteristics. Such properties have a strong influence in the distribution of snow through processes such as canopy interception of snowfall and the interaction with wind. The topography + vegetation fields provide information about the combination of such controls. None of the breaks in the slope of the log-log spectra of snow depth are present in the power spectra of the corresponding fields of topography and topography + vegetation. Neither the power spectrum exponents nor the scale breaks can be explained based on the power spectrum of the underlying topography and topography + vegetation. On the other hand, vegetation height exhibits very similar scaling behavior as the snow depth fields with bilinear power spectrum and scale breaks at wavelengths between 7 m and 14 m, with mild slopes for the low-frequencies, and steeper slopes for the high-frequencies (Figure 2.5).

38

The study areas can be separated into two groups according to the similarities or differences between the locations of the scale breaks in snow depth and the corresponding vegetation height. The snow covers of Fool Creek, Saint Louis Creek and Spring Creek exhibit scale breaks at similar scales as the corresponding vegetation fields, while at Buffalo Pass and Walton Creek the scale breaks of the snow depth occur at larger scales with respect to those of the corresponding vegetation height (see Tables 2-4 for snow depth and 5-6 for vegetation height). However, there are also important differences in the nature of the variability of snow depth between these two groups. Examination of the snow depth rasters of the study areas (not shown) indicates that the snow covers of Fool Creek, Saint Louis Creek and Spring Creek are exposed to little or no wind redistribution, and small-scale variability consistent with the vegetation patterns is dominant. On the other hand, the snow covers of the Buffalo Pass and Walton Creek exhibit patterns of drifts and scour areas consistent with the location of obstacles such as vegetation and ridges with respect to the predominant wind directions. To illustrate the importance of wind-driven snow redistribution in the study areas, wind data at 1 m above maximum expected snow depth (lower sensor) and 10 m above the ground (upper sensor) for the period October/2002 – April/2003 were analyzed. This period is chosen to represent the meteorological characteristics between the first snowfalls and the time at which the LIDAR snow depths were obtained. These meteorological data were collected as part of the CLPX within each of the ISA's at towers located approximately in the center of each area. Given that snow redistribution due to wind is only likely to occur when the air temperature is below freezing, only maximum wind speeds for 10-minutes intervals with air temperature less than $0°$ C are analyzed. The empirical distribution

functions of the maximum wind speeds at the lower and upper sensors are shown in Figure 2.6. The average maximum wind speeds at the lower and upper sensors are 0.8 m/s and 1.8 m/s at Fool Creek, 0.4 m/s (both levels) at Saint Louis Creek, 2.3 m/s and 2.6 m/s at Spring Creek, while they are 3.5 m/s and 4.4 m/s at Buffalo Pass, and 3.8 m/s and 4.4 m/s at Walton Creek, respectively. The empirical distributions indicate higher wind speed regimes at the last two areas, consistent with the observed patterns of snowdrifts and scour areas in the snow depth rasters.
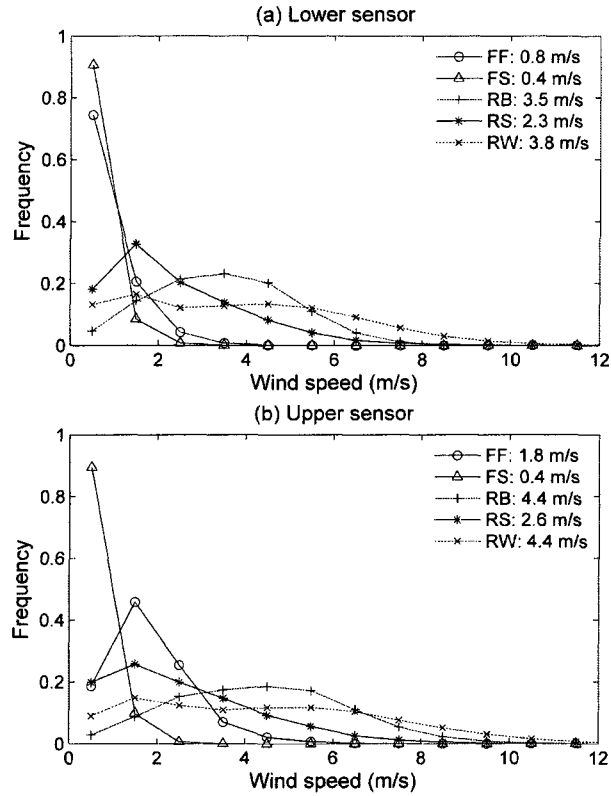
Figure 2.6. Empirical distribution functions of maximum wind speed every 10-minute intervals for the period October/2002 – April/2003 measured within each ISA at (a) 1 m above the maximum expected snow depth (lower sensor) and (b) 10 m above the ground (upper sensor). Only data for intervals with air temperature lower than $0°$ C are included. Average values are included in the legends.

With respect to the vegetation topography (topography + vegetation height) data, the variogram analysis of *Deems et al.* indicates the existence of a scale break at distances of the same order of magnitude as those observed in the snow depth variograms, though at a slightly longer absolute range. On the other hand, their variograms of vegetation height data (vegetation topography with bare earth terrain subtracted) do not display a scale

break. *Deems et al.* conclude that the similarity between the scale break separating the two regions in the terrain–vegetation distributions and that observed in the snow depth data indicates that the process change revealed in the vegetation–terrain data potentially influences the scaling behavior of snow depth patterns. These observations are contrary to what is observed in the power spectral analysis presented in this study. As mentioned above, no scale breaks are observed in the spectra of topography + vegetation. On the other hand, the spectral densities of vegetation height for all of the study sites exhibit a break at wavelengths between 7 m and 16 m. The locations of the scale breaks in the power spectra of vegetation height coincide with the breaks in the spectra of snow depth only in the areas in which little redistribution of snow by wind exists, and small-scale variability consistent with the vegetation patterns is dominant. On the other hand, the scale breaks in the snow depth spectra in the areas where snow redistribution by wind is dominant are located at larger spatial scales than those of the corresponding vegetation.

In order to compare the characteristics of the variability of the snow depth cover between these two environments, two sample profiles of snow depth of the Saint Louis Creek and Walton Creek snow covers are presented in Figure 2.7. The differences in the variability of the profiles are evident. The Saint Louis Creek snow cover is characterized by small-scale variations and lower variance (compare the vertical scales), while the snow cover at Walton Creek exhibits larger scale variations and higher variance. In Figure 2.7, 'd' is defined as the separation distance between peaks (or local maxima) above a threshold equal to the mean snow depth of the profile. The Walton Creek profile exhibits larger separations as a sign of larger characteristic scales. Based on this definition, the empirical distribution functions of the separation distance 'd' were

obtained using all of the profiles in each of the snow depth fields in the x and y directions (Figure 2.8). The distributions for the first group have very similar shapes with a marked mode located between 7 m and 10 m, while for the second group they are more uniform, with flatter peaks, and with modes located between 11 m and 16 m. The snow depth surfaces of Buffalo Pass and Walton Creek exhibit larger separations between peaks. These results are consistent with the spectral characteristics of the snow depth fields, for which the breaks in the slope of the log-log spectra occur at larger spatial scales at Buffalo Pass and Walton Creek.
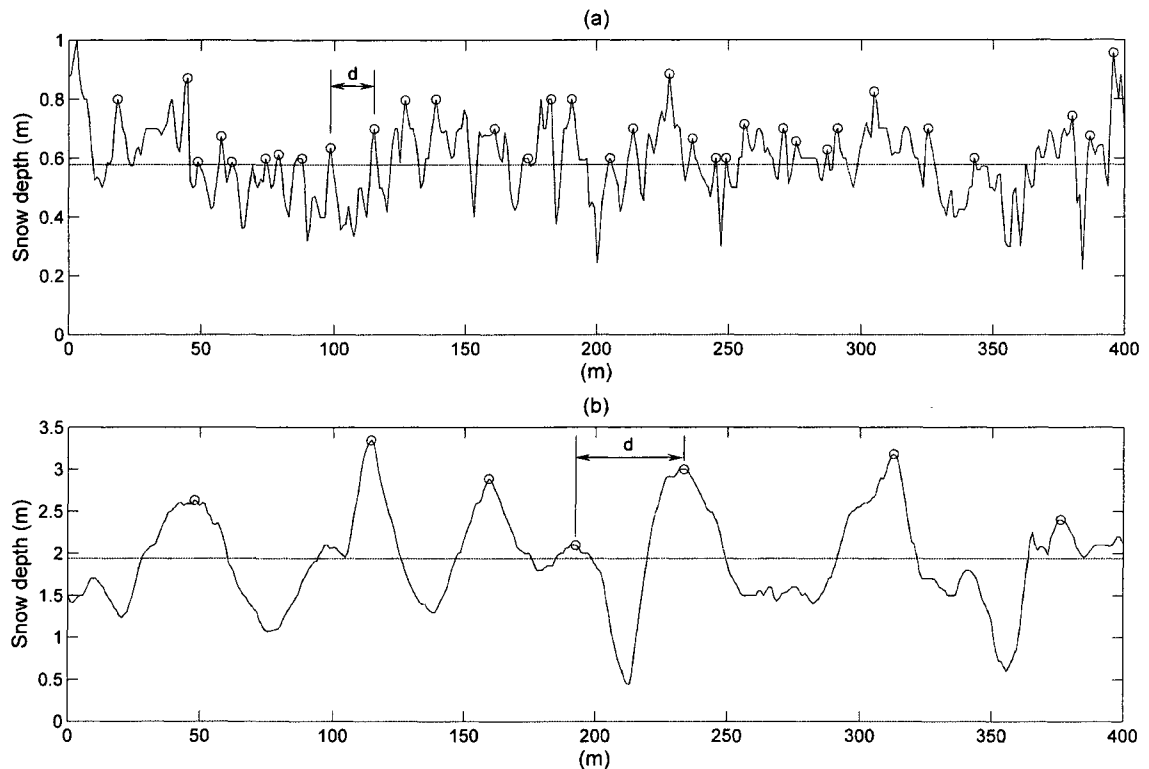
Figure 2.7. Sample profiles of snow depth at (a) St. Louis Creek and (b) Walton Creek. The circled points mark the location of the local maxima using a threshold equal to the average of the profile. The separation 'd' marks the distance between these peaks.
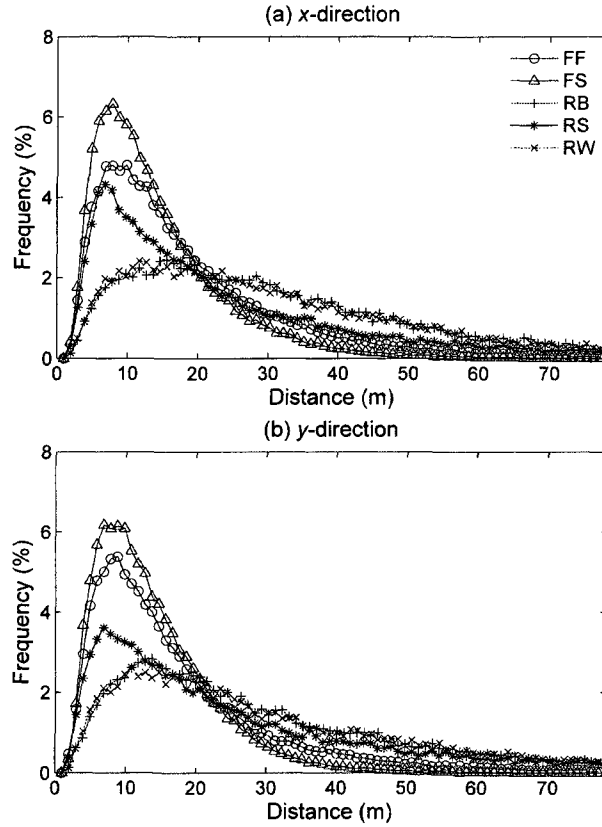
Figure 2.8. Empirical distribution functions of the separation distance between peaks in the snow depth profiles.

The similarities between the power spectrum of snow depths and vegetation heights at Fool Creek, Saint Louis Creek and Spring Creek indicate similarities in the variability of the two corresponding fields. The empirical distribution functions of the separation distance in the vegetation height and snow depth fields of these study areas (Figure 2.9) have very similar characteristics, with gamma-type distributions and modes located within similar separation ranges (from 5 m to 8 m for vegetation height and from 7 m to 10 m for snow depth). The separations between peaks in both of the fields exhibit similar

44

statistical characteristics, indicating similar characteristic scales. These similarities are a consequence of the effect of vegetation in the distribution of snow depth. Because of interception, the peaks (maxima) in vegetation height coincide with valleys (minima) in the snow depth surface, and the information that their corresponding separation distances provide about the scales of the variations is statistically equivalent in both fields. As wind redistribution is minimal in these areas, the characteristic scales of snow depths remain similar to those of the vegetation heights.
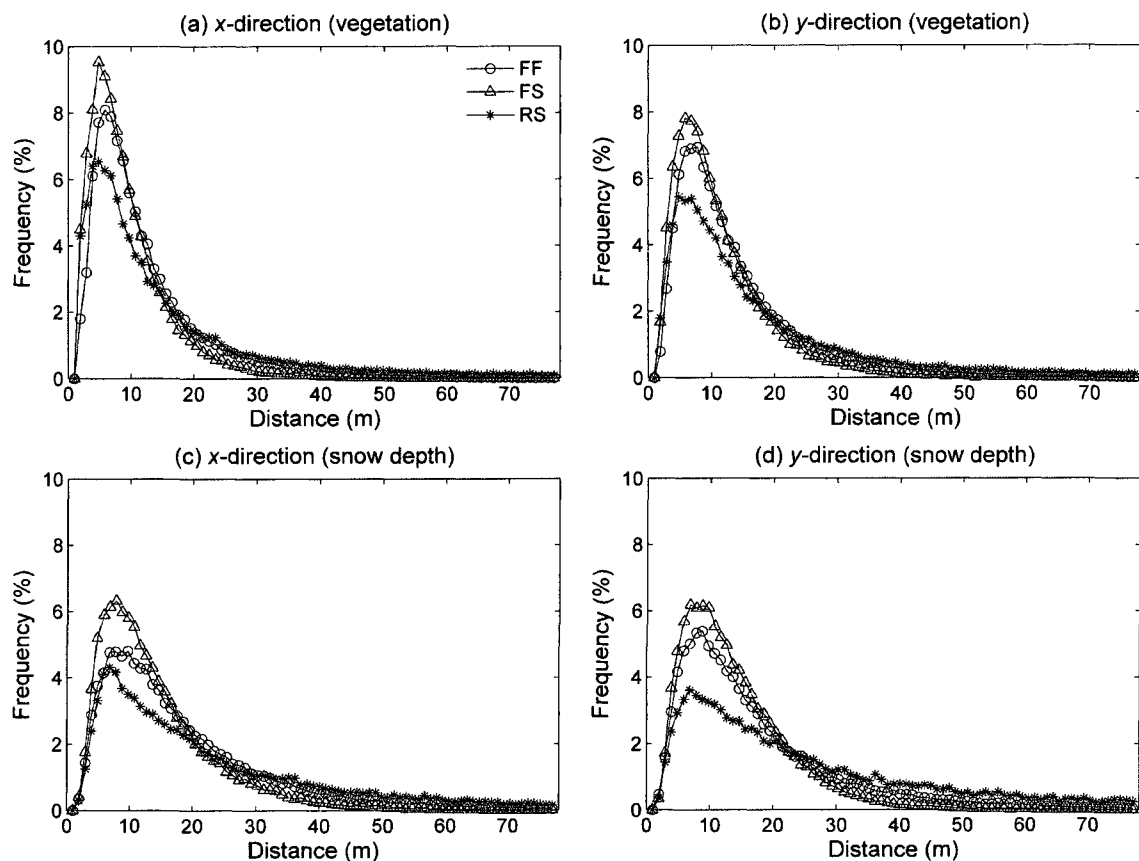
Figure 2.9. Empirical distribution functions of the separation distance between peaks in the vegetation height and snow depth profiles of the Fool Creek, St. Louis Creek and Spring Creek ISA's.

The directional analysis of the snow depth spectra (Figure 2.3) indicates higher directionality in the Buffalo Pass and Walton Creek snow depths, with the largest variations in the low-frequencies exponents and scale breaks with direction. These variables are compared to the distributions of wind direction for the period October/2002 – April/2003 in Figure 2.10. The distributions represent the percentage of time that wind blows along a specific line (either direction). Both, the low-frequencies exponent and scale break, exhibit a strong relationship with the predominant wind directions. The lowest low-frequencies exponents occur along the predominant wind directions while the highest occur along the perpendicular to the predominant direction. This relationship implies that the snow depth profiles are more variable (rougher) along the predominant wind directions when looked at scales larger than the corresponding scale break. Lower spectral exponents imply a more horizontal slope in the log-log spectrum and higher contributions of the low-frequencies to the variance of the profiles. Along the predominant wind direction, most of the variations in snow depth caused by redistribution are a consequence of the vertical interaction of wind patterns with obstacles such as ridges, depressions, and clusters of vegetation. Along the perpendicular direction, a switch in the processes occurs and most of the variations in snow depth caused by redistribution are a consequence of horizontal interactions of wind patterns with obstacles such as trees and rocks. The characteristic scales of such processes depend mainly on the separation distance between obstacles, wind velocities (speed and direction) and surface conditions (e.g., cohesion and roughness). The differences between these processes translate in anisotropy and directionality of the snow depth surface. The results obtained

46

in this study are a consequence and evidence of such directional effect, and the gradual variation of the scaling properties of snow depth in wind-dominated environments (Figure 2.10) is a consequence of the combination of the vertical and horizontal interaction of wind patterns with obstacles along directions between the predominant and perpendicular directions. The results presented in Figure 2.3 also indicate little or no directionality in the spectral properties of snow covers with little or no redistribution. The spectral exponents and scale breaks for the snow covers of Fool Creek, Saint Louis Creek and Spring Creek exhibit little variations with direction. The characteristics of the variability of snow depth are relatively similar along any direction, as snow redistribution by wind does not cause extended patterns of snowdrifts and scour areas along any particular direction.
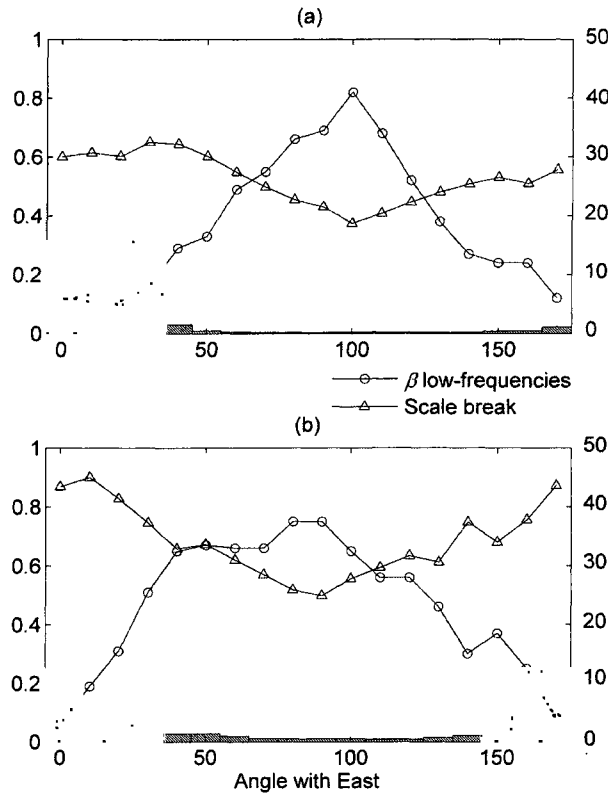
Figure 2.10. Spectral exponents for the low-frequencies intervals (left axis) and scale breaks (right axis (m)) as a function of direction for the (a) Buffalo Pass and (b) Walton Creek ISA's. The histograms correspond to wind directions during intervals with air temperatures below freezing. Similar histograms of wind direction are obtained for wind speeds above thresholds of 4 m/s and 5 m/s.

For Buffalo Pass and Walton Creek, *Deems et al.* report that for distances shorter than the scale break, the snow depth fractal dimensions are larger in directions normal to the prevailing winds, while for longer scales, the largest dimensions occur parallel to the dominant wind direction. However, the variations in the fractal dimensions reported by *Deems et al.* without indicating their significance level are of the order of 0.1 or less for

48

the two scale regions, variations that might be easily induced by small changes in the number of data used for the regressions. In this study, consistent variations with direction at the Buffalo Pass and Walton Creek ISA's were only observed in the spectral exponents of larger-scales intervals and the locations of the scale breaks. Little variations were observed in the spectral exponent of the smaller-scales intervals (Figures 2.3 and 2.10).

A hypothesis proposed first by *Shook and Gray* [1996], and adopted later by *Deems et al.* [2006], to explain the bilinear behavior of the spatial scaling of the distribution of snow depth relates the scale break distance to topographic relief. The results presented in this study reveal that relief does not play a significant role in the observed scaling behavior of the spatial distribution of snow depth, and instead, variables such as vegetation and winds are far more relevant when explaining such behavior within the range of scales analyzed.

The differences between the two scaling regimes (i.e., low- and high- frequencies) in the snow depth fields have important consequences for the characterization of the snow cover. As discussed earlier, the scale break is a measure of the separation between peaks in the snow depth surface. When the snow depth surface is analyzed above such scales, the average effects of the controlling variables need to be accounted for. Such effects correspond to the average snowfall interception by vegetation in environments dominated by canopy interception of snowfall, and the average accumulation or scour induced by redistribution of snow in wind-dominated environments. When the snow cover is looked at scales smaller than the corresponding break, the detailed characteristics (variability between peaks) become evident, and the small-scale interactions become dominant (e.g., vegetation interception by individual trees and wind interaction with surface concavities,

trees and rocks). The scales at which snow models work should be selected according to such characteristic scales. Unless the available input data allows for an accurate representation of the small-scale interactions, model scales should be selected within the low-frequency (larger scales) range. The results presented here indicate that such scales should exceed 10 m in environments where snow redistribution is minimal, and between 20 m and 40 m in environments where wind redistribution is dominant. These scales are expected to change according to the particular characteristics of each environment, so the values presented in this paper should be used only as reference scales.

2.7 Conclusions

LIDAR snow depths, bare ground elevations and elevations filtered to the top of vegetation obtained in April and September of 2003 were analyzed to characterize the spatial variability of snow depth. Based on the characteristics of the power spectral densities of these fields, the relationship of such variability to influencing factors such as topography and vegetation was defined. The power spectra of snow depth behave as $k^{-\beta}$ within two distinct frequency intervals, each with different spectral exponent. The one-dimensional spectral exponents obtained for snow depth vary between 0.1 and 1.4 for the low-frequencies intervals, and between 2.9 and 3.6 for the high-frequencies intervals, while the exponents of the mean two-dimensional power spectra vary between 1.3 and 2.2 for the low-frequencies, and between 4.0 and 4.5 for the high-frequencies. Such values indicate that the snow depth surface is more variable (or rougher) when observed at scales larger than the corresponding scale break, while much smaller variations appear when looked at scales smaller than such break. The larger scales explain the majority of

the variability. The scales that separate these two intervals are located at wavelengths between 8 m and 45 m. None of the scale breaks in the snow depth power spectra were observed in the power spectra of bare ground elevation, or in the spectra of topography + vegetation. Neither the power spectrum exponents nor the scale breaks can be explained based on the power spectrum of the underlying topography and topography + vegetation. On the other hand, the spectrum of vegetation height exhibits very similar behavior as the snow depth spectrum, with a low-frequencies interval with mild slopes between 0.3 and 1.2 for the one-dimensional spectra, and between 1.1 and 2.0 for the mean two-dimensional spectra, and a high-frequencies interval with steeper slopes between 1.9 and 3.4 for the one-dimensional spectra, and between 2.9 and 4.3 for the mean two-dimensional spectra. These two intervals are separated by a scale break located between 7 m and 16 m for the one-dimensional spectra, and between 7 m and 11 m for the mean two-dimensional spectra.

When the spectra of snow depth are compared to the spectra of the corresponding vegetation height, two distinct scaling behaviors can be identified. In the areas in which snowfall interception is dominant and snow redistribution by wind is minimal, the scale breaks in the snow depth spectra occur at similar scales as those of the corresponding vegetation. On the other hand, in areas where snow redistribution by wind is dominant, the scale breaks in the snow depth spectra are displaced towards scales larger than those of the corresponding vegetation. Redistribution of snow by wind leads to the formation of snowdrifts and scour areas over larger scales, affecting the scaling characteristics of the snow depth surface after the snow is initially deposited. The scales at which the switch in the scaling properties of snow depth occurs are comparable to the separation distance

51

between peaks (local maxima above a threshold) in the snow depth profiles. These characteristics support the conclusion that the break in the scaling behavior of snow depth is controlled by the vegetation characteristics (e.g., height, area covered by the canopy, and separation between trees) when wind redistribution is minimal and canopy interception is dominant, and by the interaction of winds with features such as surface concavities and vegetation when wind redistribution is dominant. Such effect of wind redistribution is also evidenced in the directional spectra, with the lowest low-frequencies exponents and the largest scale breaks occurring along the predominant wind directions, as sign of scaling anisotropy and directionality in wind-dominated environments. Until this study, evidence of the links between these processes and the scaling behavior observed in the power spectrum of snow depth in these two type of environments had not been provided.

The results obtained in this study have important implications with respect to processes, measurement and model scales. The existence of a break in the scaling of snow depth at scales of the order of meters to tens of meters indicates a switch in the characteristics of the variability above and below the break. Within each scale interval, similar processes are controlling the variability as indicated by the power law relationship that characterizes the spectrum within each range. If the objective is to reveal small-scale processes such as vegetation interception by individual trees and wind interaction with small features such as surface concavities, trees and rocks, measurement and model scales should be selected within the high-frequency range. In this way, the details of the snow depth surface between the peaks can be revealed. If the objective is to represent the average effect of processes such as canopy interception of snowfall and snow

redistribution due to wind, measurement and model scales should be selected within the low-frequency range. For practical purposes in hydrologic applications, accurate description of the small-scale interactions might not be necessary and the detailed information required to reproduce such processes might not be available. Model and measurement scales should be selected according to such objectives. Further analysis of spatially distributed data for different times in the season and larger spatial scales is required to expand the characterization of the variability of snow properties.

2.8 Appendix

Scale invariant systems are systems whose (statistical) properties at different scales are related by a scale-changing operation involving only a scale ratio. Statistical scale invariance can be expressed as [e.g., *Voss*, 1985b]

$$[V(t + b\Delta t) - V(t)] \overset{d}{=} b^{H}[V(t + \Delta t) - V(t)] \qquad (2.\text{A1})$$

where *b* is a scale factor, *H* is the Hausdorff exponent, and $\overset{d}{=}$ indicates that the two sides of the expression possess the same probability distribution function. Self-similarity corresponds to the particular case of *H* equal to 1, implying isotropic rescaling for the two coordinates, *t* and *V*. On the other hand, self-affinity corresponds to the case in which each coordinate is rescaled by a different scale ratio, i.e., *H* other than 1. These concepts can be extended to higher Euclidian dimensions by replacing *t* with a more general vector $\mathbf{x} = (x_1, x_2, ..., x_E)$ in an E dimensional space, leading to the following expression [e.g., *Voss*, 1985a, 1985b]:

$$[V(\mathbf{x} + b\Delta\mathbf{x}) - V(\mathbf{x})] \overset{d}{=} b^{H}[V(\mathbf{x} + \Delta\mathbf{x}) - V(\mathbf{x})] \qquad (2.\text{A2})$$

Equation (2.A2) implies scaling isotropy along the coordinates of the vector $\mathbf{x}$ as the exponent *H* is constant along any component of $\mathbf{x}$ but allows for scaling anisotropy (i.e., self-affinity) with respect to *V* as *H* may be different from 1. Scaling anisotropy or self-affinity may arise when the coordinates are not equivalent (e.g., $\mathbf{V}$ and $\mathbf{x}$, or $\mathbf{x}$ and *t*), or when different processes affect the variability along different directions. Such anisotropy can be analyzed by looking at the scaling properties (e.g., spectral exponent) along each

54

coordinate independently or by analyzing the changes of such properties along different directions (e.g., different combinations of x and y).

For a self-affine function of one variable (e.g., t as in (2.A1)) the power spectral density $P(k)$ follows a power law dependence on the wave number k as [e.g., Voss, 1985a, 1985b]

$$P(k) \ \propto \ k^{-\beta} \qquad (2.A3)$$

Similarly, the two-dimensional power spectra of self-affine functions in the x-y plane where all directions in the x-y plane are equivalent also obey a power law as

$$P(k) \ \propto \ \left(k_x^2 \ + \ k_y^2\right)^{-\beta/2} \ = \ (k)^{-\beta}$$
$$k \ = \ \left(k_x^2 \ + \ k_y^2\right)^{1/2} \qquad (2.A4)$$

but with a spectral exponent that differs by 1 with respect to the corresponding one-dimensional exponent [e.g., Voss, 1985b]. Also observe that now k stands for a general wave number. A more general form of (2.A4) allows also for scaling anisotropy along each of the components of the vector $\mathbf{x}$ as [e.g., De Michele and Bernardara, 2005]

$$P\left(k_x, k_y\right) \propto \left(\alpha_x^2 k_x^2 + \alpha_y^2 k_y^2\right)^{-\beta/2} \qquad (2.A5)$$

In the case of fractional Brownian motion, the one-dimensional spectral exponent and the Hausdorff exponent are related as [e.g., Voss, 1985a, 1985b]

$$\beta \ = \ 2H \ + \ 1 \qquad (2.A6)$$

The spectral exponent can be used as a measure of the persistence for all values of β. Functions with low spectral exponents are highly variable and adjacent values are less correlated. As the exponent increases, the functions become smoother and adjacent values become more correlated. Low spectral exponents imply a more uniform

contribution of all frequencies to the variability of the series, leading to a 'rougher' pattern with high-frequency (short wavelengths) variations of similar orders of magnitude as the low-frequency variations (long wavelengths). As the exponent increases, the contributions of the low frequencies become increasingly dominant over the contributions of the short frequencies, and as a consequence the correlation between adjacent values of the series increases and the profile becomes smoother. Weak long-range persistence corresponds to $0 < \beta < 1$, whereas strong long-range persistence corresponds to $\beta > 1$. The value of the spectral exponent also has important implications with respect to the convergence or divergence of the variance [e.g., *Malamud and Turcotte*, 1999]. The variance converges for $\beta < 1$, and diverges for $\beta > 1$. Self-affine time series with $\beta < 1$ are stationary while series with $\beta > 1$ are nonstationary, and $\beta = 1$ can be used as a crossover between weak and strong persistence in time series [*Malamud and Turcotte*, 1999].

Spectral techniques are often preferred over other techniques, such as variogram analysis, for the study of the scaling properties of random fields. This is because, depending on the value of β, different techniques are more or less accurate in estimating the scaling properties of fields. In the case of variogram analysis, the range of β for which one can expect reasonably accurate results is $1.2 < \beta < 2.5$, whereas spectral techniques are accurate for all values of β [e.g., *McSharry and Malamud*, 2005]. Spectral techniques have been used to explore the scaling characteristics of highly variable processes such as rainfall rate [e.g., *Crane*, 1990; *Veneziano et al.*, 1996], topography [e.g., *Brown*, 1987;

Turcotte, 1987, 1989; *Huang and Turcotte*, 1989], soil moisture [*Kim and Barros*, 2002],

and groundwater base flow [e.g., *Zhang and Schilling*, 2004; *Zhang and Li*, 2005].

2.9 Acknowledgements

2.10 References

Arnold, N. S., and W. G. Rees (2003), Self-similarity in glacier surface characteristics, *J. Glaciol.*, *49*(167), 547-554.

Blöschl, G. (1999), Scaling issues in snow hydrology, *Hydrolog. Process.*, *13*, 2149-2175.

Blöschl, G., and R. Kirnbauer (1992), An analysis of snow cover patterns in a small alpine catchment, *Hydrolog. Process.*, *6*, 99-109.

Brown, S. R. (1987), A note on the description of surface roughness using fractal dimension, *Geophys. Res. Lett.*, *14*(11), 1095-1098.

Cline, D., and Cold Land Processes working group (2001), Cold Land Processes field experiment plan, *http://www.nohrsc.nws.gov/~cline/clpx.html.*

Crane, R. (1990), Space-Time structure of rain rate fields, *J. Geophys. Res.*, *95*(D3), 2011-2020.

De Michele, C., and P. Bernardara (2005), Spectral analysis and modeling of space-time rainfall fields, *Atmos. Res.*, *77*, 124-136.

Deems, J. S., S. R. Fassnacht, and K. J. Elder (2006), Fractal Distribution of Snow Depth from Lidar Data, *J. Hydrometeor.*, *7*, 285-297.

Elder, K., J. Dozier, and J. Michaelsen (1991), Snow accumulation and distribution in an alpine watershed, *Water Resour. Res.*, *27*, 1541–1552.

Elder, K., J. Michaelsen, and J. Dozier (1995), Small basin modeling of snow water equivalence using binary regression tree methods, *Proc. Symp. on Biogeochemistry of Seasonally Snow-Covered Catchments*, IAHS-AIHS and IUGG XX General Assembly, IAHS Publication 228, pp. 129–139, Boulder, CO.

Elder, K., W. Rosenthal, and R. Davis (1998), Estimating the spatial distribution of snow water equivalence in a montane watershed, *Hydrolog. Process.*, *12*(10-11), 1793-1808.

Erickson, T. A., M. W. Williams, and A. Winstral (2005), Persistence of topographic controls on the spatial distribution of snow in rugged mountain terrain, Colorado, United States, *Water Resour. Res.*, *41*, W04014, doi:10.1029/2003WR002973.

Erxleben, J., K. Elder, and R. Davis (2002), Comparison of spatial interpolation methods for estimating snow distribution in the Colorado Rocky Mountains, *Hydrolog. Process.*, *16*, 3627-3649.

Evans, B. M., D. A. Walker, D. S. Benson, E. A. Nordstrand, and G. W. Petersen (1989), Spatial interrelationships between terrain, snow distribution and vegetation patterns at an artic foothills site in Alaska, *Holarctic. Ecol.*, *12*, 270-278.

Granger, R. J., J. W. Pomeroy, and J. Parviainen (2002), Boundary-layer integration approach to advection of sensible heat to a patchy snow cover, *Hydrolog. Process.*, *16*, 3559-3569.

Greene, E. M., G. E. Liston, and R. A. Pielke Sr. (1999), Relationships between landscape, snow cover depletion, and regional weather and climate, *Hydrolog. Process.*, *13*, 2453-2466.

Hosang, J., and K. Dettwiler (1991), Evaluation of a water equivalent of snow cover map in a small catchment-area using geostatistical approach, *Hydrolog. Process.*, *5*, 283-290.

Huang, J., D. L. Turcotte (1989), Fractal mapping of digitized images: application to the topography of Arizona and comparison with synthetic images *J. Geophys. Res.*, *94*(B6), 7491-7495.

Kang, B., and J. A. Ramírez (2001), Comparative study of the statistical features of random cascade models for spatial rainfall downscaling, *Proc. AGU Hydrology Days 2001*, edited by J. A. Ramírez, pp. 151-164, Hydrology Days Publications, Fort Collins, CO.

Kim, G., and A. P. Barros (2002), Downscaling of remotely sensed soil moisture with a modified fractal interpolation method using contraction mapping and ancillary data, *Rem. Sens. Environ.*, *83*, 400-413.

Kuchment, L. S., and A. N. Gelfan (2001), Statistical self-similarity of spatial variations of snow cover: verification of the hypothesis and application in the snowmelt runoff generation models, *Hydrolog. Process.*, *15*, 3343-3355.

Liston, G. E. (1999), Interrelationships among snow distribution, snowmelt, and snow cover depletion: Implications for atmospheric, hydrologic, and ecologic modeling, *J. Appl. Meteorol.*, *38*(10), 1474-1487.

Liston, G. E., and M. Sturm (1998), A snow-transport model for complex terrain. *J. Glaciol.*, *44*(148), 498-516.

Liston, G. E., R. A. Pielke, Sr., and E. M. Greene (1999), Improving first-order snow-related deficiencies in a regional climate model, *J. Geophys. Res.*, *104*(D16), 19559-19567.

Lovejoy, S, and D. Schertzer (1985), Generalized scale invariance in the atmosphere and fractal models of rain, *Water Resour. Res.*, *21*(8), pp. 1233-1240.

Luce, C. H., and D. G. Tarboton (2001), Modeling snowmelt over an area: modeling subgrid scale heterogeneity in distributed model elements, *Proc. of MODSIM 2001*, pp.341-346, International Congress on Modelling and Simulation, Canberra, Australia, December 10-13.

Luce, C. H., and D. G. Tarboton (2004), The application of depletion curves for parameterization of subgrid variability of snow, *Hydrolog. Process.*, *18*, 1409–1422.

Luce, C. H., D. G. Tarboton, and K. R. Cooley (1997), Spatially distributed snowmelt inputs to a semi-arid mountain watershed, *Proc. of the Western Snow Conference*, Banff, Canada, May 5-8, 1997.

Luce, C. H., D. G. Tarboton, and K. R. Cooley (1998), The influence of the spatial distribution of snow on basin-averaged snowmelt, *Hydrolog. Process.*, *12*, 1671–1683.

Luce, C. H., D. G. Tarboton, and K. R. Cooley (1999), Sub-grid parameterization of snow distribution for an energy and mass balance snow cover model, *Hydrolog. Process.*, *13*, 1921-1933.

Malamud, B. D., D. L. Turcotte (1999), Self-affine time series: measures of weak and strong persistance, *J. Stat. Plann. Infer.*, *80*, 173-196.

Mandelbrot, B. (1967), How long is the coast of Britain? Statistical self-similarity and fractional dimension, *Science*, 156, 636-638.

Mandelbrot, B. (1982), *The Fractal Geometry of Nature*, 468 pp., Freeman, San Francisco.

Marsan, D., D. Schertzer, and S. Lovejoy (1996), Causal space-time multifractal processes: Predictability and forecasting of rain fields, *J. Geophys. Res.*, *101*(D21), 26333-26346.

McSharry, P. E., and B. D. Malamud (2005), Quantifying self-similarity in cardiac inter-beat interval time series, *Comput. Cardiol.*, *32*, 459-462.

Meng, H., J. A. Ramírez, J. D. Salas, and L. Ahuja (1996), Scaling analysis of infiltration at R-5 catchment, *Invited Proceedings of the USDA-ARS Workshop on Real World Infiltration*, Pingree Park, CO, July 22-25. CWRRI Information Series No. 86, pp. 239-240.

Miller, S.L. (2003), *CLPX-Airborne: Infrared Orthophotography and LIDAR Topographic Mapping*, National Snow and Ice Data Center. Digital Media, Boulder, CO.

Molnar, P., and J. A. Ramírez (1998), Energy dissipation theories and optimal channel characteristics of river networks, *Water Resour. Res.*, *34*(7), pp. 1809-1818.

Over, T. M. (1995), Modeling space-time rainfall at the mesoscale using random cascades, Ph.D. thesis, University of Colorado, Boulder.

Over, T. M., and V. K. Gupta (1996), A space-time theory of mesoscale rainfall using random cascades, *J. Geophys. Res.*, *101*(D21), 26319-26332.

Rodríguez-Iturbe, I., G. K. Vogel, R. Rigon, D. Entekhabi, F. Castelli, and A. Rinaldo (1995), On the spatial organization of soil moisture fields. *Geophys. Res. Lett.*, *22*(20), 2757-2760.

Rodríguez-Iturbe, I.; and A. Rinaldo (1996), *Fractal River Basins*, 564 pp., Cambridge University Press, Cambridge, United Kingdom.

Shook, K., and D. M. Gray (1994), Determining the snow water equivalent of shallow prairie snowcovers, paper presented at 51st Eastern Snow Conference, Dearborn, Mich., June 14–16.

Shook, K, and D. M. Gray (1996), Small-scale spatial structure of shallow snowcovers, *Hydrolog. Process.*, *10*, 1283-1292.

Shook, K, and D. M. Gray (1997), Synthesizing shallow seasonal snow covers, *Water Resour. Res.*, *33*(3), 419–426.

Shook, K., D. M. Gray, and J. W. Pomeroy (1993), Temporal variation in snowcover area during melt in Prairie and Alpine environments, *Nord. Hydrol.*, *24*, 183–198.

Tarboton, D. G., R. L. Bras, and I. Rodríguez-Iturbe (1988), The fractal nature of river networks, *Water Resour. Res.*, *24*(8), 1317-1322.

Tessier, Y., S. Lovejoy, and D. Schertzer (1993), Universal multifractals: Theory and observations for rain and clouds, *J. Appl. Meteorol.*, *32*(2), 223-250.

Turcotte, D. L. (1987), A fractal interpretation of topography and geoid spectra on the earth, moon, venus, and mars, *J. Geophys. Res.*, *92*(B4), E597-E601.

Turcotte, D. L. (1989), Fractals in geology and geophysics, *Pure Appl. Geophys.*, *131*(1), 171-196.

Veneziano, D., and V. Iacobellis (1999), Self-similarity and multifractality of topographic surfaces at basin and subbasin scales, *J. Geophys. Res.*, *104*(B6), 12797-12812.

Veneziano, D., R. L. Bras, and J. D. Niemann (1996), Nonlinearity and self-similarity of rainfall in time and a stochastic model, *J. Geophys. Res.*, *101*(D21), 26371-26392.

Voss, R. F. (1985a), Random fractals: characterization and measurement, in *Scaling Phenomena in Disordered Systems*, edited by R. Pynn and A. Skjeltorp, pp. 1-11, Plenum Press, New York.

Voss, R. F. (1985b), Random fractal forgeries, in *Fundamental Algorithms for Computer Graphics*, NATO ASI Series, Vol. F17, edited by R. A. Earnshaw, pp. 805-835, Springer-Verlag, Berlin Heidelberg.

Winstral, A., K. Elder, and R. Davis (2002), Spatial snow modeling of wind-redistributed snow using terrain-based parameters, *J. Hydrometeor.*, *3*, 524-538.

Zhang, Y. K., Z. Li (2005), Temporal scaling of hydraulic head fluctuations: Nonstationary spectral analyses and numerical simulations, *Water Resour. Res.*, *41*, W07031, doi:10.1029/2004WR003797.

Zhang, Y. K., K. Schilling (2004), Temporal scaling of hydraulic head and river base flow and its implication for groundwater recharge, *Water Resour. Res.*, *40*, W03504, doi:10.1029/2003WR002094.

3 Scaling Properties and Spatial Organization of Snow Depth Fields in Sub-alpine Forest and Alpine Tundra

3.1 Abstract

In this study, we analyze the spatial distribution functions, the correlation structures, and the power spectral densities of high-resolution LIDAR snow depths ($\sim$ 1 m) in two adjacent 500 m x 500 m areas in the Colorado Rocky Mountains, one a sub-alpine forest the other an alpine tundra. We show how and why differences in the controlling physical processes induced by variations in vegetation cover and wind patterns lead to the observed differences in spatial organization between the snow depth fields of these environments. In the sub-alpine forest area, the mean of snow depth increases with elevation, while its standard deviation remains uniform. In the tundra subarea, the mean of snow depth decreases with elevation, while its standard deviation varies over a wide range. The two-dimensional correlations of snow depth in the forested area indicate little spatial memory and isotropic conditions, while in the tundra they indicate a marked directional bias that is consistent with the predominant wind directions and the location of topographic ridges and depressions. The power spectral densities exhibit a power law behavior in two frequency intervals separated by a break located at a scale of around 12 m in the forested subarea, and 65 m in the tundra subarea. The spectral exponents obtained indicate that the snow depth fields are highly variable over scales larger than the scale break, while highly correlated below. Based on the observations and on synthetic

snow depth fields generated with one- and two-dimensional spectral techniques, we show that the scale at which the break occurs increases with the separation distance between snow depth maxima. In addition, the breaks in the forested area coincide with those of the corresponding vegetation height field, while in the tundra subarea they are displaced towards larger scales than those observed in the corresponding vegetation height field.

3.2 Introduction

Identifying and characterizing the spatial and temporal variations of snow cover properties (e.g., snow depth, snow density, and snow water equivalent (SWE)) and the relationships between such variability and environmental and hydro-meteorological variables is of importance in hydrology and other applications. Better understanding of these relationships allows for improvements in snowmelt modeling [e.g., *Luce et al.*, 1998; *Liston and Sturm*, 1998; *Liston*, 1999; *Greene et al.*, 1999], interpolation of point measurements [e.g., *Elder et al.*, 1998; *Erxleben et al.*, 2002; *Erickson et al.*, 2005], downscaling of remote sensing data and model results [e.g., *McGinnis*, 2004; *Weitzenkamp et al.*, 2008], subgrid scale parameterizations [e.g., *Luce et al.*, 1999; *Liston*, 2004], and design strategies for measuring and monitoring snow properties [e.g., *Xu et al.*, 1993].

One of the most common approaches for such characterization has consisted of determining the statistical relationships between snow properties and topographic and meteorological variables such as elevation, slope, aspect, wind and radiation [e.g., *Evans et al.*, 1989; *Hosang and Dettwiler*, 1991; *Elder et al.*, 1991; *Blöschl and Kirnbauer*, 1992; *Elder et al.*, 1995; *Elder et al.*, 1998; *Erxleben et al.*, 2002; *Winstral et al.*, 2002; *Erickson et al.*, 2005]. More recently, increasing attention has been given to the characterization of the scale invariance of snow properties such as depth [e.g., *Shook and Gray*, 1994, 1996 and 1997; *Kuchment and Gelfan*, 2001; *Arnold and Rees*, 2003; *Deems et al.*, 2006; *Trujillo et al.*, 2007], SWE [e.g., *Shook and Gray*, 1997], and snow-covered

area (SCA) [e.g., *Shook et al.*, 1993; *Shook and Gray*, 1997; *Blöschl*, 1999; *Granger et al.*, 2002]. These studies have been based on the application of variogram and semi-variogram analyses and spectral techniques previously applied to other variables such as rainfall [e.g., *Lovejoy and Schertzer*, 1985; *Tessier et al.*, 1993; *Over*, 1995; *Over and Gupta*, 1996; *Marsan et al.*, 1996; *Kang and Ramirez*, 2001], soil moisture [e.g., *Rodríguez-Iturbe et al.*, 1995], topography [e.g., *Mandelbrot*, 1967, 1982; *Brown*, 1987; *Turcotte*, 1987, 1989; *Huang and Turcotte*, 1989], and steady-state and transient infiltration rates [e.g., *Meng et al.*, 1996].

Among the snow cover properties, snow depth has received most of the attention because it is one of the most spatially variable, and also because it is one of the easiest to measure. Several different techniques have been used for the study of the scale invariance of snow depth, from the analysis of the dependence of the standard deviation of snow depth on sampling distance, to more complex techniques such as variogram and spectral analyses. The types of measurements used range from point data along linear transects obtained in winter field campaigns to high-resolution remote sensing measurements that provide snow depth information over areas of the order of 1-km^2. The summary presented below presents the recent progression of the knowledge provided by these studies, from the first studies by *Shook and Gray* [1994, 1996], to the latest findings by *Trujillo et al.* [2007].

Shook and Gray [1994, 1996] analyzed the standard deviation of snow depth along linear transects in prairie and Arctic environments as a function of sample distance, covering distances of up to 1200 m. Their results indicate a power-law type increase of the standard deviation up to sampling distances of the order of 20 m, after which the

relationship is asymptotic to a slope of 0.06 in the log-log domain. *Shook and Gray* [1996] defined a 'cut-off' length as the point of intersection between the initial slope and a horizontal tangent to the end of the curve in the log-log plot of standard deviation versus sample distance. This definition is used to compare the scale at which the break occurs in different environments, extending the analysis to transects in two other areas with variations in elevation range. Cut-off lengths between 30 m and 500 m were obtained for the three environments. *Shook and Gray* [1996] hypothesized that the autocorrelation structure of snow depth in one of their study areas used for agriculture (stubble) was due to the formation of dunes of snow (i.e., snow drifts), stating that the autocorrelation structure caused by a dune must terminate at scales greater than the length of a dune. They describe the cutoff length as an index of the upper limit of the fractal structure of the fields, and hypothesize that such cutoff length is established primarily by topography in the absence of major changes in vegetation.

Shook and Gray [1996] also suggest that the magnitude of the cutoff length may be related to the degree of large-scale topographic relief, based on an observed increase in the cutoff length with relief for three snow depth transects in three different locations. Additionally, *Shook and Gray* [1996] tested the influence of large-scale trends in snow depth on the cutoff length by de-trending two snow depth transects of about 150 m and 170 m in length. The de-trending consisted of subtracting a linear and a polynomial function of horizontal distance. Before subtracting these trends, the log-log plots of standard deviation of snow depth versus sampling distance demonstrated similar slopes with no breaks for both of the profiles. Once de-trended, the standard deviation of the profiles displayed cutoff lengths at approximately 30 m, with slopes similar to those

obtained for the original data below the cutoff length, and a flatter function above the cutoff length. From the decrease in the cutoff length produced by the de-trending of the profiles, *Shook and Gray* [1996] conclude that the autocorrelation of snow depth is due to both small-scale and large-scale surface features, and that the effect of large-scale features is to increase the cutoff length. On the basis of the similarities of the cutoff lengths obtained for the de-trended data of the fallow and stubble transects, they also suggest that the magnitude of the cutoff distance is relatively insensitive to land use, and that the cutoff length is a measure of the effects of topographic variability on snow accumulation.

Recently, a high-definition (~ 1.5 m separation between observations) dataset of spatially distributed snow depths has become available as part of NASA's Cold Land Processes Experiment (CLPX). The dataset consists of airborne LIght Detection And Ranging (LIDAR) measurements of snow depth, topography and elevation returns to the top of vegetation for nine 1-km^2 intensive study areas (ISA's) located in the state of Colorado (USA) (see Section 3.3 for more details). These data have been used in two recent studies of the scaling characteristics of the spatial distribution of snow depth [*Deems et al.*, 2006; *Trujillo et al.*, 2007] focusing on determining the control that vegetation, topography and winds exert on such scaling characteristics.

Deems et al. [2006] analyzed the variograms of the LIDAR measurements of snow depth, topography and vegetation topography (i.e., elevation + vegetation height) of three of the nine 1-km^2 study areas (i.e., Buffalo Pass, Walton Creek, and Alpine ISA's), in which the spatial distribution of snow depth is strongly influenced by wind redistribution of snow. From the observed log-log linearity of the variograms, they infer fractal

behavior in the elevation, vegetation topography and snow depth datasets. Their analyses seem to indicate the existence of two distinct scale regions with fractal distributions for the snow depth and vegetation topography datasets, separated by a scale break whose location varies between 15 m and 40 m for snow depth, and between 31 m and 56 m for vegetation topography, similar to the results obtained by *Shook and Gray* [1994, 1996], *Kuchment and Gelfan* [2001] and *Arnold and Rees* [2003]. The fractal dimensions obtained for snow depth are of the order of 2.5 for the shorter scale range and 2.9 for the longer scale range. From these values, *Deems et al.* [2006] speculate that for the short range there is a balance between high- and low-frequency variations, while at larger distances the distribution of snow depth approaches a spatially random distribution. They also speculate that the scale breaks in the snow depth variograms indicate a switch from a pattern dominated by short-range vegetation variability to one predominately influenced by longer-range variations in terrain, based on similarities in the behavior of the variograms of vegetation topography. *Deems et al.* [2006] also suggest that the location of the scale break might be related to the overall terrain relief on the basis of an overall increase in the location of the scale break with relief for the three study areas, supporting the hypothesis first proposed by *Shook and Gray* [1996]. They also state that the process change revealed in the terrain–vegetation (topography + vegetation height) data potentially influences the scaling behavior of snow depth patterns, given that the scale break separating the two fractal regions in the terrain–vegetation distributions is of the same order of magnitude as the scale break observed in the snow depth data. Finally, from relatively small variations of the fractal dimensions for different directions of the order of 0.1 in the snow depth, *Deems et al.* [2006] conclude that such variations show a

strong qualitative relationship to prevailing winds and large-scale topographic orientation.

Trujillo et al. [2007] used a similar dataset that includes data from five of the nine 1-km^2 study areas of the CLPX, two of them included in the study by *Deems et al.* [2006], covering a wider range of environments with differences in topography, vegetation and meteorological characteristics. In their study, *Trujillo et al.* analyzed the power spectral densities of the 1-km^2 raster fields of snow depth, topography, topography + vegetation height, and vegetation height, comparing the results obtained for each of these fields and identifying all relationships between them. They complemented their study with an analysis of maximum wind speeds and directions, and of the separation distance between peaks in the snow depth and vegetation height profiles. Also, they compared the spectral characteristics (e.g., spectral exponents and scale breaks) to wind patterns in search for any relationship between the variables. Their analyses show that the spectral densities of snow depth and vegetation height exhibit a similar bilinear power-law behavior separated by scale breaks located at wavelengths of the order of meters to tens of meters. However, a comparison of the location of the scale breaks in the snow depth spectra and the corresponding vegetation height spectra reveals that the scale breaks in the snow depth scaling coincide with those of the vegetation height fields only in environments in which the spatial variability of snow depth is controlled by canopy interception of snowfall, while the break in the snow depth scaling is displaced towards larger scales than those of the corresponding vegetation height fields in environments with a strong influence of wind redistribution of snow. These results are in contrast to those of *Deems et al.* [2006]. *Trujillo et al.* [2007] give explanation to the relationship between the spectral properties

71

of snow depth and vegetation height in environments in which canopy interception of snow is dominant by comparing the empirical probability distributions of the separation distance between peaks in the snow depth and vegetation height profiles of the fields. This comparison shows that the separations between peaks in the profiles of both, vegetation height and snow depth, exhibit similar statistical characteristics as a sign of similar characteristic scales in both fields. They state that such similarities are a consequence of the effect of canopy interception of snow in the distribution of snow depth given that the location of the peaks (maxima) in the vegetation height fields (coincident with the location of trees) coincides with the location of low points (minima) in the snow depth fields in environments in which the distribution of snow depth is strongly influenced by canopy interception of snow. On the other hand, *Trujillo et al.* [2007] show the control that wind patterns exert on the spectral characteristics of snow depth in environments in which wind redistribution of snow is dominant by comparing the distributions of wind direction to the variation of the spectral exponents and scale breaks with direction. Such comparisons reveal a strong relationship between the spectral exponent of the low-frequencies and the location of the scale break with the predominant wind directions as a sign of the influence of wind patterns on the characteristics of the spatial variability of snow depth in such environments. The differences observed in the spectral characteristics (i.e., spectral exponents and scale break) of the snow depth fields between the different environments and the relationship of such characteristics to vegetation indicate that land use plays an important role in determining the scaling characteristics of the spatial distribution of snow depth, especially in environments in which canopy interception of snow depth is dominant, contrary to what was proposed by

Shook and Gray [1996]. Furthermore, *Trujillo et al.* [2007] demonstrated that the location of the scale break is a measure of the separation distance between high points or peaks in the snow depth surface, and that the characteristics of the variations in the snow depth fields change above and below such characteristic scales. These results corroborate *Shook and Gray*'s [1996] suggestions that the change in the autocorrelation structure of snow depth in environments with the influence of wind redistribution is caused primarily by the formation of dunes (i.e., snowdrifts), and that the autocorrelation caused by a dune must terminate at scales greater than the length of the dune. Contrary to the suggestion by *Deems et al.* [2006] with respect to the influence of topographic relief on the location of the scale break, *Trujillo et al.* [2007] found no clear relationship between the two variables, as the location of the scale break was demonstrated to be related to other characteristics of the environments.

In this study, differences in the spatial organization of snow depth between a sub-alpine forest and an alpine tundra environment are described and explained based on the analysis of spatial distribution functions, correlation functions, and power spectral densities of high-resolution LIDAR measurements (~ 1 m) obtained within two adjacent 500 m x 500 m study areas located in the Colorado Rocky Mountains. Both of the areas are located in the Alpine ISA of the CLPX and present similar topographic characteristics (e.g., slope and aspect), but different vegetation characteristics and wind patterns. The analysis is complemented by the application of spectral techniques for generating synthetic one-dimensional profiles and two-dimensional fields that reproduce the scaling characteristics (i.e., spectral exponents and scale breaks) observed in the snow depth fields.

3.3   Field Description and Dataset

The data used in this study were collected as part of the Cold Land Processes Experiment (CLPX) in 2003 [*Cline et al*, 2001]. The CLPX was a cooperative effort of NASA, NOAA and other government agencies and universities designed to advance the understanding of the terrestrial cryosphere, providing information to address questions on cold land processes, spatial and temporal variability of the snow cover, and uncertainty of remote sensing measurements and models [*Cline et al*, 2001]. The study area of the CLPX is conformed by a nested array of study areas at five different scale levels in the state of Colorado and a small portion of southern Wyoming. The two first levels correspond to one large and one small regional study areas of 3.5° x 4.5° and 1.5° x 2.5°, respectively. Three Meso-cell study areas (MSA) of 25 km x 25 km and nine 1 km x 1 km intensive study areas (ISA's) conform the third and fourth scale levels, respectively. The last scale level corresponds to one local-scale observation site (LSOS) of 1 ha. This study focuses on the Alpine ISA. Such focus is motivated by the existence of alpine tundra and sub-alpine forest environments within this ISA, each exhibiting different characteristics in the spatial organization of the snow cover. The hypothesis is that those differences result from differences in the controlling physical processes induced by variations in vegetation cover and, consequently, the control of wind patterns on the spatial organization of snow depth.

74
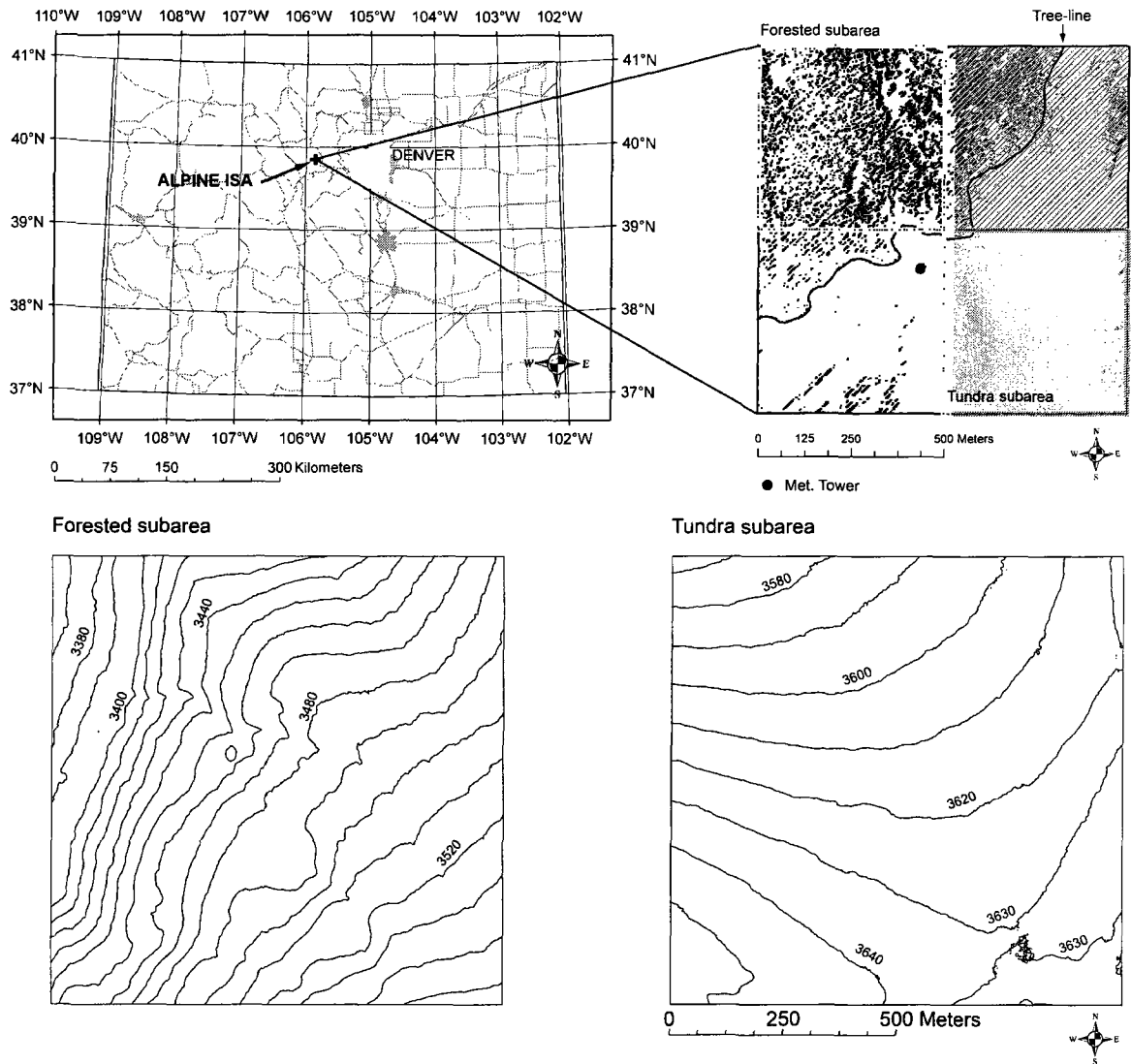
Figure 3.1. Location of the Alpine Intensive Study Area (ISA) of the CLPX in the state of Colorado. The detail shows the aerial photography of the ISA taken on April 8, 2003. Also, boundaries for the forested and the tundra subareas are included. The location of the meteorological tower above the tree-line is marked by the black dot. The topographic contours of the subareas are shown in the bottom panels.

The Alpine ISA is a high-altitude area located in the Fraser MSA in the Colorado Rocky Mountains (Figure 3.1). This ISA is located in the transition between the sub-alpine and the alpine tundra environments, with elevations that range between 3364 m a.s.l. and 3676 m a.s.l.. The tree-line that separates the sub-alpine and the tundra environments is located at about 3565 m a.s.l., with the lower portion covered by a dense coniferous forest, and the higher portion covered by short tundra vegetation (Figure 3.1). Most of the area is on a northwest facing slope, with little aspect variation (Figure 3.2a). Slopes in the ISA are moderate, with 94 % of the area with slope angles of less than 30°, and an average slope angle of 15° (Figure 3.2b). Terrain features such as aspect and slope exhibit little variation within the ISA, and the main difference between the two environments is the vegetation cover. This difference translates in a difference in wind patterns due to the shielding effect that the trees offer.
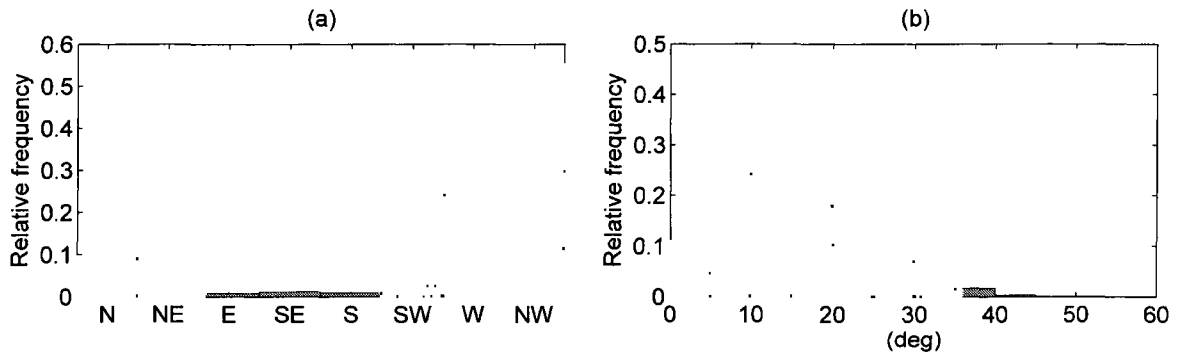
Figure 3.2. Histograms of (a) aspect and (b) slope angle for the entire Alpine ISA.

The dataset used for this study consists of LIDAR elevation returns (filtered to bare ground/snow, and filtered to top of vegetation), elevation contours (0.5 m), and snow

depth contours (0.1 m) [*Miller*, 2003; *Cline et al.*, 2008]. These data were processed from the LIDAR elevation returns with an average horizontal spacing of 1.5 m and vertical tolerance of 0.05 m. The snow depth contours were obtained by subtracting the two topographic surfaces corresponding to snow-covered conditions close to maximum accumulation (April 8, 2003) and no-snow conditions (September 18, 2003). The contour maps were used to generate Triangulated Irregular Network (TIN) surfaces of the fields in ArcGIS, which then were converted to rasters of 1024 by 1024 grid cells covering the entire 1-km^2 area with a grid spacing of approximately 1 m for snow depth, bare ground elevations (topography), and elevation to the top of vegetation (topography + vegetation). Two subareas of 500 m by 500 m were selected within the ISA (Figure 3.1), one being a forested environment the other an alpine tundra environment. The resulting snow depth fields for these study subareas are presented in Figure 3.3.

(a)

(b)

0   62.5   125   250 m

0.0 m   3.3 m

0.0 m   6.3 m
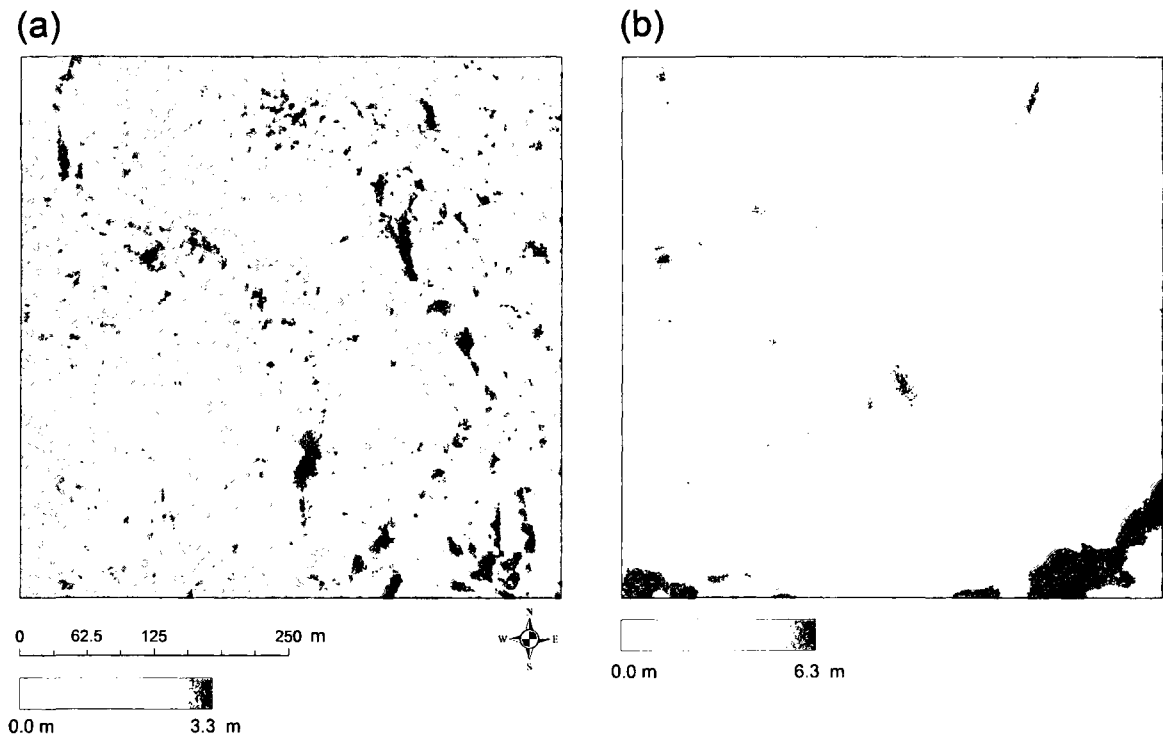
Figure 3.3. Snow depth fields derived from LIDAR for the forested (a) and the tundra (b)

subareas.

In addition, wind data collected as part of the CLPX at a meteorological tower located

in the alpine portion of the ISA (Figure 3.1) are also used. The data correspond to wind

speeds and directions at 1 m above maximum expected snow depth (lower sensor) and 10

m above the ground (upper sensor) for the period October/2002 – April/2003, chosen to

represent the meteorological characteristics between the first snowfalls and the time at

which the LIDAR snow depths were obtained. The empirical distributions of maximum

wind speed at the lower and upper sensors are shown in Figure 3.4, and the distributions

of wind direction are shown in Figure 3.5. Given that snow redistribution due to wind is

only likely to occur when the air temperature is below freezing, only maximum wind

78

speeds and directions for 10-minute intervals with air temperature less than 0° C were analyzed. Average maximum wind speeds are 7.2 m/s at the lower sensor, and 8.3 m/s at the upper sensor, and maximum wind speeds exceed a threshold of 5 m/s 70% of the time at the lower sensor, and 76% of the time at the upper sensor. Such values are evidence of strong wind regimes, with potential for significant redistribution of snow when the snow surface is exposed. Threshold wind speeds (at z = 10 m) for snow transport have been measured to range between 4 m/s and 11 m/s for dry snow conditions, and between 7 m/s and 14 m/s for wet snow conditions [*Li and Pomeroy*, 1997]. The predominant winds in the area flow from the northwest, similar to the predominant topographic aspect of the area (Figure 3.2a).
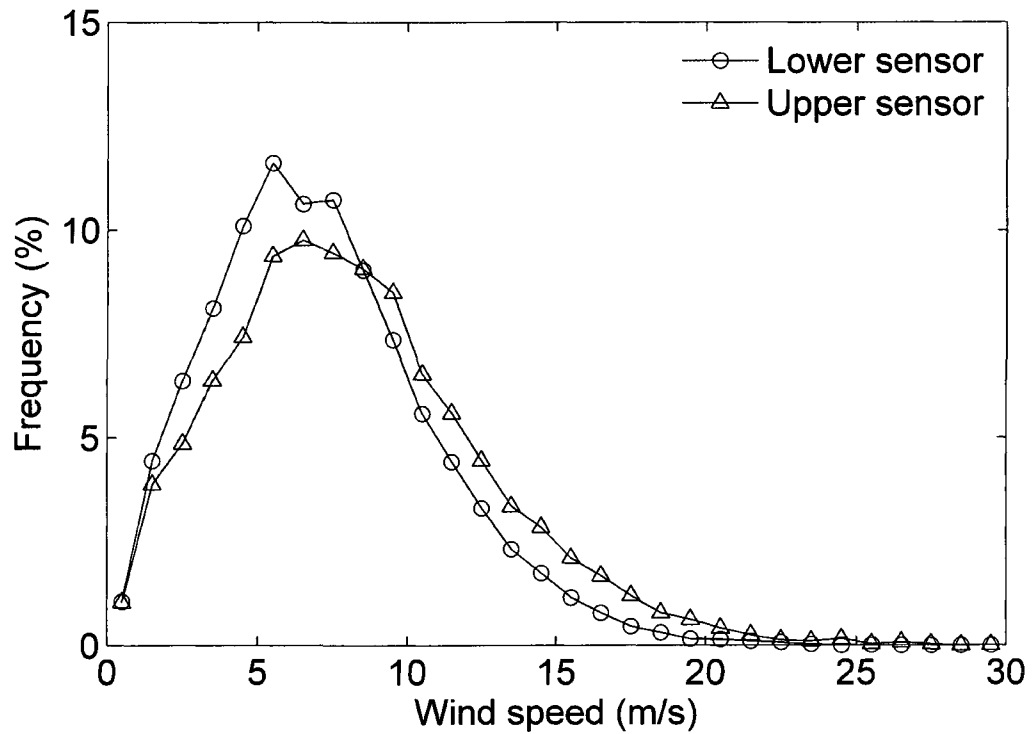
Figure 3.4. Empirical distribution functions of maximum wind speed every 10 minutes for the period October/2002 – April/2003 measured at 1 m above the maximum expected snow depth (lower sensor) and 10 m above the ground (upper sensor). Only data for intervals with air temperature lower than $0°$ C are included. Average speeds are 7.2 m/s at the lower sensor, and 8.3 m/s at the upper sensor.
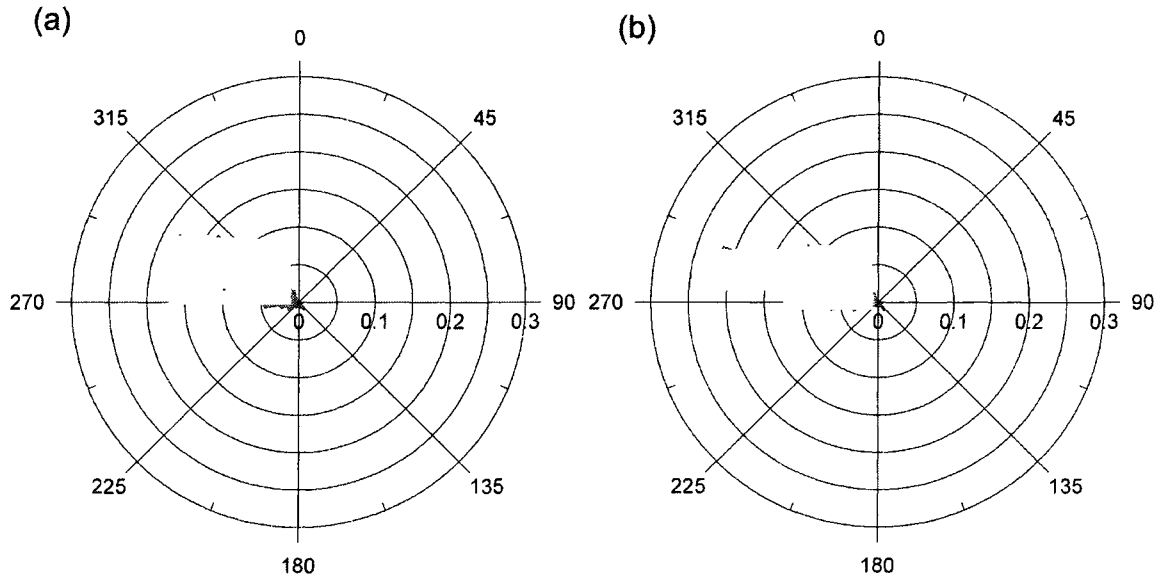
Figure 3.5. Distributions of mean wind direction for 10-minute intervals for the period October/2002 – April/2003 measured at (a) 1 m above the maximum expected snow depth (lower sensor) and (b) 10 m above the ground (upper sensor). Only data for intervals with air temperature lower than $0°$ C. The radial scale corresponds to the relative frequency. The distributions shown were obtained for the dataset without a minimum threshold wind speed. Similar distributions are obtained for wind speeds above thresholds of 4 m/s and 5 m/s. $0°$ corresponds to the North direction.

3.4 Spatial Analysis

3.4.1 Spatial Distributions

The histograms of snow depth for the forested and tundra subareas are shown in Figure 3.6, and summary statistics are presented in Table 3.1. The distribution of snow depth in the forested subarea is approximately Gaussian, with snow depths between 0 m

and 3.3 m, and a mean of 1.62 m. On the other hand, the distribution for the tundra subarea resembles a negatively skewed truncated distribution, with snow depths between 0 m and 6.3 m, and a mean of 1.20 m. The standard deviation is greater in the tundra subarea, with a value of 0.65 m, compared to 0.33 m in the forested subarea. When mean and standard deviation are analyzed as a function of elevation (Figure 3.7), additional differences can be observed. In the forested portion, the mean snow depth increases at an average rate of 2.0 m per 1000 m elevation. The trend reverses in the tundra portion, where the mean snow depth decreases with elevation from about 1.8 m at 3555 m a.s.l. to almost zero at 3676 m a.s.l., although with large variations in the overall trend. The standard deviation also shows a clear change in the behavior above the tree-line. Below the tree-line, the standard deviation remains relatively constant with elevation, with values that range between 0.3 m and 0.4 m, while above the tree-line in the tundra subarea, there is an overall increase with values that are highly variable and with maxima close to 1.6 m, indicating larger variations around the mean in the tundra environment.
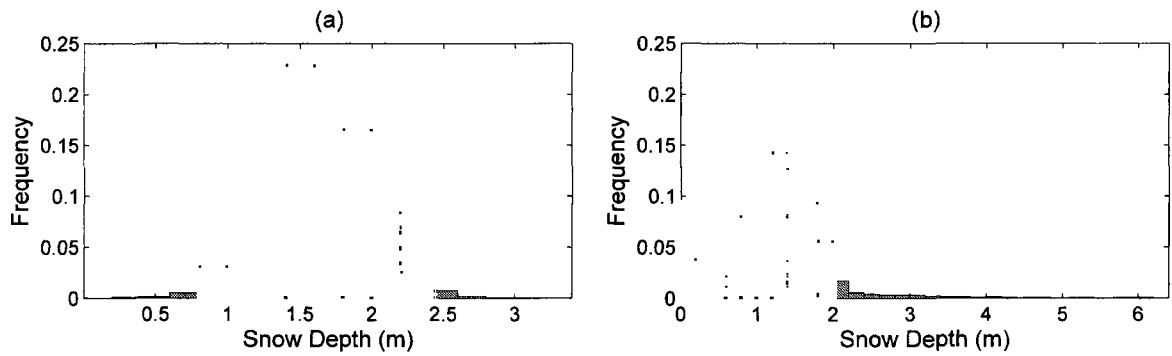
Figure 3.6. Histograms of snow depth for the forested (a) and tundra (b) subareas. A summary of the statistics for these distributions is presented in Table 3.1.

Table 3.1. Snow depth statistics in the forested and tundra subareas. All values but the coefficient of variation (CV) are in meters.

	Mean	Std. Dev.	CV	Min.	Max.
Forested	1.62	0.33	0.20	0.0	3.3
Tundra	1.20	0.65	0.54	0.0	6.3
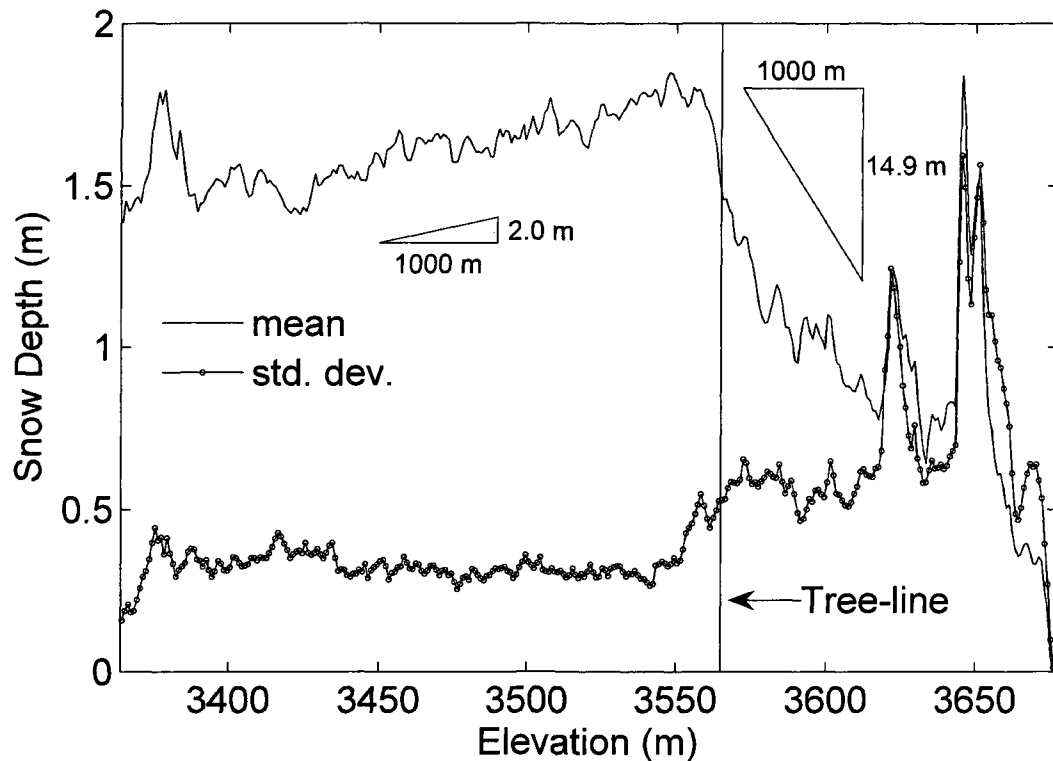
Figure 3.7. Mean and standard deviation of snow depth as a function of elevation obtained for the entire Alpine ISA. The figure illustrates the significant change in the characteristics of the snow cover above the tree-line, located at about 3565 m a.s.l..

The differences in the statistical characteristics of the two snow depth fields can be explained by the differences between the two environments. The effect of the strong winds on the spatial distribution of snow depth is conditioned by the vegetation characteristics, as confirmed by the patterns that can be observed in Figure 3.3. In the tundra environment above the tree line, the snow depth field is characterized by a pattern of snowdrifts and scour areas aligned with the location of ridges and depressions and perpendicular to the predominant wind direction, while the snow depth field in the forested subarea exhibits a pattern dominated by small-scale variability consistent with

84

the location of trees, with little or no sign of snow redistribution by wind due to the shielding effect of the forest. The relatively constant standard deviation with elevation below the tree-line is a sign of similar characteristics in the spatial variability of snow depth throughout the forested subarea due to the relatively uniform characteristics of the vegetation. On the other hand, the decreasing trend in the mean snow depth with elevation in the tundra subarea is evidence of the effect of snow redistribution by wind. Due to the predominant wind directions and the overall terrain aspect, the snow of the tundra subarea is transported uphill, not only leading to the formation of snowdrifts and eroded areas, but also blowing a significant portion of the snow out of the ISA to be deposited on the lee side of the mountain, located to the southeast of the ISA. Also, the redistribution of snow by wind induces losses associated with the sublimation of blowing snow, which have been measured to account for annual losses from 9 % to 47 % of the annual precipitation [*Benson*, 1982; *Pomeroy and Gray*, 1995; *Liston and Sturm*, 1998; *Pomeroy et al.*, 1998; *Essery et al.*, 1996]. These processes cause a decrease in the mean snow depth above the tree-line, which becomes more evident as elevation increases, as the distance from the tree-line increases (commonly referred to as fetch), and the eroding and transport potential of the wind also increases. Similarly, the overall increase in the standard deviation above the tree-line and the large variations of the mean and standard deviation with elevation are evidence of the pattern of snow drifts and scour areas throughout the tundra environment that are responsible for the large variations of the snow depth around the mean.

3.4.2 Two-dimensional Autocorrelation Functions

The two-dimensional autocorrelation functions of snow depth are shown in Figure 3.8 for lags up to ± 100 m in the x and y directions. The correlation function of snow depth in the forested environment exhibits a rapid decay, reaching values of around 0.2 at lags of the order of 10 m. On the other hand, the correlation function of snow depth in the tundra environment shows a slower decay indicating a smoother surface with longer spatial memory. These results indicate that the variations in snow depth occur over much shorter scales in the forested subarea, which can also be observed in the snow depth fields shown in Figure 3.3. The two-dimensional correlation function also provides information about the directionality of the snow depth fields in the two environments. The correlation function in the forested environment shows little anisotropy, as the contour lines above a correlation value of 0.3 are concentric and relatively circular, while the correlation function for the tundra environment shows an anisotropic decay that follows a gradient in the north-western direction (equivalent to the south-eastern gradient). Such directionality in the tundra subarea is consistent with the predominant wind directions (Figure 3.5) and the overall topographic aspect (Figure 3.2a). The weakest correlation structure (fastest decay) of the snow depth field in the tundra environment occurs along a direction parallel to the predominant wind direction, while the strongest correlation structure occurs along the direction perpendicular to the predominant wind direction.
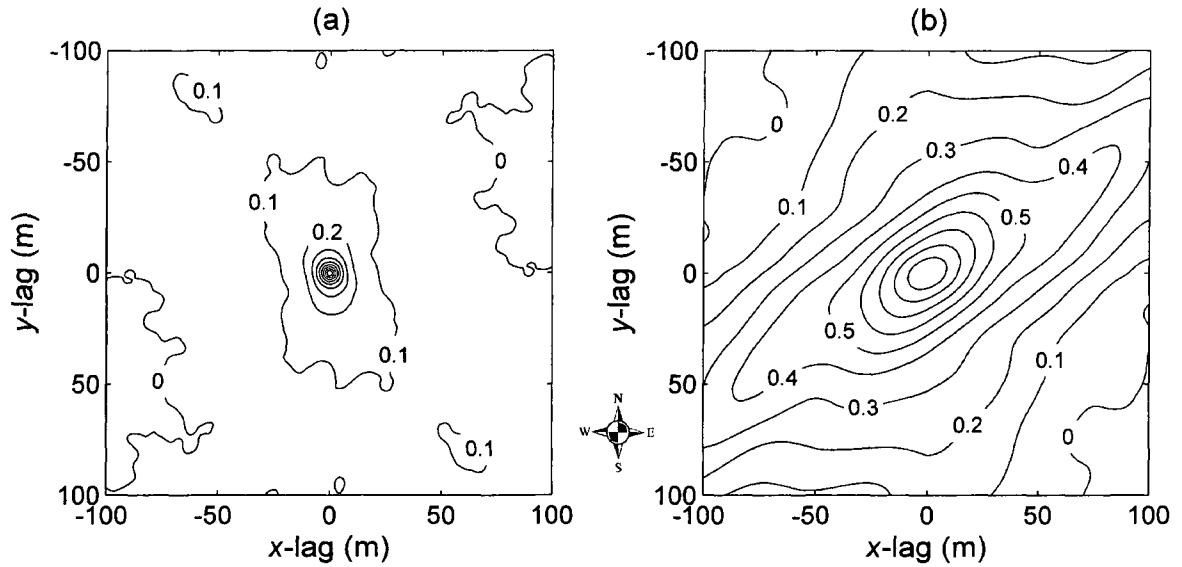
Figure 3.8. Contour maps of the two-dimensional correlograms of snow depth for (a) the forested subarea, and (b) the tundra subarea.

3.4.3 One-Dimensional and Mean Two-Dimensional Power Spectra

Spectral techniques have been used in the study of highly variable processes to determine scaling ranges, spectral slopes, fractal dimensions and Haussdorf exponents. Spectral techniques are applied in this study in two different ways. For the one-dimensional case, one-dimensional power spectral densities were obtained separately for each of the west to east (x) rows and each of the north to south (y) columns of the fields, and then averaged over each direction for each of the square subareas. For the two-dimensional case, the mean two-dimensional power spectral density was determined as the radial average of the two-dimensional spectral density, determined from the two-dimensional Fourier transform of the fields. The methodologies followed for the one- and two-dimensional spectral analyses presented here are described in detail in *Trujillo et al.*

87

[2007]. This spectral analysis was applied to the fields of snow depth and vegetation height in order to compare the scaling behavior of the two fields.
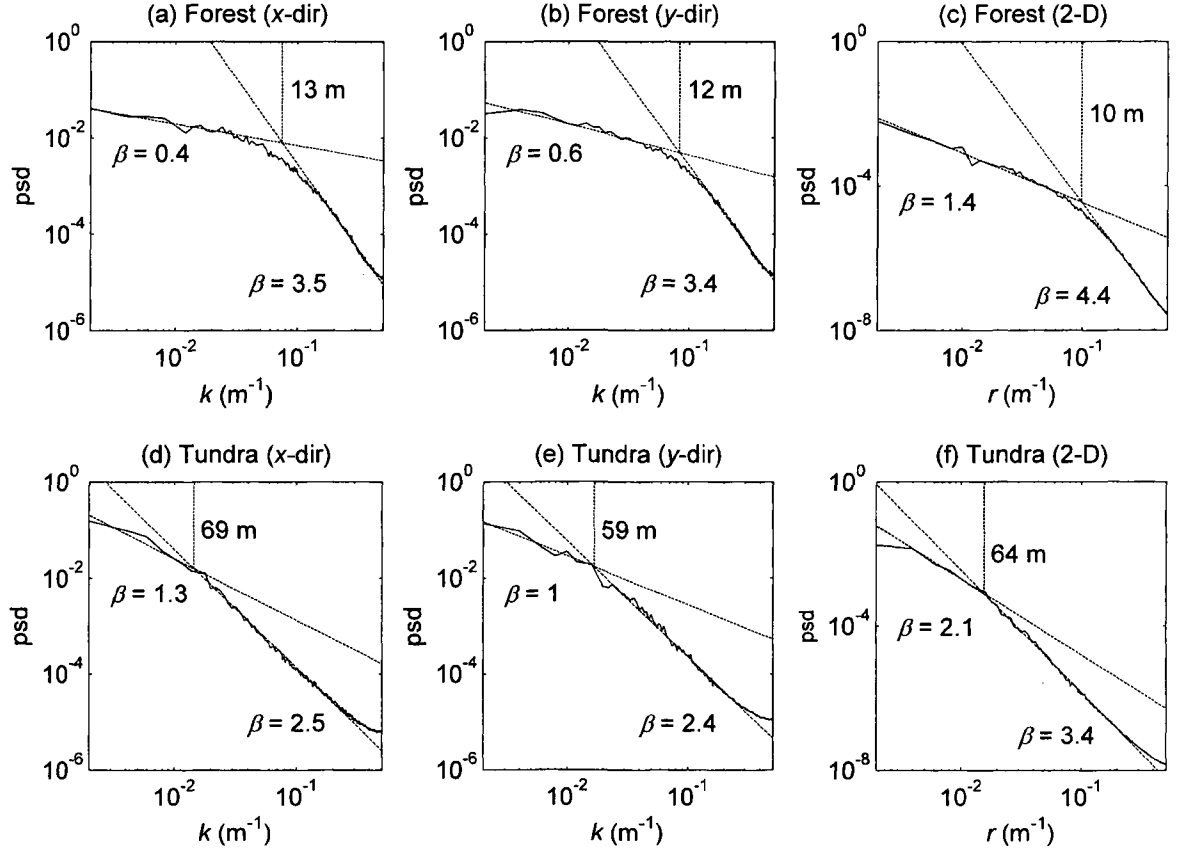
Figure 3.9. One-dimensional and mean two-dimensional power spectral densities of snow depth for the forested and alpine tundra subareas.

The log-log plots of the one- and two-dimensional power spectral densities of snow depth are shown in Figure 3.9. The power spectra of the snow depth fields behave like $k^{-\beta}$ within two scale intervals, each characterized by a different spectral exponent (k is the wave number divided by the length of the profiles, and it represents the spatial scale or wavelength under consideration, and β is the spectral exponent and characterizes the

degree of variability). For the one-dimensional case, the spectral exponents in the forested subarea for the low-frequencies interval are 0.4 and 0.6 for the x and y directions, respectively, while they are 3.5 and 3.4 for the x and y directions, respectively, for the high-frequencies interval. The break that separates the two intervals is located at a spatial scale of about 12 m. For the tundra subarea, the low-frequency spectral exponents are 1.3 and 1.0 for the x and y directions, respectively, while they are 2.5 and 2.4 for the high-frequency interval for the x and y directions, respectively. The scale breaks are located at 69 m and 59 m for the x and y directions, respectively. The one-dimensional spectral exponents obtained for the low-frequency intervals indicate that for points separated by distances larger than the scale of the break, the corresponding snow depths are weakly correlated. The snow depth profiles are highly variable over scales larger than the scale of the break. On the other hand, the high-frequency spectral exponents indicate that for points that are closer than the break, the corresponding snow depth values are highly correlated. The profiles become smoother below the corresponding break. The change in the characteristics of the variability occurs at scales of the order of 10 meters for the forested subarea of several tens of meters for the tundra subarea.

For the two-dimensional case, the low- and high-frequency spectral exponents for the snow depth field of the forested subarea are 1.4 and 4.4, respectively, while they are 2.1 and 3.4, respectively, for the tundra subarea. The breaks are located at 10 m for the forested subarea, and at 64 m for the tundra subarea. The magnitudes of the observed one- and two-dimensional spectral exponents differ approximately by one, as expected theoretically for isotropic fields [e.g., *Voss*, 1985].

The breaks in the one- and two-dimensional spectra of the snow depth fields of the two subareas are located within the same range found in the studies of the spatial scale-invariance of snow depth along linear transects [*Shook and Gray*, 1994, 1996 and 1997; *Arnold and Rees*, 2003] and snow depth fields [*Deems et al.*, 2006; *Trujillo et al.*, 2007]. However, the scale breaks for the snow depth field of the tundra environment are located at larger spatial scales than those of the forested subarea, similar to what was found by *Trujillo et al.* [2007], indicating longer characteristic scales in the snow depth field of the tundra subarea. This observation is consistent with what is observed in the two-dimensional correlation functions (Figure 3.8).

The last of the spectral analyses explores the scaling properties of the vegetation height fields. This analysis indicates that the power spectra of the vegetation height fields also behave like k^{β} within two frequency intervals, with a low-frequency interval characterized by slopes between 0.5 and 0.8 for the one-dimensional case, and between 1.3 and 1.6 for the two-dimensional case, and a high-frequency interval with slopes between 2.9 and 3.4 for the one dimensional case, and between 3.7 and 4.0 for the two-dimensional case (Table 3.2). The locations of the breaks in the forested subarea coincide with those of the snow depth field, while in the tundra subarea the breaks occur at scales larger than those observed for the corresponding snow depth field. Therefore, the spatial organization of vegetation height and snow depth are similar in the forested subarea, as the spectral exponents and scale breaks are within the same ranges. *Trujillo et al.* [2007] obtained similar results from the analysis of the power spectral densities of snow depth and vegetation height in five 1-km^2 areas. They showed that the similarities in the spectral properties of the vegetation height and snow depth fields in forested

environments are a consequence of canopy interception because the location of the peaks (maxima) in the vegetation height fields (coincident with the location of trees) coincides with the location of low points (minima) in the snow depth fields. The results presented here further confirm the control that vegetation and wind redistribution of snow exert in the spatial scaling characteristics of snow depth.

Table 3.2. Summary of the spectral characteristics for the vegetation height fields in the forested and tundra subareas.

Forested	x	y	2-D
Low-frequency β	0.5	0.6	1.3
High-frequency β	3.3	3.4	4.0
Scale break (m)	9	10	8
Tundra	x	y	2-D
Low-frequency β	0.8	0.8	1.6
High-frequency β	2.9	2.9	3.7
Scale break (m)	14	15	14

3.4.4 Synthetic Snow Depth Profiles and Fields

To help understand the implications of the observed one- and two-dimensional power spectra, synthetic snow depth profiles and snow depth fields with bilinear spectral densities, and with variations in the spectral exponents and the scale of the break were generated. The spectral generation techniques are presented in the Appendix.

3.4.4.1 Snow Depth Profiles

In Figure 3.10 the effect of the scale of the break is shown with a series of profiles with low-frequency spectral exponent (β_1) of 0.0 and a high-frequency spectral exponent

(β_2) of 3.5. These values allow for a separation of a larger-scale interval that is highly variable and uncorrelated from a smaller-scale interval with little variability and high correlation. T_{bk} is the wavelength at which the break occurs, and is inversely related to the wave number (k_{bk}). The effect of increasing T_{bk} (i.e., reducing k_{bk}) is illustrated by identifying the peaks or maxima above a zero threshold (circle markers) in the profiles. As T_{bk} increases, the separations between the peaks increase and many of the features (i.e., *maxima and minima*) in the profiles become less significant. By reducing k_{bk}, the number of low-frequency perturbations within the scale interval characterized by spectral exponent β_1 is reduced, and the scales affected by such perturbations are limited to the larger scales. The increase in the high-frequency interval also increases the range of scales characterized by spectral exponent β_2, associated with a stronger correlation structure. The differences in the scale at which the break occurs observed in the one-dimensional spectra of snow imply significantly larger characteristic scales in the alpine tundra subarea, which is also consistent with the slower decay displayed in the correlation function of the alpine tundra subarea (Figure 3.8b).
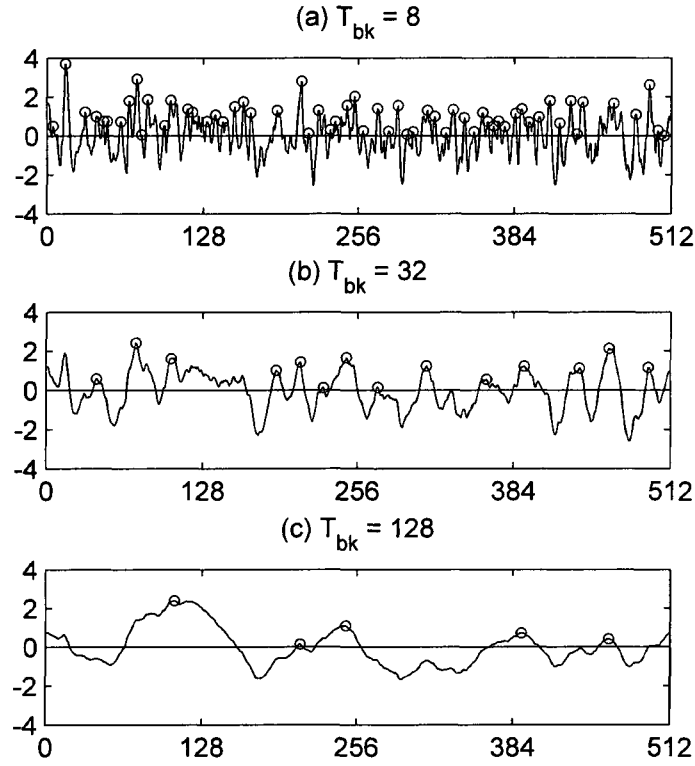
Figure 3.10. Synthetic profiles with a low-frequencies spectral exponent (β_1) of 0.0 and a high-frequencies spectral exponent (β_2) of 3.5. T_{bk} is the wavelength at which the scale break occurs, and is related to the wave number by N/k_{bk}.

Figure 3.11a shows a series of profiles with β_1 varying between 0.0 and 2.0, constant β_2 of 3.5, and constant T_{bk} = 32. The vertical lines in the figure are included as a reference and are spaced at a distance of T_{bk}. Overall, the increase in the low-frequencies spectral exponent affects the features of the larger scales, leading to a stronger persistence in the profiles at scales larger than T_{bk}. The heights of the profile for points separated by distances larger than T_{bk} become more correlated as β_1 increases. The increase in β_1 also affects the variability of the smaller scales although in a less significant way, because the contribution of perturbations in the high-frequency interval is reduced as the power

93

spectrum in the low-frequency interval becomes steeper. The low-frequency spectral exponents of snow depth obtained in both of the subareas indicate a weaker correlation structure for scales larger than the corresponding break in the forested subarea with respect to that in the tundra subarea.
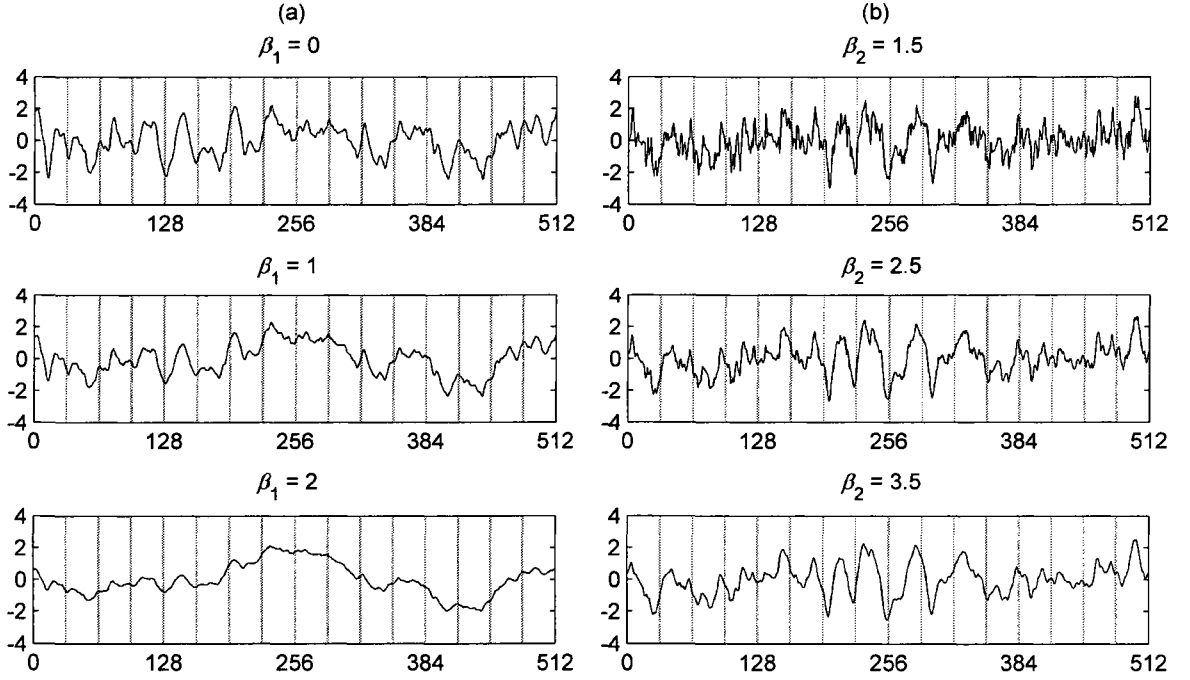
Figure 3.11. Synthetic profiles with (a) low-frequencies spectral exponents (β_1) varying between 0.0 and 2.0, and a constant high-frequencies spectral exponent (β_2) of 3.5, and (b) with a constant low-frequencies spectral exponent (β_1) of 0.0, and high-frequencies spectral exponents (β_2) varying between 1.5 and 3.5. All of the profiles were generated with $T_{bk} = 32$. The grey vertical lines are included as a reference scale and are spaced at a distance of T_{bk}.

Figure 3.11b shows a series of profiles with a constant low-frequency spectral exponent of 0.0, high-frequency spectral exponents varying between 1.5 and 3.5, and constant T_{bk} = 32. As observed, the variability of the profiles for scales smaller than T_{bk} decreases as β_2 increases, while the features at scales larger than T_{bk} are preserved in all of the profiles regardless of the value of β_2. The high-frequency exponent controls the characteristics of the variations for the smaller scales as the exponent controls the contribution of the high-frequency perturbations to the variance. Increasing the exponent implies a faster decay in the contributions, and hence, a smoother profile at scales smaller than T_{bk}. According to these observations and the high-frequency exponent values of snow depth for both subareas, the snow depth profiles in the forested subarea show higher correlation structure for scales smaller than the corresponding breaks.

3.4.4.2 Snow Depth Fields

Four isotropic fields with mean two-dimensional spectral exponents of 1.0 and 4.5 for the low and high frequencies, respectively, and with breaks (T_{bk}) occurring at scales between 16 and 128 are presented in Figure 3.12. The spectral exponents of the fields were selected to differ by one with respect to the exponents used to generate the profiles shown in Figure 3.10. Therefore, a cross section of the fields would exhibit similar spectral characteristics as the profiles in Figure 3.10. In the figure, square boxes of side dimensions equal to the corresponding T_{bk} are shown below each field as reference. Similar to the one-dimensional case, the scale at which the break occurs influences the characteristic scales of the fields, with the main features separated by distances comparable to the corresponding T_{bk}, and a much smoother pattern of variation for the

95

small scales. The case presented is similar to what is observed in the forested environment (Figure 3.3a), where little anisotropy is observed and the spatial organization of the trees strongly influences the spatial characteristics of snow depth at scales of the order of meters to tens of meters. The location of individual trees and canopy characteristics affect the amount of snowfall intercepted, and in consequence, influence the size, depth and location of local minima (i.e., tree wells) in the snow cover. Such control explains the similarities between the scaling characteristics of the snow depth and the vegetation height fields in the forested environment.

(a) $T_{bk} = 16$

(b) $T_{bk} = 32$

-4.0 | | 3.9

-4.1 | | 3.5

(c) $T_{bk} = 64$

(d) $T_{bk} = 128$

-3.8 | | 3.1

-3.6 | | 3.2

0   128   256
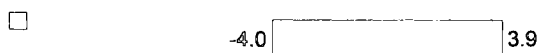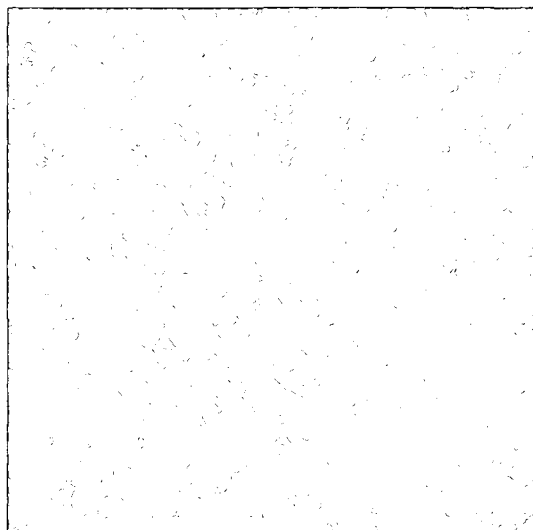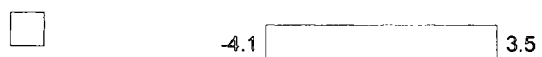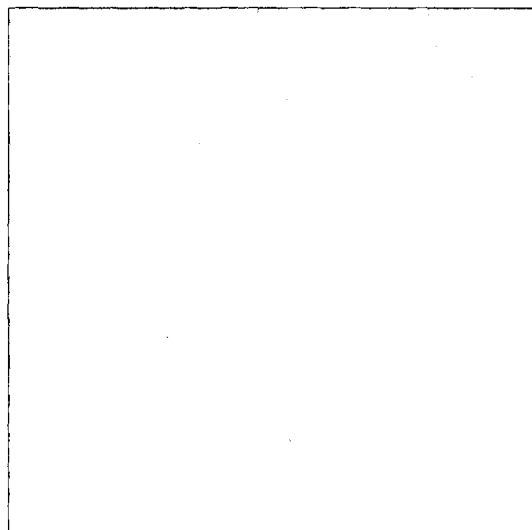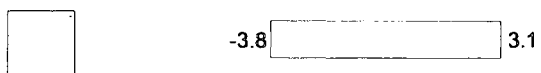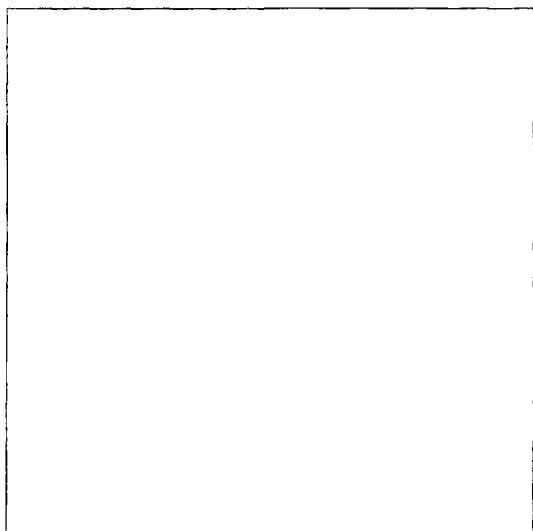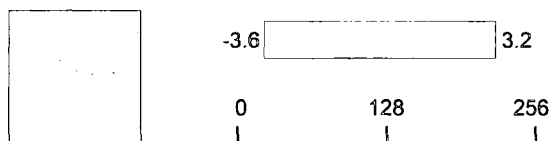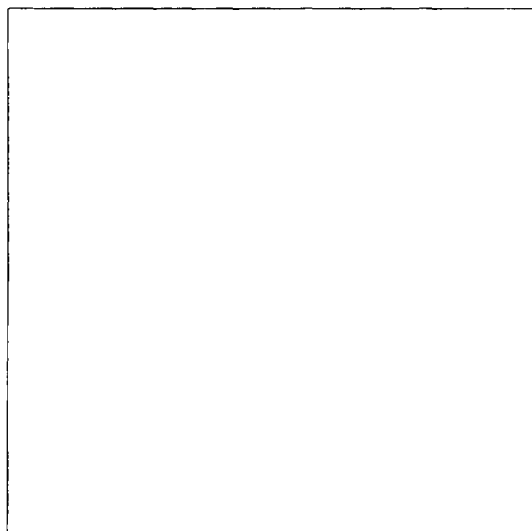
Figure 3.12. Synthetic fields with two-dimensional low- and high- frequency spectral exponents of 1.0 and 4.5, respectively, and T_{bk} between 16 and 128. Black square boxes of side T_{bk} are shown below each of the fields as a reference scale.

97

For the anisotropic case, we explore first the effect of directional dependence of the scale of the break, and second the effect of changes in the low-frequency spectral exponents and the scale of the break simultaneously. These two sub-cases are included to simulate the type of variations in the spectral properties of snow depth observed by *Trujillo et al.* [2007] in wind dominated environments, as well as in the alpine tundra subarea studied here. Our observations indicate that the scale of the break varies from high to low from the predominant wind direction to the perpendicular direction, while the low-frequency exponent varies from low to high from the predominant wind direction to the perpendicular direction.

Figure 3.13 shows two fields of 512 x 512 generated with variations in the scale of the break such that the longer scale break occurs in a predominant direction, and the shorter scale break in a perpendicular direction. The low-frequency and high-frequency one-dimensional spectral exponents were maintained constant for all directions, with β_1 of 0.0 and β_2 of 3.5. The scale break as a function of direction for each of the fields is indicated by the black ellipse shown at the bottom of each field as a reference scale. The predominant direction (longer scale break) of the fields was selected at 40° counter clock-wise (CCW) from the east direction. The field in Figure 3.13a exhibits small-scale variability, with longer separation distances between peaks along the predominant direction (T_{bk} = 64). Along the perpendicular direction (T_{bk} = 16), the variability occurs over smaller scales. In Figure 3.13b, similar characteristics can be observed, however the scale breaks occur at significantly longer spatial scales, with T_{bk} = 128 along the predominant direction, and T_{bk} = 64 along the perpendicular direction. Also, because β_1

98

and β_2 are maintained constant across all directions, the variability of the fields above and below the breaks is similar for all directions, with a weak correlation structure above separations longer than the break, and a strong correlation structure for shorter separations.
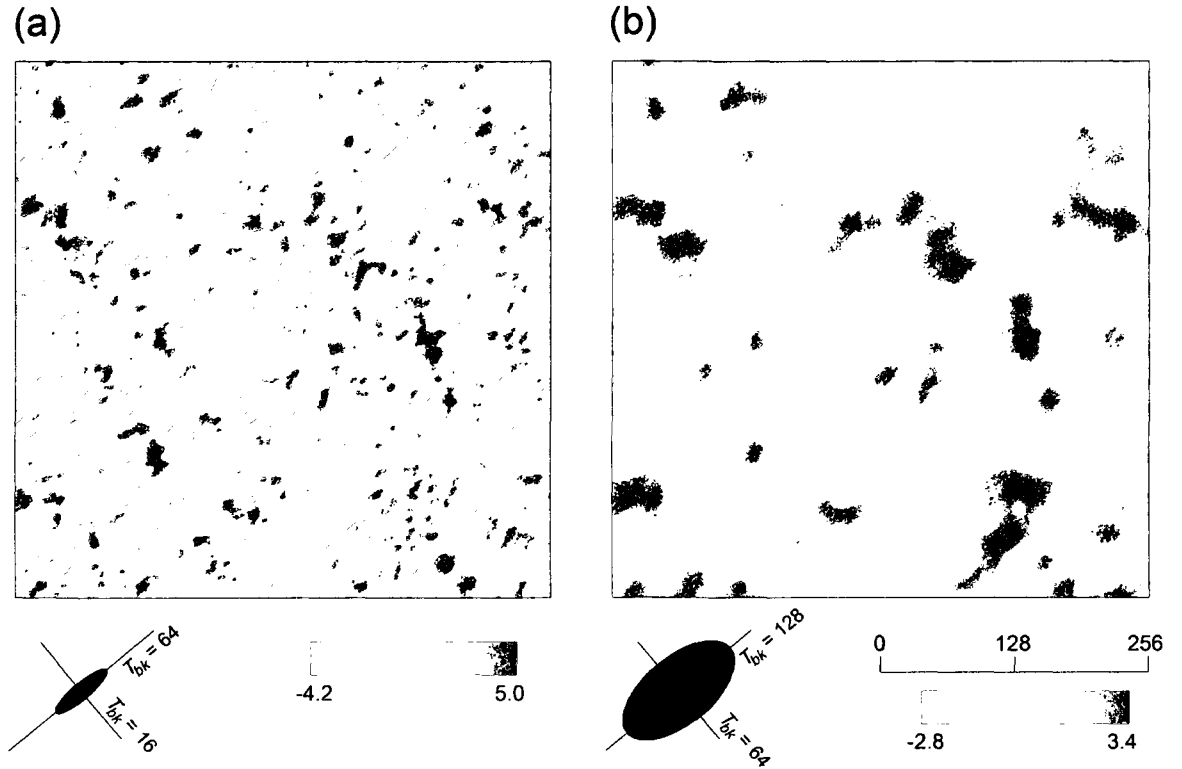
Figure 3.13. Synthetic anisotropic fields generated with uniform one-dimensional low- and high-frequency spectral exponents of 0.0 and 3.5, respectively, for all directions. The directional variations of T_{bk} are included as a reference scale at the bottom of each field, represented by the black ellipse.

Figure 3.14 shows two synthetic fields generated with directional variations not only in the scale of the break, but also in the low-frequency spectral exponents. The high-

frequency spectral exponent was set constant at a value of 2.5 for all directions, similar to the values observed for the snow depth field of the tundra subarea. The field presented in Figure 3.14a was generated with directional variations in β_1 between 0.0 and 0.5, and with variation in T_{bk} between 64 for the predominant direction and 16 in the perpendicular direction. The predominant direction of both fields is oriented at 130° CCW from the east. The directional variations of the scale break are included as a reference scale at the bottom of Figure 3.14a, represented by the black ellipse. The field presented in Figure 3.14b was generated using the same directional variation in T_{bk} as the one used for the field in Figure 3.14a, but with a wider variation in β_1, with values between 0.0 for the predominant direction, and 1.5 and for the perpendicular direction. A summary of the directional variations of β_1 and T_{bk} used to generate the fields is presented in Table 3.3. Because of these variations, the larger scales exhibit a stronger correlation structure (stronger persistence) along the perpendicular direction (40°/220° CCW) with respect to that along the predominant direction (130°/310° CCW), as β_1 goes from 0.5 (Figure 3.14a) or 1.5 (Figure 3.14b) for the perpendicular direction to 0.0 for the predominant direction. These differences imply that for profiles across the predominant direction, points that are separated by distances larger than the corresponding scale break exhibit little or no correlation ($\beta = 0$), while for profiles along the secondary direction, points separated by distances larger than the corresponding break exhibit a degree of correlation than is related to the spectral exponent (0.5 or 1.5). The correlation structure of the larger scales along intermediate directions lies in between these two bounds.

(a) $0.0 \leq \beta_1 \leq 0.5$, $\beta_2 = 2.5$

(b) $0.0 \leq \beta_1 \leq 1.5$, $\beta_2 = 2.5$

-4.9   4.1

0   128   256

-4.5   3.8
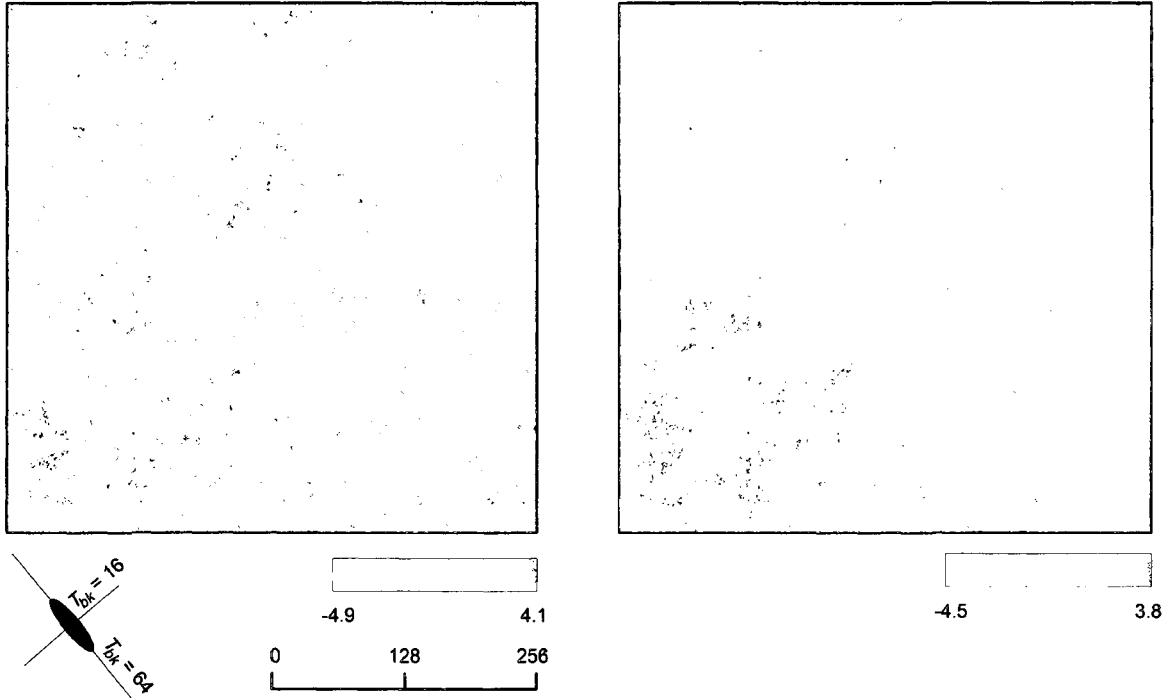
Figure 3.14. Synthetic anisotropic fields generated with directional variations in β_1 between (a) 0.0 and 0.5, and between (b) 0.0 and 1.5. β_2 was set constant at a value of 2.5 for all directions. The directional variations of T_{bk} are included as a reference scale (black ellipse). A summary of the values of β_1, β_2 and T_{bk} used to generate the fields is presented in Table 3.3.

Table 3.3. Summary of the spectral characteristics used to generate the anisotropic fields presented in Figure 3.14. The angle is measured with respect to the east in the CCW direction. The two columns for β_1 refer to the corresponding field in the Figure.

Angle (°)	β_1 (a)	β_1 (b)	β_2	T_{bk}
130	0.00	0.00	2.5	64
175	0.25	0.75	2.5	22
220	0.50	1.50	2.5	16
265	0.25	0.75	2.5	22

The fields in Figure 3.14a and Figure 3.14b were generated using the same parent processes (the original white noise processes of each of the lines are maintained the same for both of the fields), so the features of the fields are similar, although the magnitudes of the variations are different as the spectral exponents are different. Both fields exhibit similar bands of high values and low values, similar to the ones observed in the snow depth field of the alpine environment (Figure 3.3b), in which snow drifts and scour areas are formed along a direction that is perpendicular to the predominant wind directions, and with separations between the snow drifts that are dependent on the location of topographic ridges and depressions. However, higher variability can be observed across the perpendicular direction in the field shown in Figure 3.14a in comparison to the field in Figure 3.14b, caused by the smaller low-frequency spectral exponent (0.5 compared to 1.5).

3.5 Summary

LIDAR snow depths obtained in April 2003 for two adjacent areas of 500 m by 500 m were analyzed to determine scaling characteristics and spatial organization of snow depth in a sub-alpine forest and an alpine tundra environment. Both of the areas present similar topographic characteristics (e.g., slope and aspect), limiting the differences to vegetation characteristics and the influence of wind. The distribution of snow depth in the forested subarea follows a Gaussian distribution, while for the tundra subarea it is negatively skewed. The mean of snow depth increases with elevation in the forest area, while it decreases in the alpine portion. The standard deviation of snow depth in the tundra

subarea is greater by a factor of two compared to that of the forested area. The standard deviation of snow depth is relatively constant with elevation below the tree-line, while above the tree-line in the tundra subarea, it shows an overall increase. The two-dimensional correlations of snow depth indicate little spatial memory and quasi-isotropic conditions in the forested area, while they show a marked directional bias that is consistent with the predominant wind directions and the location of topographic ridges and depressions in the tundra subarea. The spectral density functions of the snow depth fields follow a bilinear behavior with two scale intervals, each characterized by a different spectral exponent. The locations of the scale breaks in the forested area coincide with those of the vegetation height field, while the breaks in the snow depth scaling are displaced towards larger scales in the tundra subarea with respect to those observed in the corresponding vegetation height field.

3.6 Appendix

Spectral generation techniques are useful for the generation of synthetic profiles and fields that exhibit spectral characteristics that are statistically indistinguishable from those observed in the snow depth spectra. Here we introduce modifications of Fourier filtering techniques and of the turning bands method to reproduce the bilinear power-law behavior observed in the profiles and fields of snow depth of the study areas.

3.6.1 Bilinear self-affine profiles

In order to generate traces with bilinear spectral densities, we use a modified version of the standard Fourier filtering method as indicated below. The following nomenclature is used:

k: wave number.

k_{bk}: wave number at which the scale break occurs.

T_{bk}: wave length at which the break occurs, and it is related to the wave number by N/k_{bk}, where N is the number of data points in the profile.

The traces are generated as follows:

i.   A white noise process is generated as a series of uncorrelated Gaussian random values for the desired number of data points (N).

ii. The complex coefficients of the Fourier transform of the series obtained in step (i) are determined.

iii. The complex coefficients of the Fourier transform of the white noise process are multiplied by a factor of $1/k^{\beta_1/2}$ for $k = 1,...,k_{bk}$, and by a factor of

$k_{bk}^{(\beta_2 - \beta_1)/2} / k^{\beta_2/2}$ for $k = k_{bk}+1,..., N/2$. The complex coefficients for the negative wave numbers correspond to the complex conjugate of the coefficients for the positive wave numbers.

iv. An inverse Fourier transform is performed using the coefficients obtained in (iii). The power spectrum of the resulting series will follow a bilinear power law relationship with a scale break at k_{bk}.

Minimum and maximum absolute errors for the low-frequency exponent of the profiles in Figures 3.10 and 3.11 are 0.01 and 0.22, respectively, while the mean absolute error for all the profiles is 0.05. For the high-frequency exponent, the minimum and maximum absolute errors are 0.00 and 0.10, respectively, while the mean absolute error is 0.05.

3.6.2 Bilinear Self-affine fields

3.6.2.1 Case One: Isotropic fields

Similar to the methodology used for generating linear and bilinear profiles, the Fourier filtering technique can be extended in order to generate synthetic isotropic fields, i.e., fields in which all directions in the x-y plane are equivalent, with a bilinear power spectrum with two-dimensional exponents β_1 and β_2.

The fields can be generated as follows:

i. A random white noise field $\sim N (\mu, \sigma)$ is generated for the desired number of data points (N by N).

ii. The complex coefficients of the two-dimensional Fourier transform of the field obtained in (i) are determined.

iii. The complex coefficients of the two-dimensional Fourier transform of the white noise field are multiplied by a factor of $1/k^{\beta_1/2}$ for $k \leq k_{bk}$, and by a factor of $k_{bk}^{(\beta_2 - \beta_1)/2}/k^{\beta_2/2}$ for $k > k_{bk}$, with $k = \left(k_x^2 + k_y^2\right)^{1/2}$.

iv. An inverse Fourier transform is performed using the coefficients obtained in (iii). The mean two-dimensional power spectrum of the resulting series will follow a bilinear power law relationship with a scale break at k_{bk}.

Minimum and maximum absolute errors for the low-frequency exponent of the isotropic fields in Figure 3.12 are 0.07 and 0.13, respectively, while the mean absolute error is 0.10. For the high-frequency exponent, the minimum and maximum absolute errors are 0.00 and 0.03, respectively, while the mean absolute is 0.01.

3.6.2.2 Case Two: Anisotropic fields

Bilinear anisotropic fields were generated using a modification of the turning bands method (TBM) [*Matheron*, 1973; *Mantoglou and Wilson*, 1982]. In two dimensional space, the TBM transforms the simulation of a two-dimensional realization into the sum of a series of one-dimensional realizations. In the isotropic case, the generations of the one-dimensional (line) realizations are performed along several lines in the unit circle, using a unique one-dimensional covariance function (or power spectral density function) that corresponds to a given two-dimensional covariance function. Then, the value of the two-dimensional process is obtained as a weighted sum of the corresponding values of the line processes. For a particular point in the two-dimensional space, the corresponding

one-dimensional values are assigned by orthogonally projecting the points of the line realization, reason for which the method is named 'turning bands', as the projection of the line process appears as a series of bands that rotate according to the direction of each of the lines. Further details of the projection methodology are not included here as such methodology has been extensively described in several related publications [e.g., *Mantoglou and Wilson*, 1982; *Mantoglou*, 1987; *Setas and Rebordão*, 2000]. The method assumes that the field to be simulated is second-order stationary and isotropic, and that at each point the values are normally distributed and have zero mean.

More recent applications of the methodology have been developed for anisotropic covariance functions [e.g., *Mantoglou*, 1987; *Setas and Rebordão*, 2000]. Anisotropy can be simulated by distributing the lines around the unit circle along directions sampled from a non-uniform probability density function. An alternative approach for simulating anisotropy consists of making the spectral density function (or covariance function) of the one-dimensional process dependent on direction. The latter approach is the one implemented in this study, varying the spectral exponents and scale of the breaks as a function of direction. The line processes are generated following the procedure described in section 3.6.1. The methodology is applied uniformly distributing the desired number of lines along the unit circle similar to *Mantoglou and Wilson* [1982] and *Mantoglou* [1987]. In this way, the anisotropy in the spectral characteristics can be provided as an input in which the location of the scale break and the spectral exponents can be specified for each of the lines. The method was applied using the center of the grid as the origin for the generation. To ensure the continuity of the line processes, and as collinear directions have equivalent spectral properties, the dimension of the line processes was selected to be two

times the side dimension of the square grid, and the origin was set to coincide with the midpoint of the line. For example, if the desired grid size is N x N, the dimensions of line processes is $2N$ and the origin is located at point N. These characteristics condition the lower bound for the spacing of the line processes to be $\sqrt{2}/2$ times the spacing of the grid. Such condition ensures that the length of the lines is greater or equal than the length of the diagonal of the grid.

Given the conditions stated above, the methodology can be implemented as follows:

i. Define the size of the grid (N x N), spacing of the grid (Δ_g), spacing of the line process (Δ_l), angular separation between the lines (e.g., degrees), and spectral properties for each of the lines (β_1, β_2 and T_{bk}). Note that defining the angular separation is equivalent to defining the number of lines (L).

ii. A line process is generated for each direction using the corresponding spectral characteristics provided as input. This step is performed using the procedure described in section 3.6.1. k_{bk} can be determined by approximating the result from dividing the total length of the desired profile by T_{bk} to the closest integer.

iii. The value corresponding to each of the points in the grid is obtained as [*Mantoglou and Wilson*, 1982]

$$z_s(\mathbf{x}_N) = \frac{1}{\sqrt{L}} \sum_{i=1}^{L} z_i(\mathbf{x}_N \cdot \mathbf{u}_i) \qquad (3.A1)$$

Where $z_s(\mathbf{x}_N)$ is the realization of the two-dimensional process for the position $\mathbf{x}_N$, $z_i(\mathbf{x}_N \cdot \mathbf{u}_i)$ is the corresponding realization of the one-dimensional process

for line i, and $\mathbf{x}_N \cdot \mathbf{u}_i$ is the projection of the position vector $\mathbf{x}_N$ onto the unit vector $\mathbf{u}_i$ (directional vector for line i). The subscript s indicates 'synthetic'.

Minimum and maximum absolute errors for the low-frequency exponent of the isotropic fields in Figures 3.13 and 3.14 are 0.03 and 0.23, respectively, while the mean absolute error is 0.09. For the high-frequency exponent, the minimum and maximum absolute errors are 0.01 and 0.17, respectively, while the mean absolute is 0.07.

3.7 Acknowledgements

3.8 References

Arnold, N. S., and W. G. Rees (2003), Self-similarity in glacier surface characteristics, *J. Glaciol.*, *49*(167), 547-554.

Benson, C. S. (1982) Reassessment of winter precipitation on Alaska's Arctic slope and measurements on the flux of wind-blown snow'. *Geophysical Institute Report UAG R-288*. Geophysical Institute, University of Alaska, Fairbanks, 26 pp.

Blöschl, G. (1999), Scaling issues in snow hydrology, *Hydrolog. Process.*, *13*, 2149-2175.

Blöschl, G., and R. Kirnbauer (1992), An analysis of snow cover patterns in a small alpine catchment, *Hydrolog. Process.*, *6*, 99-109.

Brown, S. R. (1987), A note on the description of surface roughness using fractal dimension, *Geophys. Res. Lett.*, *14*(11), 1095-1098.

Cline, D., and Cold Land Processes working group (2001), Cold Land Processes field experiment plan, *http://www.nohrsc.nws.gov/~cline/clpx.html*.

Cline, D., S. Yueh, B. Chapman, B. Stankov, A. Gasiewski, D. Masters, K. Elder, R. Kelly, T. H. Painter, S. Miller, S. Katzberg and L. Mahrt (2008), NASA Cold Land Processes Experiment (CLPX 2002-2003): airborne remote sensing, *J. Hydrometeor*, early online release.

Deems, J. S., S. R. Fassnacht, and K. J. Elder (2006), Fractal Distribution of Snow Depth from Lidar Data, *J. Hydrometeor.*, *7*, 285-297.

Elder, K., J. Dozier, and J. Michaelsen (1991), Snow accumulation and distribution in an alpine watershed, *Water Resour. Res.*, *27*, 1541–1552.

Elder, K., J. Michaelsen, and J. Dozier (1995), Small basin modeling of snow water equivalence using binary regression tree methods, *Proc. Symp. on Biogeochemistry of Seasonally Snow-Covered Catchments*, IAHS-AIHS and IUGG XX General Assembly, IAHS Publication 228, pp. 129–139, Boulder, CO.

Elder, K., W. Rosenthal, and R. Davis (1998), Estimating the spatial distribution of snow water equivalence in a montane watershed, *Hydrolog. Process.*, *12*(10-11), 1793-1808.

Erickson, T. A., M. W. Williams, and A. Winstral (2005), Persistence of topographic controls on the spatial distribution of snow in rugged mountain terrain, Colorado, United States, *Water Resour. Res.*, *41*, W04014, doi:10.1029/2003WR002973.

Erxleben, J., K. Elder, and R. Davis (2002), Comparison of spatial interpolation methods for estimating snow distribution in the Colorado Rocky Mountains, *Hydrolog. Process.*, *16*, 3627-3649.

Essery, R., J. Pomeroy, J. Parviainen, and P. Storck (1996), Sublimation of snow from coniferous forests in a climate model, *J. Clim.*, *16*, 1855-1864.

Evans, B. M., D. A. Walker, D. S. Benson, E. A. Nordstrand, and G. W. Petersen (1989), Spatial interrelationships between terrain, snow distribution and vegetation patterns at an artic foothills site in Alaska, *Holarctic. Ecol.*, *12*, 270-278.

Granger, R. J., J. W. Pomeroy, and J. Parviainen (2002), Boundary-layer integration approach to advection of sensible heat to a patchy snow cover, *Hydrolog. Process.*, *16*, 3559-3569.

Greene, E. M., G. E. Liston, and R. A. Pielke Sr. (1999), Relationships between landscape, snow cover depletion, and regional weather and climate, *Hydrolog. Process.*, *13*, 2453-2466.

Hosang, J., and K. Dettwiler (1991), Evaluation of a water equivalent of snow cover map in a small catchment-area using geostatistical approach, *Hydrolog. Process.*, *5*, 283-290.

Huang, J., D. L. Turcotte (1989), Fractal mapping of digitized images: application to the topography of Arizona and comparison with synthetic images *J. Geophys. Res.*, *94*(B6), 7491-7495.

Kang, B., and J. A. Ramírez (2001), Comparative study of the statistical features of random cascade models for spatial rainfall downscaling, *Proc. AGU Hydrology Days 2001*, edited by J. A. Ramírez, pp. 151-164, Hydrology Days Publications, Fort Collins, CO.

Kuchment, L. S., and A. N. Gelfan (2001), Statistical self-similarity of spatial variations of snow cover: verification of the hypothesis and application in the snowmelt runoff generation models, *Hydrolog. Process.*, *15*, 3343-3355.

Li, L., and J. W. Pomeroy (1997), Estimates of threshold wind speeds for snow transport using meteorological data, *J. Appl. Meteorol.*, *36*, 205-213.

Liston, G. E. (1999), Interrelationships among snow distribution, snowmelt, and snow cover depletion: Implications for atmospheric, hydrologic, and ecologic modeling, *J. Appl. Meteorol.*, *38*(10), 1474-1487.

Liston, G.E. (2004), Representing subgrid snow cover heterogeneities in regional and global Models, *J. Clim.*, *17*, 1381–1397.

Liston, G. E., and M. Sturm (1998), A snow-transport model for complex terrain. *J. Glaciol.*, *44*(148), 498-516.

Lovejoy, S, and D. Schertzer (1985), Generalized scale invariance in the atmosphere and fractal models of rain, *Water Resour. Res.*, *21*(8), pp. 1233-1240.

Luce, C. H., D. G. Tarboton, and K. R. Cooley (1998), The influence of the spatial distribution of snow on basin-averaged snowmelt, *Hydrolog. Process.*, *12*, 1671-1683.

Luce, C. H., D. G. Tarboton, and K. R. Cooley (1999), Sub-grid parameterization of snow distribution for an energy and mass balance snow cover model, *Hydrolog. Process.*, *13*, 1921-1933.

Mandelbrot, B. (1967), How long is the coast of Britain? Statistical self-similarity and fractional dimension, *Science*, 156, 636-638.

Mandelbrot, B. (1982), *The Fractal Geometry of Nature*, 468 pp., Freeman, San Francisco.

Mantoglou, A. (1987), Digital simulation of multivariate two- and three-dimensional stochastic processes with a spectral turning bands method, *Math. Geol.*, *19*(2), 129-149.

Mantoglou, A., and J. L. Wilson (1982), The turning bands method for simulation of random fields using line generation by a spectral method, *Water Resour. Res.*, *18*(5), 1379-1394.

Marsan, D., D. Schertzer, and S. Lovejoy (1996), Causal space-time multifractal processes: Predictability and forecasting of rain fields, *J. Geophys. Res.*, *101*(D21), 26333-26346.

Matheron, G. (1973), The intrinsic random function and their applications, *Advan. Appl. Prob.*, *5*, 439-468.

McGinnis, G. L., (2004), Estimating climate-change impacts on Colorado Plateau snowpack using downscaling methods. *Prof. Geogr.*, *45*(1), 117-125, doi: 10.1111/0033-0124.00062.

Meng, H., J. A. Ramírez, J. D. Salas, and L. Ahuja (1996), Scaling analysis of infiltration at R-5 catchment, *Invited Proceedings of the USDA-ARS Workshop on Real World Infiltration*, Pingree Park, CO, July 22-25. CWRRI Information Series No. 86, pp. 239-240.

Miller, S.L. (2003), *CLPX-Airborne: Infrared Orthophotography and LIDAR Topographic Mapping*, National Snow and Ice Data Center. Digital Media, Boulder, CO.

Over, T. M. (1995), Modeling space-time rainfall at the mesoscale using random cascades, Ph.D. thesis, University of Colorado, Boulder.

Over, T. M., and V. K. Gupta (1996), A space-time theory of mesoscale rainfall using random cascades, *J. Geophys. Res.*, *101*(D21), 26319-26332.

Pomeroy, J. W., and D. M. Gray (1995), Snowcover accumulation, relocation and management, NHRI Science Report No. 7, National Hydrology Research Institute, Environment Canada: Saskatoon, SK; 134 pp.

Pomeroy, J. W., J. Parviainen, N. Hedstrom, and D. M. Gray (1998), Coupled modelling of forest snow interception and sublimation, *Hydrolog. Process.*, *12*, 2317-2337.

Rodríguez-Iturbe, I., G. K. Vogel, R. Rigon, D. Entekhabi, F. Castelli, and A. Rinaldo (1995), On the spatial organization of soil moisture fields. *Geophys. Res. Lett.*, *22*(20), 2757-2760.

Setas, M., and J. M. Rebordão (2000), Modeling anisotropy and fractal two-dimensional fields: a tool for image simulation, *Opt. Eng.*, *39*(6), 1497-1506.

Shook, K., and D. M. Gray (1994), Determining the snow water equivalent of shallow prairie snowcovers, paper presented at 51st Eastern Snow Conference, Dearborn, Mich., June 14–16.

Shook, K, and D. M. Gray (1996), Small-scale spatial structure of shallow snowcovers, *Hydrolog. Process.*, *10*, 1283-1292.

Shook, K, and D. M. Gray (1997), Synthesizing shallow seasonal snow covers, *Water Resour. Res.*, *33*(3), 419–426.

Shook, K., D. M. Gray, and J. W. Pomeroy (1993), Temporal variation in snowcover area during melt in Prairie and Alpine environments, *Nord. Hydrol.*, *24*, 183–198.

Tessier, Y., S. Lovejoy, and D. Schertzer (1993), Universal multifractals: Theory and observations for rain and clouds, *J. Appl. Meteorol.*, *32*(2), 223-250.

Trujillo, E., J. A. Ramírez, and K. J. Elder (2007), Topographic, meteorologic, and canopy controls on the scaling characteristics of the spatial distribution of snow depth fields, *Water Resour. Res.*, *43*, W07409, doi:10.1029/2006WR005317.

Turcotte, D. L. (1987), A fractal interpretation of topography and geoid spectra on the earth, moon, venus, and mars, *J. Geophys. Res.*, *92*(B4), E597-E601.

Turcotte, D. L. (1989), Fractals in geology and geophysics, *Pure Appl. Geophys.*, *131*(1), 171-196.

Voss, R. F. (1985), Random fractal forgeries, in *Fundamental Algorithms for Computer Graphics*, NATO ASI Series, Vol. F17, edited by R. A. Earnshaw, pp. 805-835, Springer-Verlag, Berlin Heidelberg.

Weitzenkamp, B., T. Sauter, A. Kraemer, R. Roth, and C. Schneider (2008), Spatial downscaling of snow cover as a tool for projections of snow availability for winter sports in 2030 in the Black Forest using Remote Sensing and GIS Methods, *Geophys. Res. Abstr.*, *10*, EGU2008-A-06206.

Winstral, A., K. Elder, and R. Davis (2002), Spatial snow modeling of wind-redistributed snow using terrain-based parameters, *J. Hydrometeor.*, *3*, 524-538.

Xu, H., J. O. Bailey, E. C. Barrett, R. E. J. Kelly (1993), Monitoring snow area and depth with integration of remote sensing and GIS, *Int. J. Rem. Sens.*, *14*(17), 3259 – 3268.

4 Cellular Automata Model for Simulating Wind Transport of Snow and the Interaction with Topography and Alpine Vegetation

4.1 Abstract

A cellular automata model is developed for simulating the evolution of snow packs in areas in which wind transport of snow and its interactions with terrain and short alpine vegetation are dominant. The model simulates the horizontal transport and deposition of snow from a layered snowpack formed by accumulated weekly precipitation, a physically based densification process that accounts for the compaction of the snow layers, and the interaction between the blowing snow with small-scale topographic features and vegetation. Other features include simulation of time-variable transport trajectories, space- and time-variable precipitation, and time-variable initial density. The erosion and deposition of particles is determined according to a predefined set of probabilities dependent upon the location of the grid cells relative to aerodynamic obstacles and the vertical angles with such obstacles. The interaction with the vegetation is simulated using a set of probabilities that depend on the height of the vegetation, and a relationship that relates the exposed vegetation height to the capacity of the vegetation to reduce snow removal and enhance deposition. The model is applied to combinations of synthetic topographic fields, vegetation patterns, and atmospheric conditions. The results show that the statistical properties of snow depth fields throughout the accumulation period in wind dominated environments depend on the transport volumes of snow, which are dependent on meteorological conditions (e.g., winds and temperature). The inter-seasonal

consistency of the spatial organization of snow covers in wind-dominated environments documented in several studies is conditioned to the consistency of wind patterns and wind transport potential. Years with differences in wind regimes and meteorological conditions (e.g., wind speeds and directions, temperatures) will exhibit differences in the spatial statistical properties of snow cover properties (e.g., depth and SWE). The magnitudes of the differences in the spatial statistical properties depend on the magnitudes of the differences in the meteorological conditions.

4.2 Introduction

The interactions between the snow cover, topography, vegetation, and winds greatly control the spatial organization of snow cover properties in wind dominated environments [*Hiemstra et al.*, 2002; *Trujillo et al.*, 2007; 2009]. Such interactions determine the size and location of scour and accumulation areas, volumes of snow transport, distances over which the snow is transported, and sublimation losses, among others. Better understanding of these interactions and their effect in the spatial organization and the time evolution of snow covers in wind dominated environments allows for improvements in snowmelt modeling [e.g., *Luce et al.*, 1998; *Greene et al.*, 1999; *Liston*, 1999], interpolation of point measurements [e.g., *Elder et al.*, 1998; *Erxleben et al.*, 2002; *Erickson et al.*, 2005], downscaling of remote sensing data and model results [e.g., *McGinnis*, 1997; *Weitzenkamp et al.*, 2008], subgrid scale parameterizations [e.g., *Luce et al.*, 1999; *Liston*, 2004], and design strategies for measuring and monitoring snow properties [e.g., *Xu et al.*, 1993].

The spatial organization of snow covers has been studied through the analysis of ground measurements [e.g., *Evans et al.*, 1989; *Elder et al.*, 1991; *Shook and Gray*, 1996; 1997; *Kuchment and Gelfan*, 2001; *Erickson et al.*, 2005], remote sensing measurements [e.g., *Frezzotti et al.*, 2002; *Deems et al.*, 2006; *Trujillo et al.*, 2007; 2009], and results from snow models [e.g., *Liston and Sturm*, 1998; *Liston et al.*, 1999; *Liston et al.*, 2008]. The analyses of such datasets are limited by the spacing, extent and time continuity of the measurements, and by the spatial resolution and accuracy of the models. Some of the

most recent studies have focused on the analysis of snow depths close to maximum accumulation for scales between 1 m and 1 km using high resolution Light Detection and Ranging (LIDAR) data from the Colorado Rocky Mountains [*Deems et al.*, 2006; *Trujillo et al.*, 2007; 2009]. *Trujillo et al.* [2007; 2009] demonstrated that in wind dominated environments, the interactions between snow, winds, topography, and vegetation control the scaling properties and the spatial organization of the snow depth fields. However, these analyses only provide information for one date in the season, and the time evolution of the snow cover and the time variations in the characteristics of the spatial organization still need to be resolved. In this study, we address this problem by introducing a cellular automata model for the representation of snow covers in wind dominated environments, with components that allow for the simulation of the interactions between snow and topography, vegetation and wind patterns. Several hypothetical scenarios are simulated to analyze the response of the system to variations in precipitation, topography, and winds, providing physically based evidence for the characteristics of the spatial organization of snow depth in such environments, and also extending the analyses to other times in the season. The scales at which the model works are compatible with the available high resolution LIDAR measurements of snow depth analyzed in previous studies, facilitating comparison of the model results with real observations.

4.3 Model Description

A cellular automata model is a discrete representation of a real system consisting of a regular lattice in which the behavior of the system is modeled by defining a set of simplified rules for the local interaction between one cell and its neighboring cells. In the

model, each cell is assigned a discrete state that represents a variable specific to the system (e.g., 0 or 1, a color, or a finite integer). Time is generally discrete, and the state of a cell at a time t is a function of the state of the current and neighboring cells at time $t-1$. The location of each cell is specified by its Cartesian coordinates with respect to an arbitrary origin and set of axes. Cellular automata models have been developed for multiple applications in disciplines ranging from physics and biology to social sciences because of their capability of reproducing complex behavior based on a simple set of rules governing local interactions, which facilitates their computer implementation [e.g., *Wolfram*, 2002].

Cellular automata applications specific to snow sciences include the simulation of crystal growth [*Gravner and Griffeath*, 2006; *Ning and Reiter*, 2007], snow avalanches [*Kronholm and Birkeland*, 2005; *Barpi et al.*, 2007], and snow transport by wind [*Masselot and Chopard*, 1998; *Chopard and Masselot*, 1999]. In the latter studies, snow transport is simulated using a lattice-gas model in which a module that reproduces the wind dynamics is coupled with a snow-particle transport module to reproduce the behavior of the system at the microscopic and macroscopic levels. In this representation, the Navier-Stokes equation is reproduced, allowing for a realistic physical representation of the transport process. However, this type of model requires massive parallel computing and is not suitable for the 1-m scales of interest here as the model works at the particle scale (i.e., snow grains).

The cellular automata model introduced here is designed to work at spatial scales of the order of 1 m and over weekly time steps. The snow pack is represented as a field of slabs in a rectangular lattice with periodic boundary conditions. That is, the state of the

120

system $f(\cdot)$ is such that $f(x+X, y+Y) = f(x, y)$, where X and Y are the periods in the x and y directions, respectively. Therefore, a slab transported outside of the boundary is brought back into the domain in the corresponding position of the opposite boundary. A maximum angle of repose is enforced to simulate the natural stabilization of the slopes. The erosion and deposition of slabs is determined according to a predefined set of probabilities dependent upon the relative location of the grid cells to aerodynamic obstacles and the vertical angles with such obstacles. The interaction with the vegetation is simulated using a set of probabilities that depend on the height of the vegetation, and a relationship between the exposed vegetation height and the capacity of the vegetation to reduce snow removal and enhance deposition. The snowpack is formed by accumulating weekly layers of precipitation that are subjected to wind redistribution. Following the redistribution, a physically based densification scheme that accounts for the compaction of the snow layers is applied to each layer allowing the representation of the variations in snow density through time. Other features include the simulation of time-variable transport trajectories, space- and time-variable precipitation, and time-variable initial density. This model is an extension of the cellular automata model for sand transport originally presented by *Werner* [1995], developed to simulate the three-dimensional formation and evolution of sand dunes in environments in which wind redistribution is dominant. Each element of the model is described below.

4.3.1 Simulation Domain

The simulation domain consists of a rectangular lattice in which the snow surface is represented by a stack of slabs of vertical dimension h at each location $<x, y>$, and

isotropic spacing in the x- and y- directions of ΔL. The slabs lay on top of a non-erodible and spatially variable solid surface, therefore allowing for heterogeneous topography such that the interaction of the snow with different physiographic scenarios can be simulated.

4.3.2 Slab Transport

The processes of erosion, transport, and deposition of snow by wind are influenced by factors such as snow conditions (e.g., cohesion), wind speed and direction, and the interaction of winds and blowing particles with obstacles such as topographic ridges and vegetation. No transport occurs at low wind speeds, but when the speed exceeds a given threshold, some particles begin to be removed and transported in the downwind direction until the speed is reduced such that no further transport can be sustained [*Kind*, 1990]. Higher wind speeds are associated with higher transport volumes over longer distances. These processes are simulated here by using a series of probabilities of removal and deposition, and transport trajectories. The theoretical framework of this representation is described below and additional improvements to this representation are incorporated in Section 4.4.

The transport process starts with the random selection of a location, $<x_{ini}, y_{ini}>$, in the grid as an erosion site, dependent upon the existence of snow slabs at such location. If at least one snow slab exists, the top slab is removed with a probability, $p_{erosion}$, and transported in the downwind direction according to a transport trajectory vector, $L1$, with

---

1 Symbols in bold face represent vectors

components in the x and y directions. At the arrival site, $< x_{ini} + L_x$, $y_{ini} + L_y >$, deposition is determined according to a probability, $p_{deposition}$, that is dependent on the conditions of the arrival grid cell. If the slab is determined to be deposited, the slab count at the deposition grid-cell is increased by one. If the slab is not deposited, a new arrival grid-cell is determined in a similar manner using the last location as the initial and a deposition evaluation is performed for the new arrival location. This process is repeated until the slab is deposited. Descriptions of how $p_{erosion}$ and $p_{deposition}$ are determined are presented throughout the document, with improvements in their physical representation in Section 4.4.

The probabilities of erosion and deposition are dependent on three factors: the location of shadow zones, the presence of snow on top of the solid layer, and the height of the vegetation exposed above the snow pack. These factors are dynamic, as they are affected by the snow depth surrounding a given location. A shadow zone is the area downwind of an aerodynamic obstacle, such that the wind velocity is reduced enough to suppress any further transport or removal. A shadow zone is the area on the downwind side of the crests of the surface of topography + snow located underneath an angle of β (the shadow zone angle) with a horizontal line starting at the crests (Figure 4.1). In such sheltered areas, $p_{erosion}$ takes a value of zero and $p_{deposition}$ takes a value of one, implying that no slab can be removed by wind from a shadow zone and any slab arriving to a cell in shadow zone will be deposited. The second factor is the existence of snow on top of the underlying solid layer, as the probability of deposition at a site with no slabs, $p_{deposition-ns}$, is less than the probability of deposition at a site with at least one snow slab, $p_{deposition-s}$, following the argument that there is a greater likelihood for saltating grains to rebound

from a solid surface than from a softer surface. The effect of the vegetation on the erosion and deposition probabilities is described in the Section 4.3.3 below.
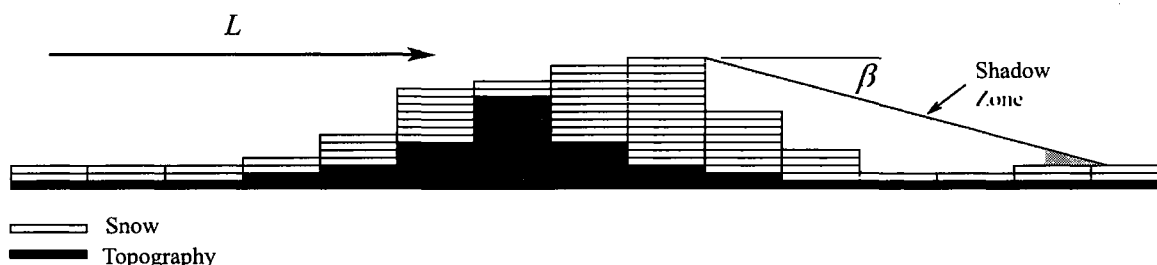
Figure 4.1. Shadow zone determination using the relief formed by the integration of topography and snow.

Sliding of slabs occurs whenever the angle of repose exceeds a maximum angle of repose α. For the erosion case, if α is exceeded after the slab is removed, a slab is transported downslope from the cell with the steepest slope. The process is repeated for the cell source of the transported slab until a cell is reached in which the maximum angle of repose is not exceeded. For the case of deposition, once the slab is determined to be deposited, if the maximum angle of repose is exceeded, the deposited slab is transported down the steepest slope until it reaches a stable position. This process is not conditioned by the wind direction, and depends solely on the direction of the gradient of the surface of topography + snow.

4.3.3 Vegetation Representation

In alpine tundra environments, the interactions between snow, vegetation, winds, and topography exhibit feedbacks that strongly influence the spatial distribution of the snow

and the location of several vegetation species. Alpine plant species have optimal ranges of snow depth that favor seeding and growth of each species [*Komárková*, 1979; *Burns and Tokin*, 1982]. For example, *Walker et al.* [2001] present a plant association chart in which favorable locations for several alpine tundra species are identified on the basis of wind exposure, snow depth ranges and snow-free days, illustrating the complex interactions between all of these influencing factors. These vegetation patterns have feedbacks on the spatial organization of the snow surface because, until fully covered by the snow, vegetation enhances snow deposition and reduces snow removal from the areas in which such vegetation is located as a consequence of the reduction in wind speeds. However, the impact of these feedbacks is limited by the scarcity and low height of alpine plant species, which in turn limits the impacts to the beginning of the accumulation period before they get fully covered and the ablation period when they become exposed. The framework for the representation of these interactions is presented below.

The effect of alpine tundra vegetation is simulated by defining a 'vegetation effectiveness' that affects the probabilities of erosion and deposition from locations in which vegetation is present. To do so, a two-dimensional 'vegetation effectiveness' field with values that can vary between 0 and 1, similar to a frontal area index, is defined according to the location and height of the vegetation. A vegetation effectiveness of 0 corresponds to an erosion probability of 1, and has no effect on the deposition probabilities. A vegetation effectiveness of 1 corresponds to a deposition probability of 1 and an erosion probability of zero. Intermediate values affect the probabilities of erosion and deposition linearly as:

$$p_{erosion} = 1 - v_{effect}$$
$$p_{deposition} = p + v_{effect}(1 - p) \tag{4.1}$$

where v_{effect} stands for vegetation effectiveness, and p can take the values of $p_{deposition-s}$ or $p_{deposition-ns}$, such that the vegetation effectiveness can increase the probability of deposition from either of the starting values. The erosion-deposition effectiveness of the vegetation is not constant but increases (linearly in our model) with the exposed vegetation height so that the burial of the alpine vegetation can be simulated. The vegetation effectiveness at a particular time, t, is calculated for every source and arrival cells according to the following relationship:

$$v_{effect}(x,y,t) = v_{effect}(x,y,0)\left(1 - \frac{SD(x,y,t)}{v_{height}(x,y)}\right) \quad \text{for} \quad SD(x,y,t) \le v_{height}(x,y) \tag{4.2}$$

$$v_{effect}(x,y,t) = 0 \quad \text{for} \quad SD(x,y,t) > v_{height}(x,y)$$

where $v_{height}(x,y)$ is the vegetation height above the ground, $SD(x,y,t)$ is the snow depth above the ground, and $v_{effect}(x,y,0)$ is the initial vegetation effectiveness.

A flow diagram of the transport of one slab accounting for all of the factors described above is presented in Figure 4.2.
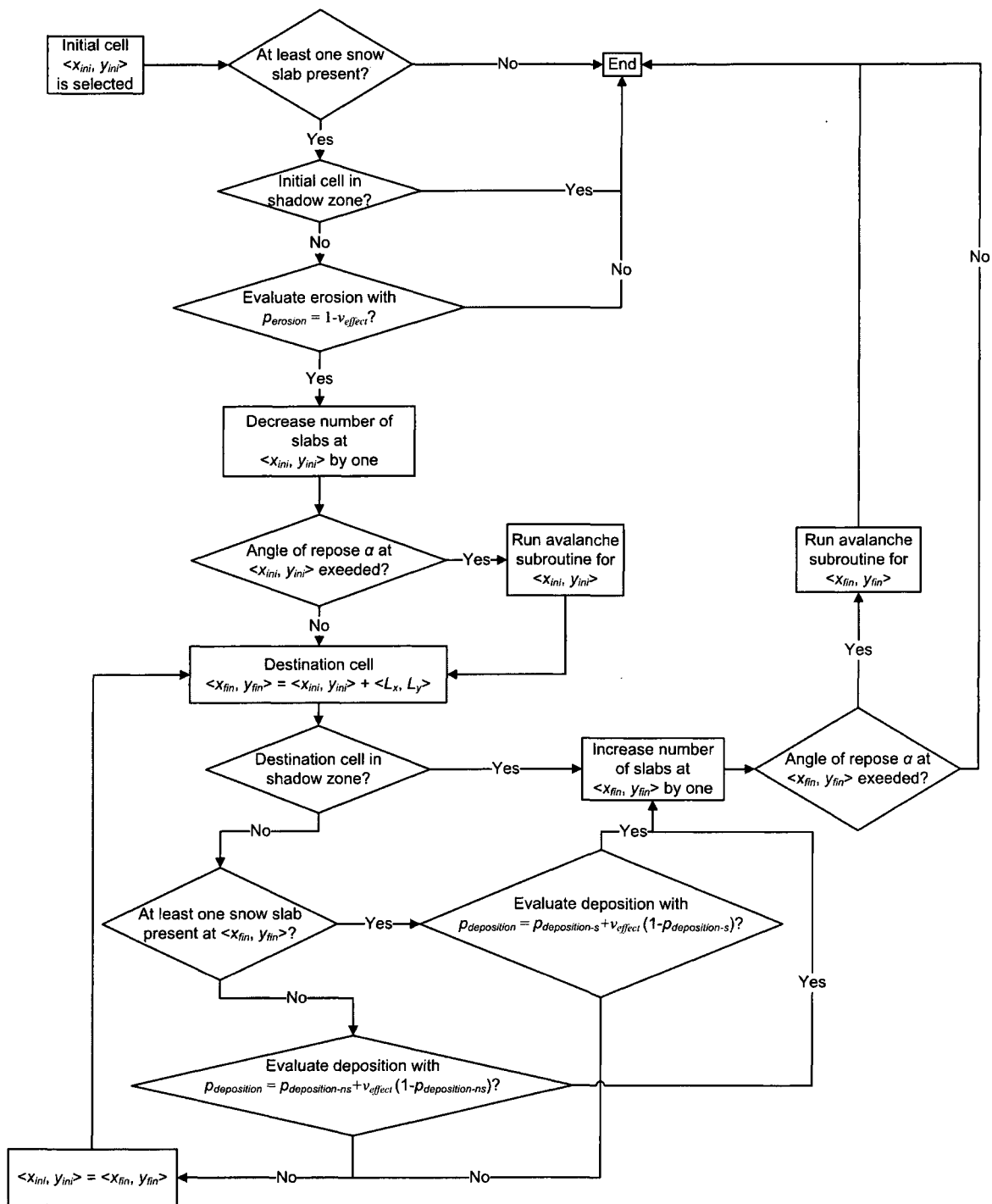
Figure 4.2. Flow diagram of the slab transport routine.

4.3.4   Time Evolution and Winds

In the model, a time step is defined in terms of the number of transported slabs. Simulated time intervals can be related to actual time intervals by selecting the horizontal and vertical dimensions of the slabs to correspond to a given volume of transport similar to real transport rates, and in the case of snow, to the snow available for transport, which in this case, will be related to the volume of fresh snow precipitated during each time interval. To implement this, the horizontal grid size (ΔL) is selected to be 1 m, while the vertical slab size (h) is selected to be 0.1 m. These dimensions would allow for a comparison of the characteristics of the spatial distribution and organization of the simulated fields with high-resolution (~1 m) spatial measurements analyzed in previous studies [e.g., *Trujillo et al.*, 2007; 2008]. Realistic mass transport rates can be simulated by selecting an appropriate time interval, i.e., number of slabs to be transported.

For the case of snow, we have chosen weekly time intervals during which new snow is precipitated into the system, and an interval of a week is defined in terms of the fraction of newly precipitated slabs to be transported. This fraction will be referred to as '*precipitation step*' hereinafter. By using weekly intervals, the snowpack can be simulated as a layered system in which a new input is incorporated at the beginning of every time step. Also, this time step definition allows the model to simulate different levels of transport by simply changing the percentage of fresh snow to be transported during each interval. For example, if a total of 100 slabs are deposited at the beginning of a weekly interval and the time step is chosen to be 50% of the new precipitation, 50 slabs will be transported during that interval following the algorithm described in Section 4.3.2. The other consideration here is that only new snow is to be transported during each

128

interval as the top layer of fresh snow is more likely to be transported as a consequence of the higher exposure to atmospheric conditions and lower densities in comparison to those of older snow. Another advantage of this time step definition is that dynamic wind trajectories can be simulated by simply defining time-dependent vectors, such that the effect of variable trajectories on the organization of snow depth can be analyzed.

4.3.5 Precipitation and Densification of Snow

The snowpack is formed by the accumulation of several layers of snow that are deposited by precipitation at different times and that exhibit different snow characteristics (e.g., snow density). In the model, weekly, spatially-distributed precipitation fields covering the modeling domain are added at the beginning of each time step. Newly precipitated snow constitutes the topmost layer of the snowpack and modifies the number of slabs at each position in the lattice. For the spatially uniform case, a precipitation time series is provided as an input in terms of snow water equivalent (SWE), and is transformed to a depth of snow by using a density of new snow that can be either constant throughout the simulation, or time dependent to represent variations caused by changes in temperature and other factors. The snow depth values are transformed to the number of slabs using the desired value of h, and these amounts are assigned to the precipitation fields that correspond to the time steps. For the spatially variable case, the same procedure is followed, although the transformation from SWE to snow depth is performed for each of the grid-cells. However, in this case, the model assumes a spatially uniform density of fresh snow, so the spatial differences in the number of slabs added are only a consequence of the spatial differences in SWE.

Even in the absence of erosion and deposition, a key process in the evolution of the snowpack is densification. In wind-dominated environments, the density and other physical characteristics of new snow (i.e., snow flakes formed by intermingled snow crystals) is affected by the impacts between the suspended snow flakes and the snow surface, as reported from field observations and experimental wind tunnel studies. *Izumi* [1984] reported that daily new snow density tends to increase with wind speeds within 3 m/s to 9 m/s, while *Kajikawa* [1989] reported that new snow density increased slightly with wind speeds of up to 5 m/s. *Sato et al.* [2008] adjudicate this dependence of the increase in new snow density on wind speed to the degree of snow flake fracture induced by the collisions enhanced by higher wind speeds, which in consequence, enhances the packing of snow crystals. Snow density is also affected by compaction and the rearranging of snow grains, and by metamorphism of snow crystals. *Arnaud et al.* [2000] state that the rearranging of unbounded grains dominates the densification of porous snow, while *Kojima* [1975] argues that the compression of a snow layer due to a snow load is the major cause of the natural densification of a snow pack. All of these processes play a role in the densification of snow in wind dominated environments, however, a comprehensive model for snow densification that accounts for all of them would require large amounts of input data, and its implementation in a cellular automata model as the one proposed here would be impractical. Consequently, densification of snow is simulated in the model using the representation proposed by *Kojima* [1957, 1967], who studied the process using a viscous compression theory. The advantage of this representation is that it requires input data that is available in our cellular automata model, and it allows for a physically based representation of the process of compaction of

the snow by its own weight, which has been identified as one of the main driving forces in the densification process, as illustrated in the quoted studies.

In his studies, *Kojima* found an empirical relationship between a compactive viscosity factor, η, and snow density, ρ, given by:

$$\eta(\rho) = \eta' \exp(K\rho) \qquad (4.3)$$

where K was found to take a value of 21.0×10^{-3} m^3/kg for dry compact snow layers and η' was found to be in a range between 6 kg d/m^2 and 16 kg d/m^2 [*Kojima*, 1957]. This relationship is then combined with the strain rate-stress relationship in (4.4):

$$\frac{1}{\rho}\frac{d\rho}{dt} = \frac{W(t)}{\eta} \qquad (4.4)$$

where $W(t)$ is the overburden load exerted on a particular snow layer. Substituting (4.3) into (4.4), rearranging and integrating, the following expression is obtained:

$$\eta' \int_{\rho(t=0)}^{\rho(t=t)} \frac{\exp(K\rho)}{\rho} d\rho = \int_0^t W(t)dt \qquad (4.5)$$

By solving the expression through substitution, we obtain:

$$\eta'\left[E_1(-K\rho_o) - E_1(-K\rho)\right] = \int_0^t W(t)dt \qquad (4.6)$$

Where ρ_o is the initial density of the layer (i.e., at time of deposition), ρ is the density at time t after deposition, and $E_1(-K\rho_o)$ is the exponential integral, defined as:

$$E_1(x) = \int_x^\infty \frac{\exp(-t)}{t} dt \qquad (4.7)$$

For an alternative development, refer to *Kojima* [1967] and *Motoyama* [1990]. In Figure 4.3, plots of the time-integrated load versus snow density are used to illustrate the

sensitivity of (4.6) to η' and ρ_o. Figure 4.3a, b and c illustrate that the effect of the initial density on the relationship is lost for density values greater than about 250 kg/m^3, regardless of the value of η'. On the other hand, for a given value of the time-integrated load, greater snow densities are obtained for lower η' values. These relationships are used in the model to determine the snow density corresponding to a particular layer at each time step and at each location. The procedure consists of calculating at all locations the time-integrated load for each layer at time t. The overburden load is obtained by summing the weight of the overburden layers plus half of the weight of the layer of interest. The corresponding snow density is obtained from (4.6) using the time-integrated load. Once the new snow density values are estimated, the redistributed SWE values for the layers are divided by the corresponding densities to obtain the snow depth of each layer at each location, and subsequently, the corresponding snow slabs field is obtained maintaining the original value of h. Consequently, throughout a simulation, the volume of a slab is maintained constant, but the weight and SWE contained in a slab is dynamic.
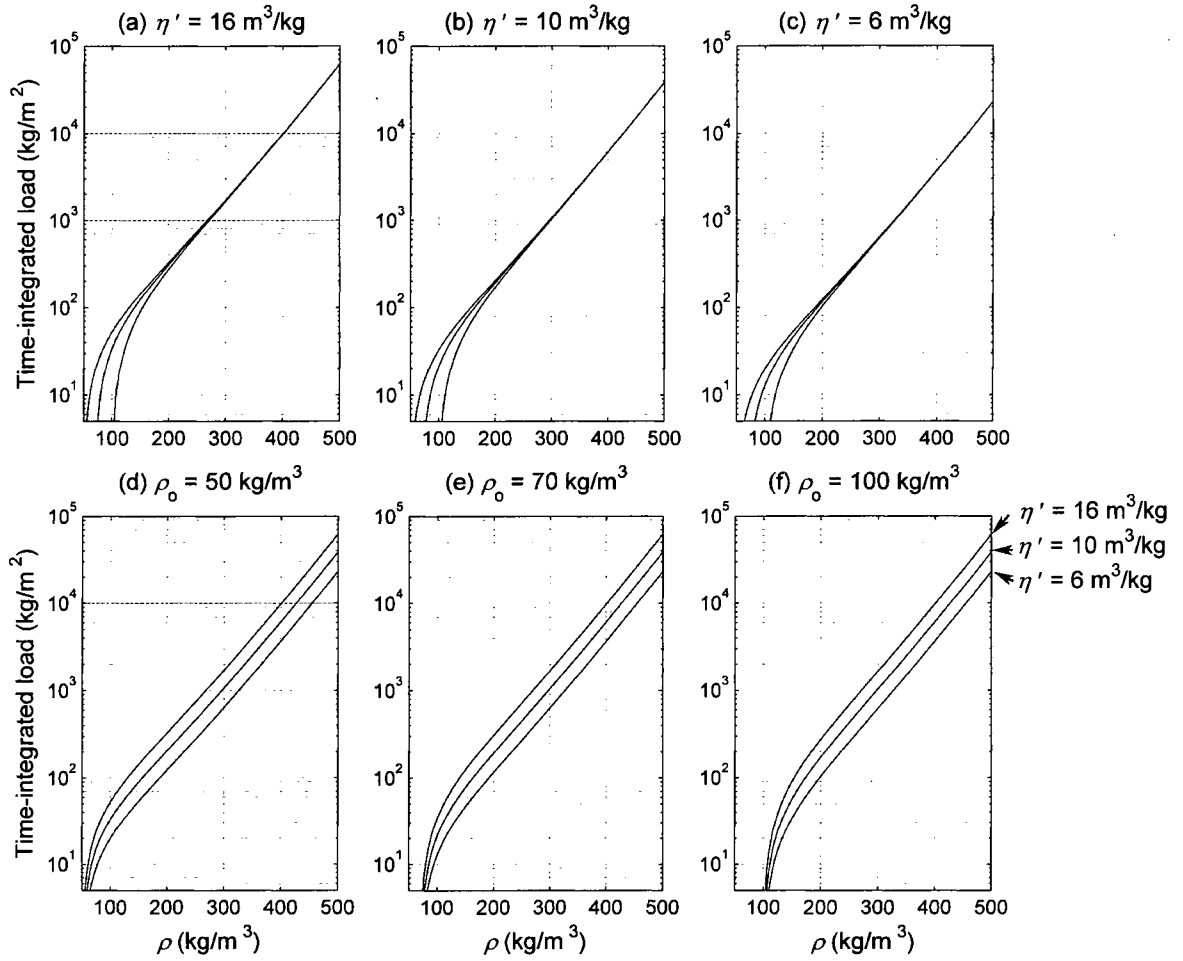
Figure 4.3. Sensitivity of the relationship between the time-integrated overburden load and snow density to η' and ρ_o. (a), (b) and (c) illustrate the differences when using initial snow densities of 50 kg/m^3, 70 kg/m^3 and 100 kg/m^3, but maintaining fixed η' values. (d), (e) and (f) illustrate the differences when using η' values of 6 m^3/kg, 10 m^3/kg and 16 m^3/kg, but maintaining fixed initial density values.

4.4 Model Results and Discussion

The following simulations have the objective of demonstrating the effect that the characteristics of the underlying topography, vegetation, and influencing meteorological factors such as precipitation and winds have in the spatial heterogeneity of snow cover properties (e.g., depth and densities). Several simulations are presented with variations in total transport volumes, synthetic topography and vegetation, time-variable wind trajectories (e.g., magnitude and direction), and time-variable precipitation and initial snow density, illustrating the response of the system to changes in these influencing factors. These results are also used to demonstrate the evolution of the snow cover throughout the accumulations season, broadening the time coverage of previous studies of the spatial heterogeneity of snow cover properties. In all of these simulations, the angle of repose, α, is chosen to be 40° as a representative maximum slope. The shadow zone angle, β, is set to 15°, the probability of deposition when no snow slabs are present, $p_{deposition-ns}$, is set to 0.4, while 0.6 when slabs are present ($p_{deposition-s}$), representing a lower likelihood for saltating grains to be deposited on a solid surface than on a softer surface.

4.4.1 Sinusoidal Topography

The first series of simulations uses a simple representation of topography following a sinusoidal shape with four cycles in a square domain of 64 m (Figure 4.4). This representation is equivalent to a one-dimensional case, as the transport vector, L, is set to have only one component in the x-direction, perpendicular to the crests of the sinusoidal topography. All of the models are run for a total simulation period of 16 weeks, representing a period between the first snow depositions on November, and March, when

redistribution of snow by wind generally starts decreasing due to increases in temperatures, solar radiation, new snow density, and cohesion.
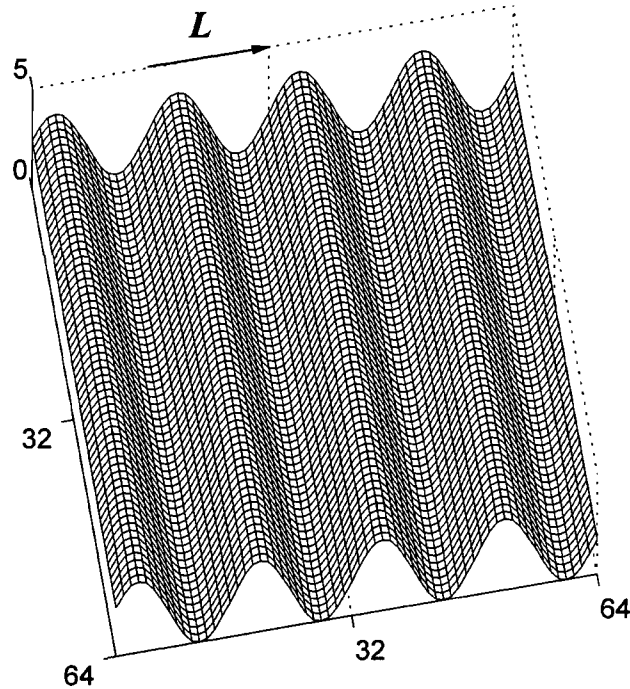
Figure 4.4. Sinusoidal topography and transport trajectory, L, used in the first set of simulations.

Results from two model runs with weekly precipitation of 50 mm (5 slabs with ρ_o =100 kg/m³) distributed uniformly within the model domain are presented in Figure 4.5. The profiles in Figure 4.5a and b were generated applying the densification methodology, while the profiles in Figure 4.5c and d were generated without densification, maintaining the initial density throughout the simulation. L was set to 2 m in the x direction, and the fraction of weekly precipitation transported in each iteration (precipitation step) is set to one. These simulations are used to illustrate the interaction between the snow and the

135

underlying topography, and the effect of the densification model in the results. The results in Figure 4.5a and b show high accumulation of snow on the lee side of the topography, with source areas on the upwind side. The evolution of the snow cover is determined by the interaction of the 'blowing' slabs and the integrated surface of topography + snow depth, which is constantly changing due to the redistribution of slabs and the densification of the snow. The snow depth profiles (Figure 4.5b) exhibit a similar sinusoidal shape, although displaced to the right by a distance close to 8 m, as the peaks in the snow profiles coincide with the depressions in the topography. Very different results are obtained when no densification is allowed (Figure 4.5c and d). At the end of the fourth week, a marked peak in the snow surface is formed behind every ridge. These peaks then lead to the formation of new pronounced peaks on the downwind side by the end of the subsequent four weeks. This process is repeated for the subsequent periods. The results can be interpreted as a displacement of the existing peaks in the downwind direction, accounting of course for the buildup of the newly deposited slabs, as indicated by the arrow in Figure 4.5c. When no densification is simulated, the behavior is very similar to the behavior of sand environments in which downwind migration of sand dunes occurs [e.g., *Havholm and Kocurek*, 1988; *Momiji et al.*, 2000]. A similar migration of the peak is observed in Figure 4.5a, although the time and spatial scales over which the migration occurs are drastically different from the case with no densification. The representation of snow densification is paramount to appropriately simulate the evolution of the snow pack during the accumulation period in environments with significant wind redistribution.
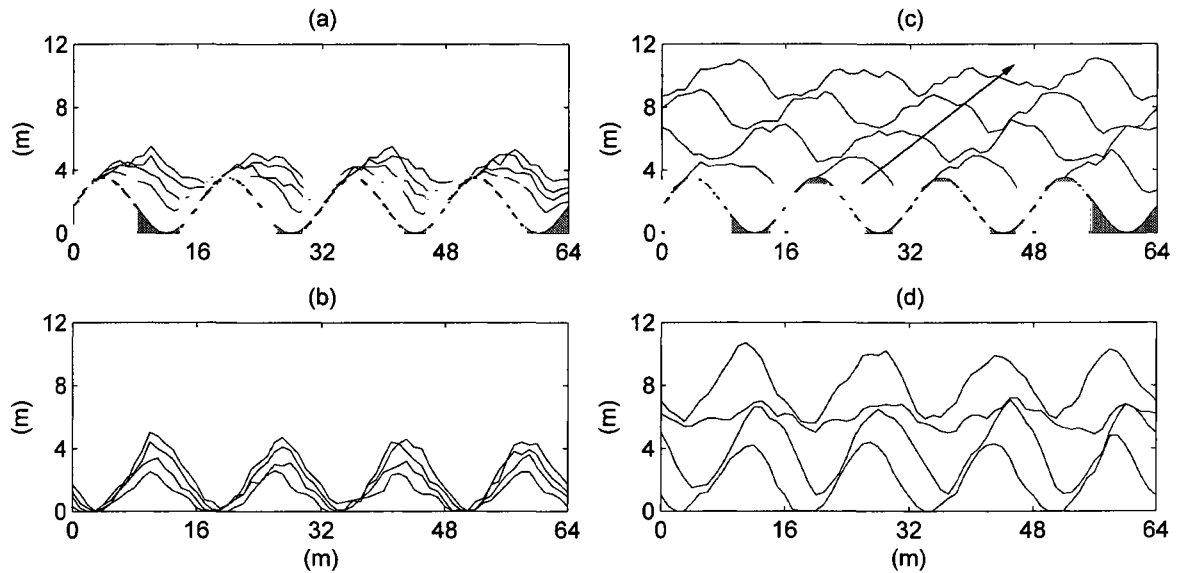
Figure 4.5. Snow depth profiles simulated using a sinusoidal topography (in gray) for two

scenarios: with densification ((a) and (b)) and without densification ((c) and (d)). Results

for every four weeks are shown from the bottom up. The integrated profiles of

topography + snow depth are shown in (a) and (c), and the profiles of snow depth only

are shown in (b) and (d).

Results obtained from the densification model are shown in Figure 4.6, in which four

snow density profiles every four weeks are shown for a cross section in one of the

maxima of the profiles in Figure 4.5b. The differences in the profiles illustrate the two

features that the representation allows: time evolution of snow density and the vertical

stratigraphy of the snowpack. At the end of week four, snow density varies between 100

kg/m^3 and 380 kg/m^3, while at the end of week 16, snow density varies between 100

kg/m^3 and 520 kg/m^3. The change in the depth of the layers through time can also be

observed, with a fast reduction in the depth of the new layers during the first weeks

following deposition. *Kojima* [1967] compared similar snow density profiles obtained

137

using the model with observations in the month of January obtaining a close fit between the two. *Motoyama* [1990] tested the consistency of the model by estimating snow depths through time using the snow density model with the same set of parameters for several years, demonstrating that the same set can be used for different seasons at a given location with reasonable results. For illustrative purposes, a snow density profile measured in an environment in which wind redistribution has been shown by *Trujillo et al.* [2007] to be a dominant factor in the organization of the snow cover is shown in the upper right corner of Figure 4.6. The pit measurements were obtained on February 25, 2003, at the Buffalo Pass study area (Colorado, U.S.A.) as part of NASA's Cold Land Processes Experiment (CLPX) [*Cline et al.*, 2004; *Elder et al.*, 2009b]. Such collection date would correspond to around week 14 in the model. The measured snow densities vary between 70 kg/m^3 and 410 kg/m^3, a range similar to the ranges in the topmost 3 m of the simulated profile for corresponding time steps (e.g., 100 kg/m^3-405 kg/m^3 at week 12). Also, the shape of the simulated density profiles resembles the vertical variation observed in natural snow packs. These results are indicative of the realistic snow densities that can be obtained with the densification model implemented here.
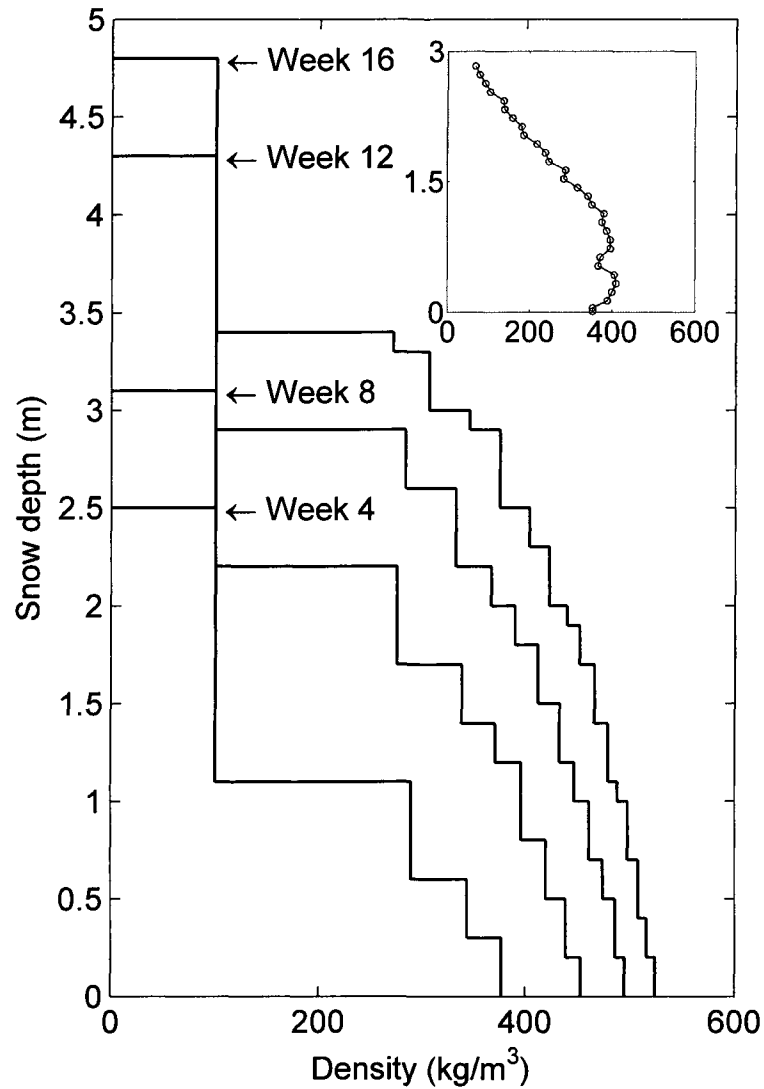
Figure 4.6. Snow density profiles every four weeks for a cross section in one of the deepest points in the snow profile shown in Figure 4.5(b). A profile of snow density measured in a wind dominated area in Colorado (U.S.A.) is shown in the smaller frame at the upper right corner for comparison.

Figure 4.7 illustrates the sensitivity of the simulated longitudinal snowpack characteristics to the length of the transport trajectory. The two simulations were run using the same parameters used for the model shown in Figure 4.5a and b, although the

transport trajectory was set to 8 m and 16 m in the x direction. These two lengths coincide with a half cycle and a full cycle of the sinusoidal topography. The results obtained using $L_x = 8$ m are very similar to the results from the model shown in Figure 4.5a and b, with accumulation zones on the lee side of the topographic ridges and erosion on the upwind side. On the other hand, the results obtained using $L_x = 16$ m are significantly different, with flat snow depth profiles, conforming a surface that is roughly parallel to the topographic surface, as if no redistribution had occurred. The coincidence between the magnitude of the vector L and the wavelength of the topography causes the source and destination cells to be located at an equivalent position in consecutive ridges, which after numerous iterations leads to a relatively uniform distribution of the snow slabs. This behavior only occurs when the magnitude of L and the separation between the ridges coincide. Longer and shorter trajectories lead to results that are statistically equivalent to each other, showing little sensitivity to the magnitude of L, as tested with several other lengths (not shown). These results illustrate that the sensitivity of the model to the magnitude of L is dependent on the characteristics of the topography, i.e., separation between topographic ridges.
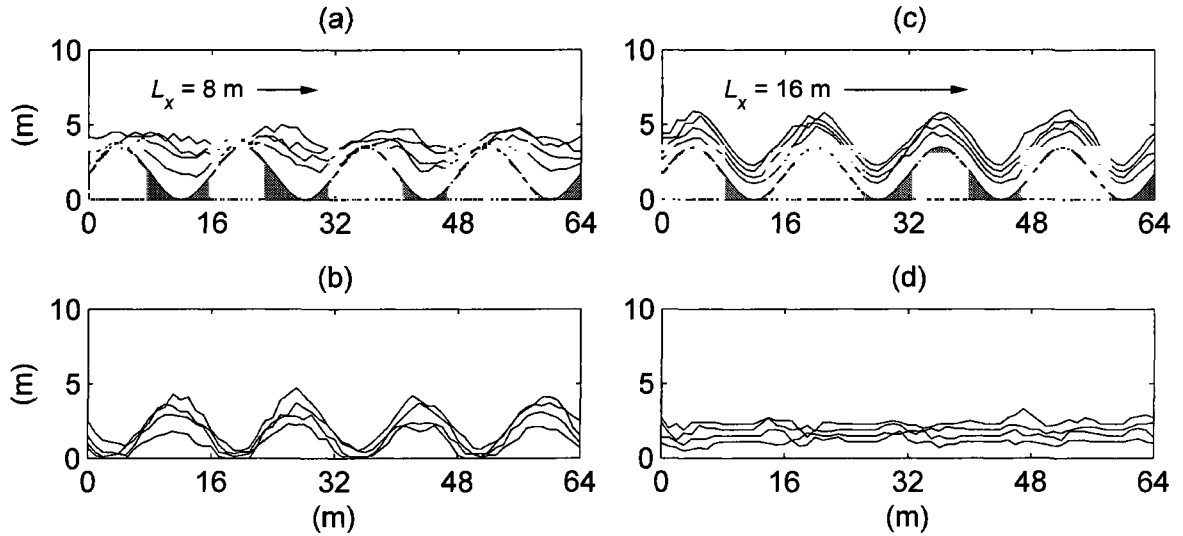
Figure 4.7. Snow depth profiles simulated with two different transport trajectories. Results for every four weeks are shown from the bottom up. The integrated profiles of topography + snow depth are presented in (a) and (c), and the profiles of snow depth only are presented in (b) and (d).

4.4.2 Synthetic Topography with k^{-2} Spectrum

The next set of simulations is performed over synthetic topographic fields exhibiting the spectral properties of real topography documented in several studies [e.g., *Mandelbrot*, 1982; *Brown*, 1987; *Turcotte*, 1987; *Huang and Turcotte*, 1989; *Turcotte*, 1989; *Trujillo et al.*, 2007]. In these studies, the power spectral density of terrain elevation (i.e., topography) was found to follow a power law relationship with frequency, with one-dimensional spectral exponent values of around 2.0, which corresponds to Brownian motion. The fields were generated using a Fourier filtering technique in which the two-dimensional Fourier transform coefficients of a white noise field are adjusted

141

according to the desired power spectral exponent. The new field is generated by performing an inverse Fourier transform using the modified coefficients. Details on the implementation of the methodology can be found in *Trujillo et al.* [2009]. The fields were smoothed out to eliminate the small scale surface roughness by applying a moving average over a square window of side dimension of 32 m.

4.4.2.1 Spatial Domain of 128 by 128

The first simulation is performed with the objective of analyzing the effects of increasing transport volumes on the organization and statistical properties of the snow fields. For this scenario, a square topographic field of side dimension of 128 is used (Figure 4.8). The size of the field was chosen to reduce computational time but ensuring a size large enough to represent the topographic interactions observed in reality. The transport vector, L, was set to 4 m in the x direction. Weekly precipitation values were set to 50 mm (5 slabs with $\rho_o = 100$ kg/m^3) distributed uniformly over the domain. All of the remaining parameters are the same as those used in the sinusoidal topography simulations. The volume of precipitation to transport (precipitation step) is set to 0.5, 1, 3, and 5 times the volume of precipitation. In Figure 4.9, results from the simulations with precipitation steps of 1.0 and 5.0 are shown. In the figure, the fields of topography + snow depth (a and c) and snow depth (b and d) at the end of week 16 are shown for each of the simulations. Comparison of the topography in Figure 4.8 with the topography + snow depth fields (Figure 4.9a and c) illustrate how some of the depressions in the topography fill in and some high accumulation areas develop on the lee side of topographic ridges. The size of these accumulation and scour areas increases as the

142

volume of transport increases. The snow depth fields (Figure 4.9b and d) are significantly different, with deeper snow depths in the high accumulation areas for the higher transport case, while the variations in snow depth occur over shorter separations for the lower transport case.
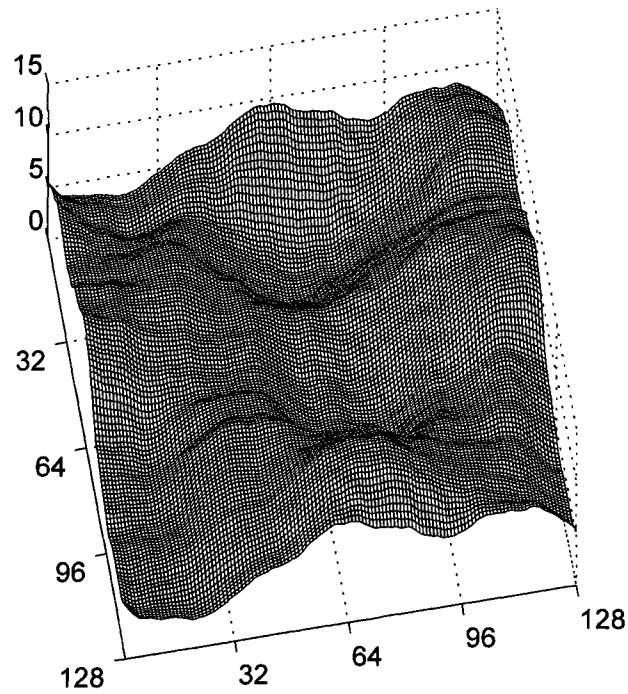
Figure 4.8. Synthetic topographic surface used in the first set of simulations for the Brownian motion case.
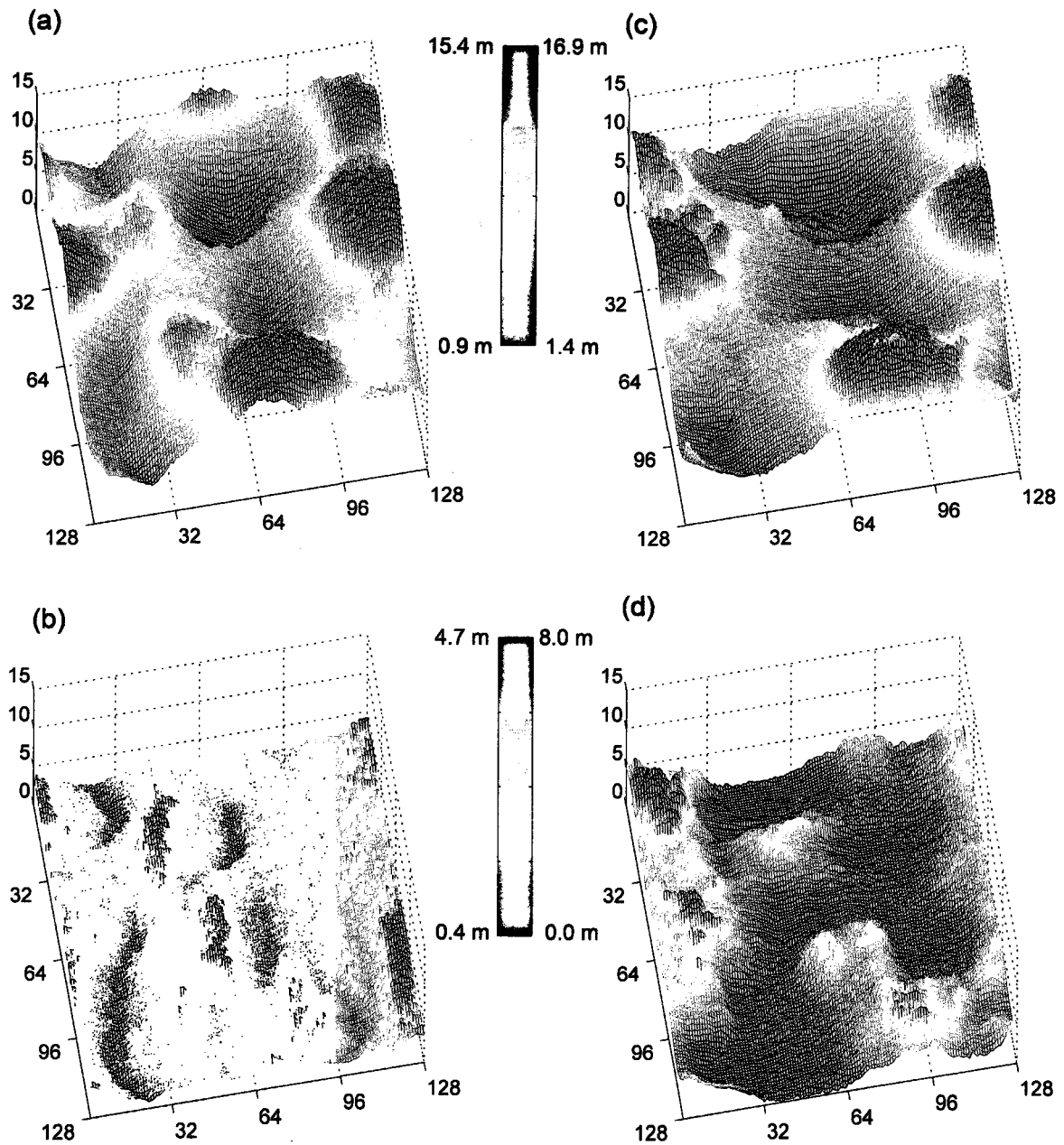
Figure 4.9. Snow depth fields at the end of week 16 simulated using the topography

shown in Figure 4.8 for precipitation steps of (a) 1.0 and (b) 5.0.

A comparison of the frequency distributions of snow depth every four weeks for the

different simulations with transport volumes between 0.5 and 5.0 is presented in Figure

4.10. As time progresses within each of the simulations, the frequency distributions of snow depth move to the right, that is, the mean snow depth increases and the range of snow depths gets wider, as expected (i.e., mass is conserved). The comparison also shows that the distributions progress from Gaussian distributions for the low transport volumes to distributions highly skewed to the right for the higher transport volumes. The distributions become flatter over a wider range as the volume of transport increases. These results are similar to what we have observed from LIDAR snow depth fields in alpine and wind dominated environments, for which positively skewed distributions have been obtained, with higher standard deviation values and wider snow depth ranges [e.g., *Trujillo et al.*, 2009]. Also, the appearance of bare-ground patches can be observed in the snow depth distributions for the higher transport volumes (Figure 4.10c and d), with the frequencies that correspond to zero and low values increasing with the transport volume. To complement these observations, the relationships between the standard deviation of snow depth and the precipitation step every four weeks are shown in Figure 4.11. Results for a simulation with precipitation step of 10.0 were added to the figure. The standard deviation shows an increase with the volume of transport, with a steeper increase at low transport volumes, and a stabilization trend at high transport rates. These results indicate that in a given area, changes in wind regimes between seasons induce changes in the statistical properties of the snow depth fields from year to year, and that those differences are less significant between seasons with already high transport volumes.
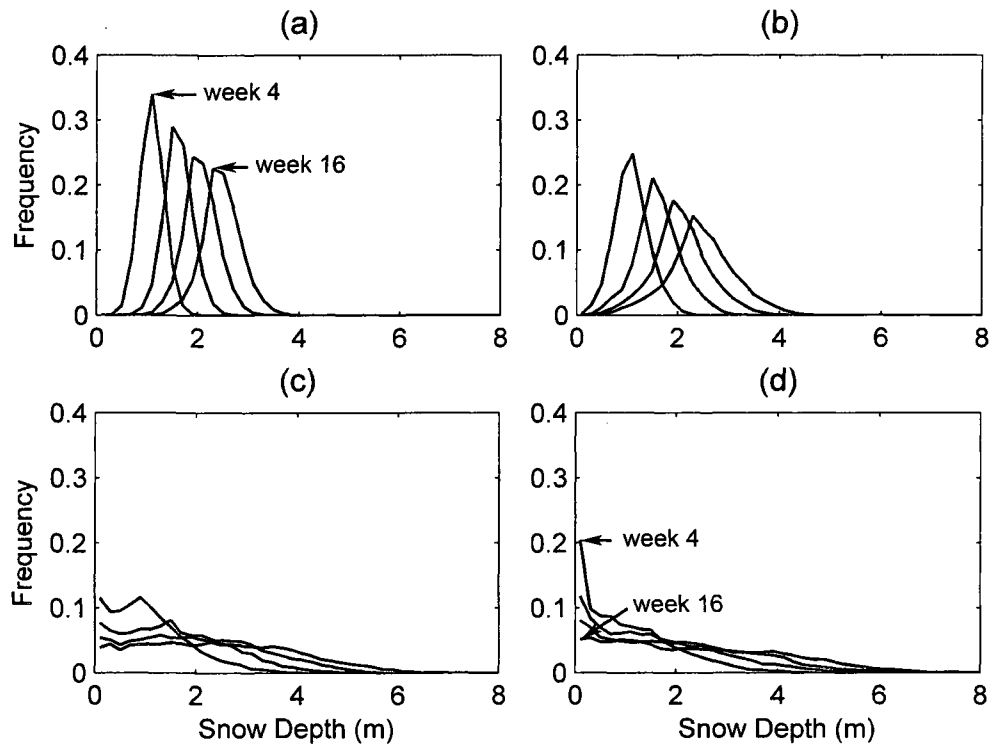
Figure 4.10. Frequency distributions of snow depth every four weeks simulated using the topography shown in Figure 4.8, and for precipitation steps of (a) 0.5, (b) 1.0, (c) 3.0 and (d) 5.0.
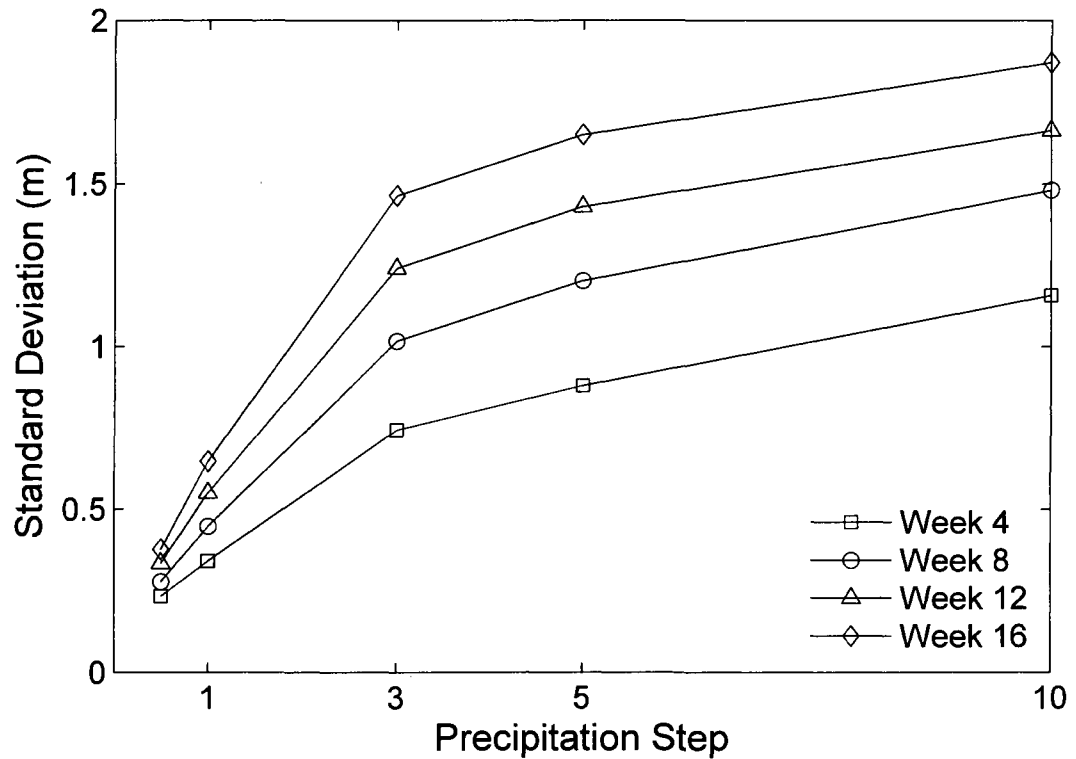
Figure 4.11. Standard deviation of snow depth versus precipitation step every four weeks.

The results from these simulations show that the statistical properties of snow depth fields throughout the accumulation period in wind dominated environments depend on the transport volumes of snow, which are dependent on meteorological conditions (e.g., winds and temperature). The inter-seasonal consistency of the spatial organization of snow covers in wind-dominated environments is conditioned to the consistency of wind transport potential. Years with differences in wind regimes and meteorological conditions (e.g., wind speeds and temperatures) will exhibit differences in the spatial statistical properties of snow cover properties (e.g., depth and SWE).

4.4.2.2 Spatial Domain of 128 by 128 with Meadow Vegetation

The following simulation is performed using the topographic field in Figure 4.12 with the objective of illustrating the control exerted by meadow vegetation in the organization of snow depth fields under high wind conditions. The field was generated to have an undulating topography with slopes low enough not to create shadow zones on the downwind slope. Instead, the topographic surface is used to identify low elevation areas (depressions) in which meadow vegetation frequently exists due to the convergence of melting and precipitated water caused by the gravitational gradients induced by the topography. Subsequently, the vegetation pattern shown in Figure 4.12 was generated in the topographic depressions with vegetation height values following an uncorrelated log-normal distribution with a mean of 1.0 and a standard deviation of 0.1. The field of vegetation effectiveness was generated following a linear relationship with height, reaching a maximum effectiveness of one at a height of 1.5 m. The simulations were performed using a lower weekly precipitation of 10 mm of SWE (1 slab with ρ_o =100 kg/m^3) to avoid the complete burial of the vegetation. A high precipitation step value of 5 was chosen to allow for significant redistribution making the effect of the vegetation more noticeable. The vector L was again set to be 4 m in the x direction. All of the remaining parameters are the same as those used in the simulations above (i.e., Figure 4.9).
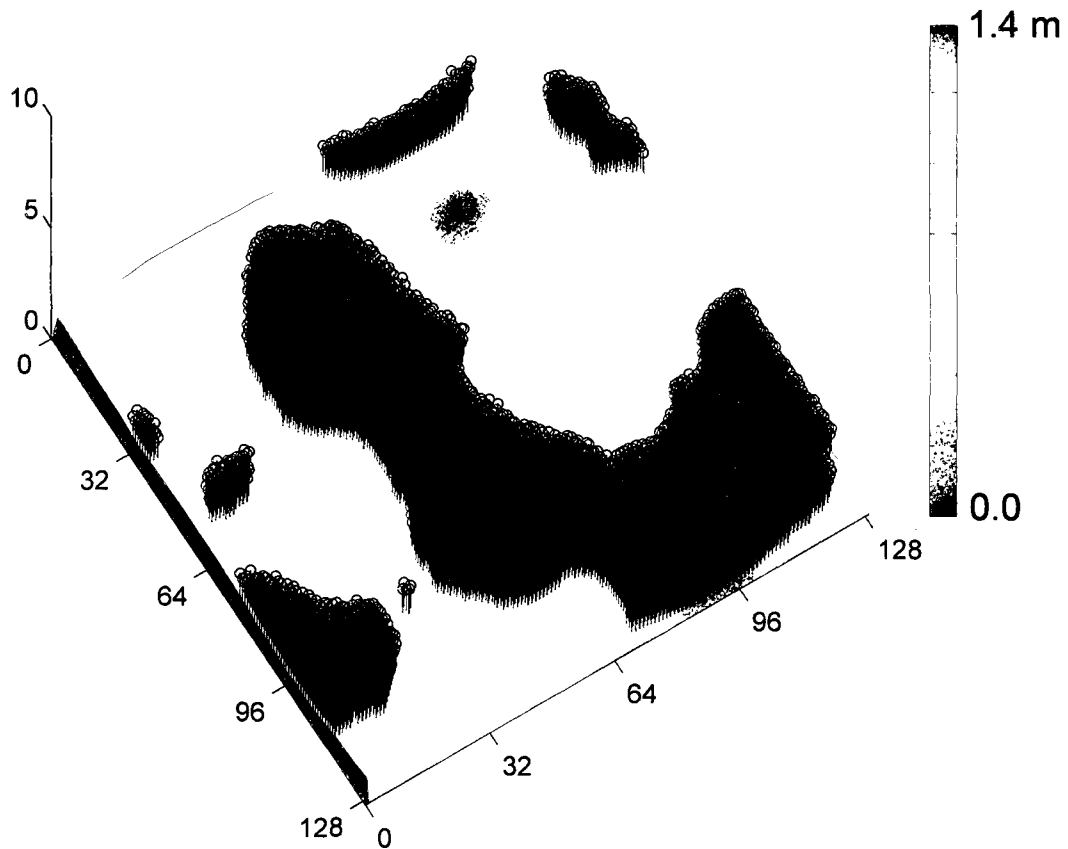
Figure 4.12. Synthetic topography with meadow vegetation (black stems) used for the

simulation in Figure 4.13.

Results from the simulation are presented in Figure 4.13. The snow depth field

obtained at the end of week 16 (Figure 4.13a) shows how the vegetation acts as a trap for

the snow directly precipitated in the meadow and for the snow blown from the bare areas.

Before the vegetation gets fully covered, more energy is required to remove the snow in

the meadow than in the open, and the reduction in wind speeds on the vegetated area

causes more snow to be deposited. These processes are represented here by the increase in the probabilities of deposition and the reduction of the probabilities of removal by the vegetation. Also, within the meadow, higher accumulations are observed in the upwind side of the vegetated area because more snow is transported downwind from the bare areas neighboring the meadow than from within the meadow. A similar pattern is observed at other times throughout the simulation (not shown). The time variations in the statistical properties (i.e., mean and standard deviation) of snow depth in both the meadow and bare areas are shown in Figure 4.13b. The mean snow depth is, on average, 0.20 m higher in the vegetated area, although the difference varies between 0.11 m at the beginning of the simulation period and 0.24 m towards the end of the simulation. On the other hand, the time variations in the standard deviation of snow depth exhibit a different behavior within both areas. In the bare areas, the standard deviation shows a monotonic increase through time from about 0.1 m at the beginning of the simulation to 0.2 m at the end. On the other hand, the standard deviation in the vegetated area shows little variations around a mean value of 0.17 m, although without any particular trend. These results indicate that for the conditions simulated, the variability within the vegetated area remains relatively uniform through time, while the variation around the mean continues increasing through time in the bare area. To the authors' knowledge, no evidence of this behavior has been presented in the existing literature.
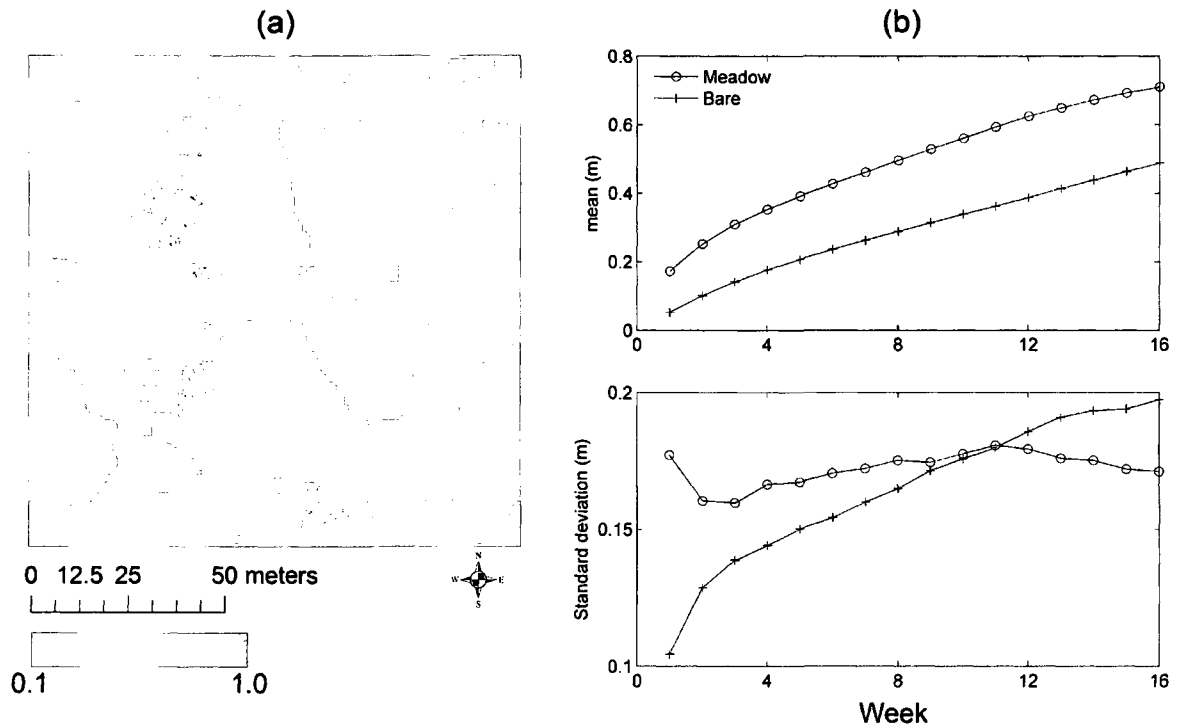
Figure 4.13. Results obtained from the simulation with the synthetic topography and vegetation patterns shown in Figure 4.12. (a) Simulated snow depth field at the end of week 16, and (b) mean and standard deviation as a function of time for both, vegetated (meadow) and bare areas.

4.4.2.3 Spatial Domain of 512 by 512

The following simulation is performed over a domain of 512 by 512 to extend the spatial coverage of the model, providing information over spatial scales similar to the scales analyzed in previous studies of the spatial organization of snow fields in wind dominated environments [e.g., *Trujillo et al.*, 2007; 2009]. The simulation is performed using a new topographic field (Figure 4.14) generated using the Fourier filtering technique described above. Besides the increase in the domain extent, two significant

151

extensions of the model are introduced in the following simulations to improve the representation of the physics of the transport processes. To define these extensions, data from a meteorological station located in the Alpine Intensive Study Area (ISA) of the CLPX collected in the winter 2002/2003 [*Elder and Goodbody*, 2004; *Elder et al.*, 2009a] are used to provide physical support to the model extensions.
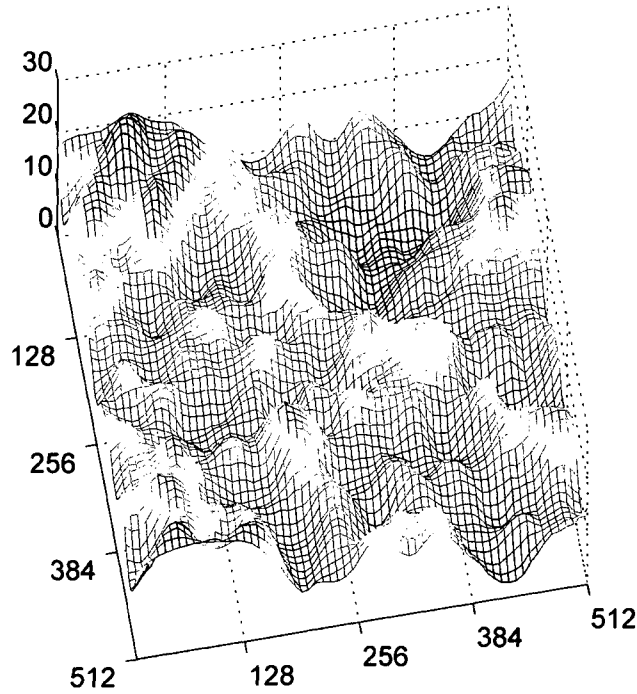
Figure 4.14. Synthetic topographic surface used in the second set of simulations for the case of topography with k^{-2} spectrum.

First, the initial density of the freshly fallen snow is now variable through time to represent the variations in density as a result of changes in atmospheric conditions, in this case, as a response to variations in air temperature. Although the density of fresh snow is also dependent on several other factors such as shape and configuration of snow crystals,

wetness, and winds, temperature persistently shows significant correlation values with fresh snow density [e.g., *Hedstrom and Pomeroy*, 1998; *Judson and Doesken*, 2000]. Temperature has been used in several studies to define regression relationships with snowfall density using linear models [e.g., *Diamond and Lowry*, 1953] and exponential models [e.g., *Hedstrom and Pomeroy*, 1998], among others. Although these models do not explain the full range of variability of fresh snow density, they do capture the average behavior, making such approximations adequate for the simulations performed in this study. The following simulations are performed using the linear model in (4.8):

$$\rho_o(T) = \rho_o(0) + kT, \qquad T \le 0°C \qquad (4.8)$$

where $\rho_o(T)$ is the fresh snow density at a temperature of T. The slope (k) was selected to be 0.005 kg/m^3/°C to reproduce the average results from observations of fresh snow density in the Rabbit Ears area in the Colorado Rocky Mountains presented in *Judson and Doesken* [2000]. Weekly average temperatures were obtained from the meteorological station in the Alpine ISA for the period between November 2002 and March 2003 (Figure 4.15). These temperature values were then used to estimate the fresh snow density values for each week shown in Figure 4.15. Weekly precipitation totals for the concurrent period in 2002-2003 were also obtained from a nearby SNOTEL station (Rabbit Ears-CO06J09S) (Figure 4.15) to complement the model inputs.
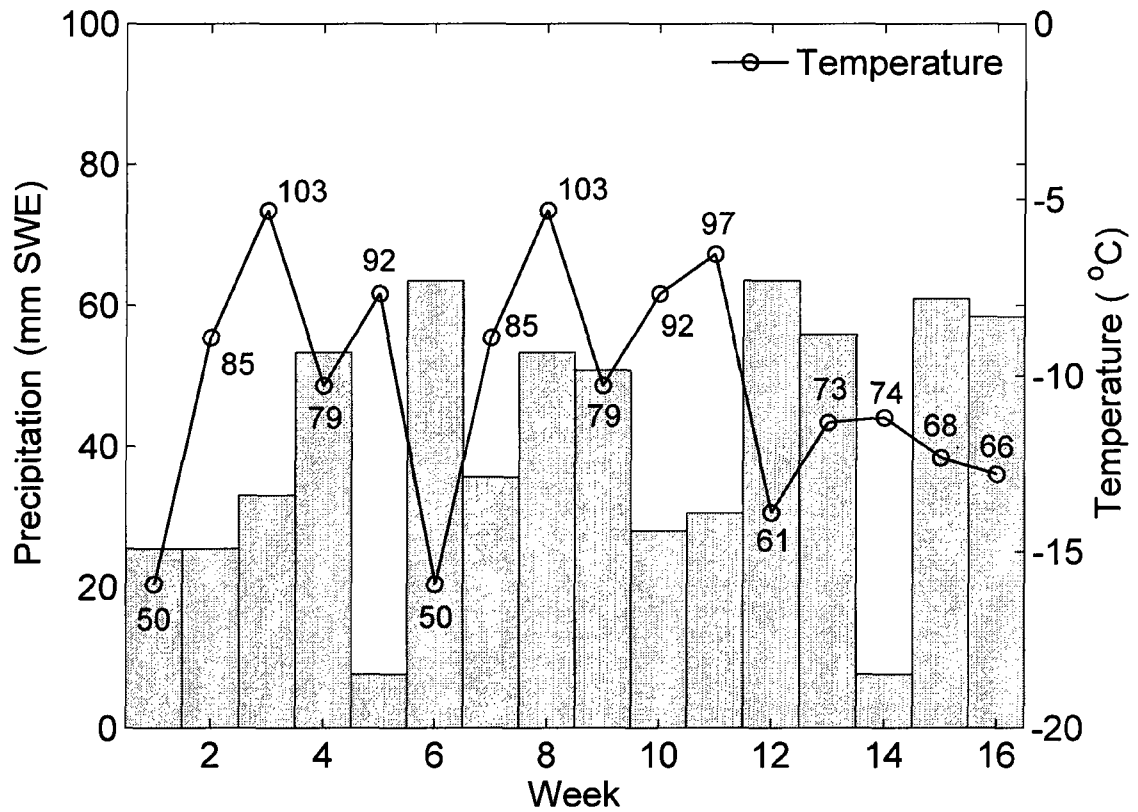
Figure 4.15. Weekly temperatures and precipitation used in the simulation shown in Figure 4.17. The fresh snow density values (in kg/m^3) corresponding to each temperature are shown next to each weekly marker.

The second model extension concerns the representation of the probabilities of removal and transport trajectories, which are highly dependent on the predominant wind directions and the corresponding wind speeds. Wind transport of deposited snow is initiated when a particular threshold speed is exceeded [*Kind*, 1990]. Such threshold speed is highly variable in space and in time, and it is highly dependent on atmospheric conditions and snow characteristics [*Li and Pomeroy*, 1997]. Threshold wind speeds (at z = 10 m) for snow transport have been measured to range between 4 m/s and 11 m/s for

154

dry snow conditions, and between 7 m/s and 14 m/s for wet snow conditions [*Li and Pomeroy*, 1997]. Also, the transport trajectories (length and direction) depend on the predominant wind directions and the corresponding wind velocities. To represent these processes, the meteorological data from the Alpine ISA are analyzed to define the parameters of wind direction and transport trajectories based on observations. The distribution of wind direction for the period between November 2002 and March 2003 (16 weeks) are shown in Figure 4.16a, while the distribution and mean of wind speed corresponding to each of the direction bins are shown in Figure 4.16b. This analysis illustrates that the predominant wind directions are also associated with higher wind speeds and are distributed over wider ranges, which translates to significantly larger transport rates over longer distances along the predominant wind directions. The distribution of wind direction was then combined with the proportion of wind speeds above a threshold value of 4 m/s to determine a conditional distribution of wind direction so that transport of snow will occur along each given direction according to the distributions in Table 4. The value of the threshold wind speed was chosen to be relatively low given that new snow in the Rabbit Ears area is generally dry and exhibits relatively low densities [*Judson and Doesken*, 2000], which facilitates the transport of newly deposited snow. No transport occurs along directions between 0° and 60° as the wind speeds along these directions do not exceed the threshold level required for snow removal (Table 4). Additionally, directional variations of the magnitude of the transport vector L are also introduced based on the observations, following a one to one linear increase in the magnitude of L with the conditional mean speeds, $\overline{V}$ ($\overline{V} \mid V \geq v_{threshold}$,

where V is the wind speed and $\overline{V}$ represents the mean) (Table 4). This representation

allows for longer transport lengths along the predominant wind directions.
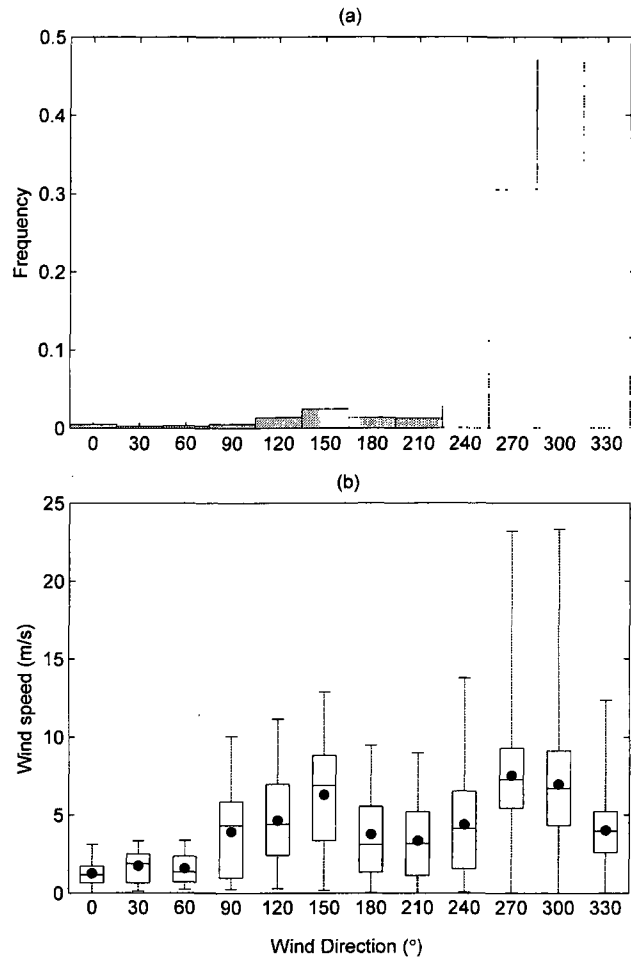
Figure 4.16. (a) Distribution of wind direction at the Alpine Intensive Study Area (ISA)

in the Colorado Rocky Mountains, and (b) Distributions of wind speed for each of the

wind directions. The whiskers cover the entire range of the data for each direction bin,

the lower and upper limits of the box mark the 0.25 and 0.75 percentiles, and the internal

line marks the median. The dots correspond to the mean of each set. Wind directions are

measured clockwise with respect to the north.

Table 4. Fractions of wind speeds greater than a threshold speed of 4 m/s ($p(v \geq 4$ m/s)), and average wind speeds for the values above 4 m/s as a function of direction for the wind data analyzed in Figure 4.16.

Direction (°)	$p(v \geq 4$ m/s)	Conditional frequency	Mean wind speed above 4 m/s
0	0.00	0.000	0.0
30	0.00	0.000	0.0
60	0.00	0.000	0.0
90	0.56	0.004	6.0
120	0.58	0.010	6.6
150	0.72	0.024	8.0
180	0.43	0.008	6.6
210	0.40	0.007	6.0
240	0.51	0.020	6.9
270	0.86	0.353	8.4
300	0.79	0.497	8.2
330	0.49	0.077	5.6

The simulated snow depth field at the end of week 16 is shown in Figure 4.17a. In the field, bands of low and high snow depths are aligned perpendicularly to the predominant wind directions, with deeper snow on the downwind side of topographic ridges, while shallow snow depths on the upwind slopes. The correlation structure of the field can be observed in Figure 4.17b, in which the two-dimensional correlation of snow depth at the end of week 16 is shown. The correlation function indicates a correlation structure that is consistent with the predominant wind directions, with an anisotropic behavior in which a stronger correlation structure exists along the perpendicular to the predominant wind directions. This structure is similar to the two-dimensional correlation structure of snow

depth observed in wind dominated environments, for which stronger correlations occur along directions perpendicular to the predominant wind directions [*Trujillo et al.*, 2009]. Another important feature is the existence of negative correlations of the order of -0.4 aligned with the predominant wind directions, and at lags of the order of 25 m to 30 m, comparable with the separation distances between the deep and shallow snow depth bands observed in the field. The analysis of the progression of the two-dimensional correlation functions through time (not shown) indicates that the correlation structure becomes stronger as time progresses, as the deep and shallow areas in the snow surface become more pronounced. A plot of standard deviation versus mean snow depth throughout the simulation is shown in Figure 4.17c. The figure indicates a linear increase, which is remarkably similar to the observations presented in *Egli and Jonas* [2009], who analyzed the hysteretic behavior of the curve of standard deviation versus mean snow depth using daily time series from 77 snow depth stations in the Swiss Alps, of which about 75% were located above tree-line. In their analysis, *Egli and Jonas* [2009] obtained a quasi-linear increase of the standard deviation with the mean snow depth during the accumulation period until a maximum is reached at the peak of the winter season. After the peak is reached, the trajectory retreats along the same path until a distinct turning point is reached. The remaining of the trajectory during the ablation period follows a clearly different path illustrating the hysteretic behavior of the curve. Evidence of the relationship using observations at the scales at which the model works has not, to the authors' knowledge, been presented in the literature. Finally, the temporal variation of mean snow density is shown in Figure 4.17d, with a range between 50 kg/m^3 and 325 kg/m^3, and with time variations that reflect the deposition of new snow.
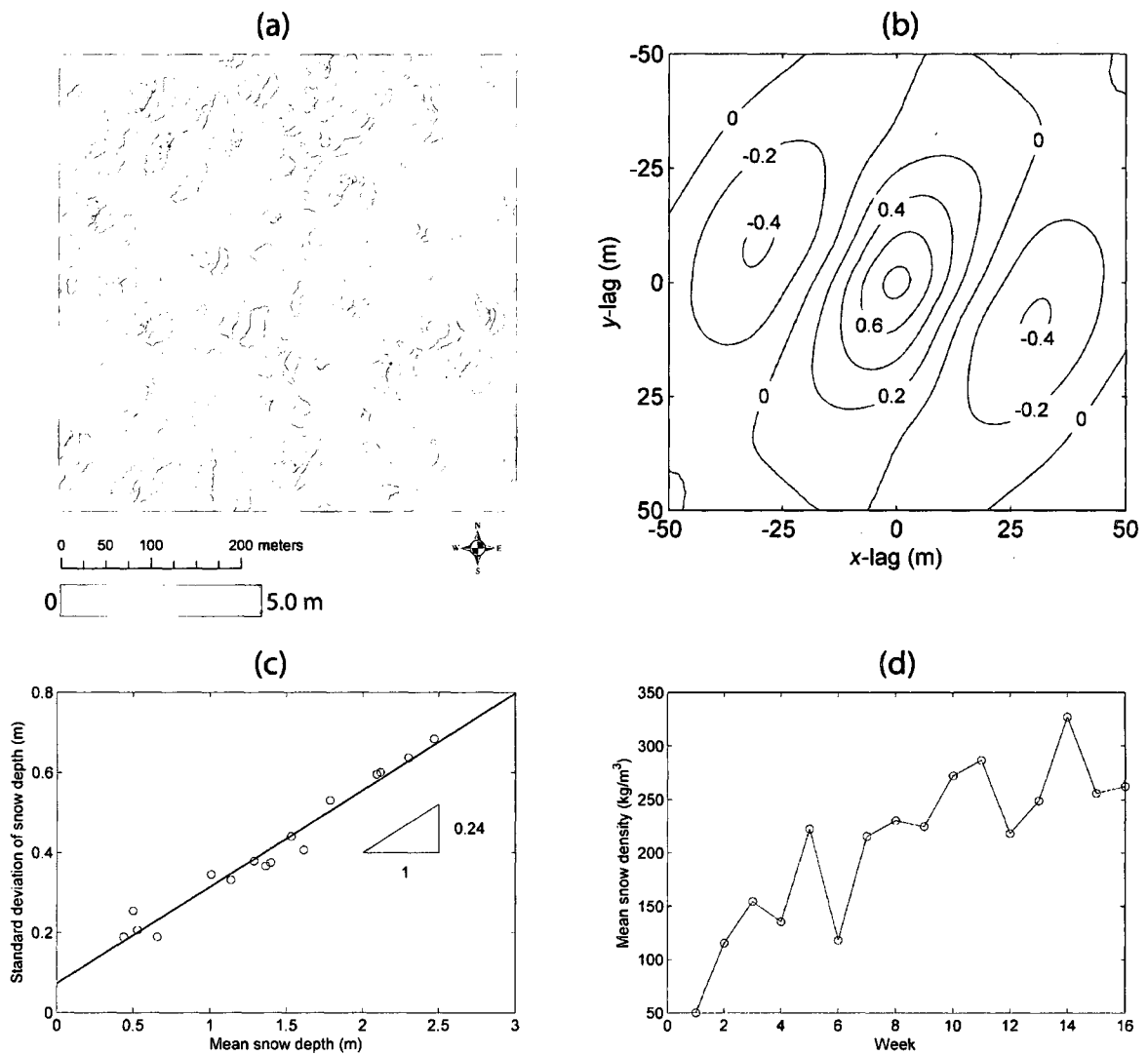
Figure 4.17. (a) Simulated snow depth field at the end of week 16; (b) Two-dimensional

correlation function for the simulated field at the end of week 16; (c) Standard deviation

versus mean snow depth for the simulated fields (each point corresponds to a weekly

pair); (d) Progression of the mean snow density throughout the simulation period.

A comparison of the simulated snow depth field at the end of week 16 with LIDAR snow depths obtained on April 8, 2003 in the Walton Creek ISA of the CLPX [*Miller*, 2003] is shown in Figure 4.18. The Walton Creek ISA is located in the Rabbit Ears area in Colorado, and the spatial organization of snow depth has been shown to be controlled by wind redistribution, and the interactions of the winds with topography and vegetation [*Trujillo et al.*, 2007]. Figure 4.18a shows a section of the LIDAR field in which the interaction between the blowing snow and the undulating topography has induced a pattern of snow distribution with eroded areas in the upwind slopes and deposition areas in the downwind slopes. This pattern of organization is remarkably similar to the pattern obtained from the simulation performed using the synthetic topography shown in Figure 4.14. Both fields exhibit high and low accumulation areas separated by comparable distances, and with similar shapes and ranges of variation, illustrating the capabilities of the model to reproduce the characteristics of the spatial organization of snow depths in wind dominated environments. Further development of the model would allow for improvements in the representation of wind patterns, snow removal and deposition, and additions of other types of vegetation (e.g., ribbon forest).

(a)

0   4.1

(b)

⟶ Predominant
wind direction

0   5.0

0   50   100   200 meters
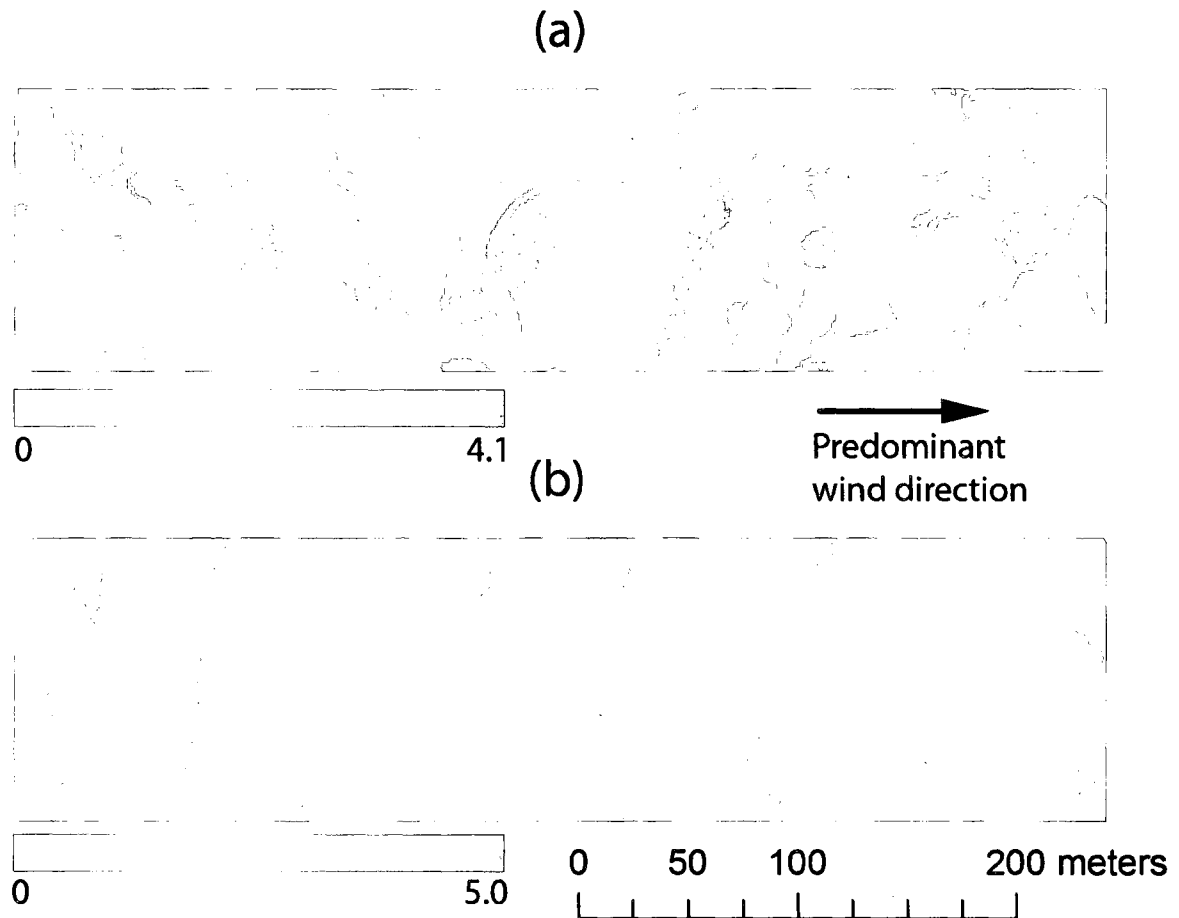
Figure 4.18. Comparison of (a) high-resolution LIDAR snow depths at the Walton Creek

ISA in April/2008 and (b) the simulated snow depths in Figure 4.17a.

4.5 Summary and Conclusions

A cellular automata model for simulating the evolution of snow packs in areas in which wind transport of snow and its interactions with terrain and short alpine vegetation are dominant is introduced. The model is designed to work at small spatial scales (~1 m) and over weekly time steps. The processes simulated include a layered snowpack formed by accumulating weekly precipitation, a physically based densification scheme that

161

accounts for the compaction of the snow layers, and the interaction between the blowing snow with small-scale topographic features and vegetation. Other features include the possibility of time-variable transport trajectories, space- and time-variable precipitation, and time-variable initial density. The erosion and deposition of particles is determined according to a predefined set of probabilities dependent upon the location of the grid cells relative to aerodynamic obstacles and the vertical angles with such obstacles. The interaction with the vegetation is simulated using a set of probabilities that depend on the height of the vegetation, and a relationship that relates the exposed vegetation height to the vegetation effectiveness.

The simulations indicate that when no densification of snow is allowed, the behavior of the snow surface is very similar to the behavior of sand in environments in which wind transport is a dominant process and in which downwind migration of sand dunes occurs. The results also show that the representation of the process of densification is of paramount importance to appropriately simulate the evolution of the snow pack in wind dominated environments. The sensitivity to variations in the transport volumes shows that the size of accumulation and eroded areas increases with transport volumes. Also, the variability of the snow depth fields occurs over shorter distances in the low transport cases. Analysis of the time evolution of the statistical distribution functions of the simulated fields shows that as time increases the mean snow depth increases and the snow depth values have wider ranges. Also, the distributions progress from Gaussian distributions for low transport rates to distributions highly skewed to the right for the higher transport rates. These results are in accordance with previous observations of the distributions of snow depth in environments in which wind redistribution of snow is

162

dominant, for which highly skewed distribution functions have been observed. Analyses of the standard deviation of snow depth as a function of the transport volumes indicate a steep increase in the standard deviation at low transport values, while the rate of increase decreases for the higher transport volumes. However, the standard deviation did not reach a stabilization point within the transport volume ranges analyzed. These results indicate that in a given location, changes in wind regimes between seasons induce changes in the statistical properties of the snow depth fields, and that those differences are less significant between seasons with already high transport volumes. The simulation performed using synthetic topography with low relief and meadow vegetation shows that this type of vegetation acts, until fully buried, as a trap for snow directly precipitated in the meadow and for the snow blown from the upwind bare portions. Also, the snow depth field in the vegetated area exhibits higher means and a relatively uniform standard deviation, while in the bare areas the field shows an increase in the standard deviation with time, indicating increases in the variability through time.

The results from the simulation performed over synthetic topographic domains of the order of 500 m and with time variations in precipitation, fresh snow density and wind characteristics (i.e., wind directions and transport distances) reproduce the time and space variations of snow cover properties previously observed in wind dominated environments in several locations. The spatial patterns of the simulated snow depth fields, the anisotropy in the two-dimensional correlation function, and the time progression of the snow cover (i.e., standard deviation as a function of the mean snow depth, and density changes throughout the season) resemble the observations presented in several studies, illustrating the potential of the model for studying the effect of changes in atmospheric

conditions (i.e., precipitation, temperature and winds) and physiographic conditions (i.e., topography and vegetation) on the spatial organization of snow cover properties (i.e., snow depth, snow density and SWE) during the accumulation period.

Overall, the results presented here show that the statistical properties of snow depth fields throughout the accumulation period in wind dominated environments depend on the transport volumes of snow, which are dependent on meteorological conditions (e.g., winds and temperature). The inter-seasonal consistency of the spatial organization of snow covers in wind-dominated environments documented in several studies is conditioned to the consistency of wind patterns and wind transport potential. Years with differences in wind regimes and meteorological conditions (e.g., wind speeds and directions, temperatures) will exhibit differences in the spatial statistical properties of snow cover properties (e.g., depth and SWE). The magnitudes of the differences in the spatial statistical properties depend on the magnitudes of the differences in the meteorological conditions.

4.6 References

Arnaud, L., J. M. Barnola, and P. Duval (2000), Physical modeling of the densification of snow/firn and ice in the upper part of polar ice sheets, paper presented at *International Symposium on Physics of Ice Core Records*, Hokkaido University Press, Shikotsukohan, Hokkaido, Japan, September 14-17, 1998, *Physics of Ice Core Records*, 285-305.

Barpi, F., M. Borri-Brunetto, and L. D. Veneri (2007), Cellular-automata model for dense-snow avalanches, *J. Cold Regions Eng.*, *21*(4), 121-140.

Brown, S. R. (1987), A Note on the Description of Surface-Roughness Using Fractal Dimension, *Geophys. Res. Lett.*, *14*(11), 1095-1098.

Burns, S. J., and P. J. Tokin (1982), Soil-geomorphic models and the spatial distribution and development of alpine soils, in *Space and Time in Geomorphology*, edited by C. E. Thorn, pp. 25-43, Allen and Unwin, London.

Chopard, B., and A. Masselot (1999), Cellular automata and lattice Boltzmann methods: a new approach to computational fluid dynamics and particle transport, *Future Generat. Comput. Syst.*, *16*(2-3), 249-257.

Cline, D., R. Armstrong, R. Davis, K. Elder, and G. Liston (2004), CLPX-Ground: ISA Snow Pit Measurements, edited by M. P. a. M. J. Brodzik., National Snow and Ice Data Center, Boulder, CO.

Deems, J. S., S. R. Fassnacht, and K. J. Elder (2006), Fractal distribution of snow depth from lidar data, *J. Hydrometeor.*, *7*(2), 285-297.

Diamond, M., and W. P. Lowry (1953), Correlation of density of new snow with 700 mb temperature, *SURE Research Paper No. 1*.

Egli, L., and T. Jonas (2009), Hysteretic dynamics of seasonal snow depth distribution in the Swiss Alps, *Geophys. Res. Lett.*, *36*, L02501, doi: 10.1029/2008GL035545.

Elder, K., J. Dozier, and J. Michaelsen (1991), Snow accumulation and distribution in an alpine watershed, *Water Resour. Res.*, *27*(7), 1541-1552.

Elder, K., W. Rosenthal, and R. E. Davis (1998), Estimating the spatial distribution of snow water equivalence in a montane watershed, *Hydrol. Processes*, *12*(10-11), 1793-1808.

Elder, K., and A. Goodbody (2004), *CLPX-Ground: ISA Main meteorological data*, National Snow and Ice Data Center, Boulder, CO.

Elder, K., D. Cline, A. Goodbody, P. Houser, G. E. Liston, L. Mahrt, and N. Rutter (2009a), NASA Cold Land Processes Experiment (CLPX 2002/03): Ground-Based and Near-Surface Meteorological Observations, *J. Hydrometeor.*, *10*(1), 330-337, doi: 10.1175/2008jhm878.1.

Elder, K., D. Cline, G. E. Liston, and R. Armstrong (2009b), NASA Cold Land Processes Experiment (CLPX 2002/03): Field Measurements of Snowpack Properties and Soil Moisture, *J. Hydrometeor.*, *10*(1), 320-329, doi: 10.1175/2008jhm877.1.

Erickson, T. A., M. W. Williams, and A. Winstral (2005), Persistence of topographic controls on the spatial distribution of snow in rugged mountain terrain, Colorado, United States, *Water Resour. Res.*, *41*, W04014, doi: 10.1029/2003WR002973.

Erxleben, J., K. Elder, and R. Davis (2002), Comparison of spatial interpolation methods for estimating snow distribution in the Colorado Rocky Mountains, *Hydrol. Processes*, *16*(18), 3627-3649.

Evans, B. M., D. A. Walker, C. S. Benson, E. A. Nordstrand, and G. W. Petersen (1989), Spatial interrelationships between terrain, snow distribution and vegetation patterns at an arctic foothills site in Alaska, *Holarctic Ecol.*, *12*(3), 270-278.

Frezzotti, M., S. Gandolfi, F. La Marca, and S. Urbini (2002), Snow dunes and glazed surfaces in Antarctica: new field and remote-sensing data, *Ann. Glaciol.*, *34*(1), 81-88 (88), doi: 10.3189/172756402781817851.

Gravner, J., and D. Griffeath (2006), Modeling snow crystal growth I: Rigorous results for Packard's digital snowflakes, *Exp. Math.*, *15*(4), 421-444.

Greene, E. M., G. E. Liston, and R. A. Pielke (1999), Relationships between landscape, snowcover depletion, and regional weather and climate, *Hydrol. Processes*, *13*(14-15), 2453-2466.

Havholm, K. G., and G. Kocurek (1988), A preliminary study of the dynamics of a modern draa, Algodones, Southeastern California, USA, *Sedimentology*, *35*(4), 649-669.

Hedstrom, N., and J. W. Pomeroy (1998), Intercepted snow in the boreal forest: measurements and modelling, *Hydrol. Processes*, *12*, 1611-1625.

Hiemstra, C. A., G. E. Liston, and W. A. Reiners (2002), Snow redistribution by wind and interactions with vegetation at upper treeline in the Medicine Bow Mountains, Wyoming, USA, *Arctic Antarct. Alpine Res.*, *34*(3), 262-273.

Huang, J., and D. L. Turcotte (1989), Fractal mapping of digitized images: Application to the topography of Arizona and comparison with synthetic images, *J. Geophys. Res. Solid Earth Planets*, *94*(B6), 7491-7495.

Izumi, K. (1984), Snow density and electric conductivity of daily snowfall observed in Niigata, Annual Report of the Research Institute for Hazards in Snowy Areas, No. 6, 103–109 pp, Niigata University.

Judson, A., and N. Doesken (2000), Density of freshly fallen snow in the Central Rocky Mountains, *Bull. Am. Meteorol. Soc.*, *81*(7), 1577-1587.

Kajikawa, M. (1989), Relationship between new snow density and shape of crystals, *Seppyo*, *51*, 178–183.

Kind, R. J. (1990), Mechanics of aeolian transport of snow and sand, *J. Wind Eng. Ind. Aerodyn.*, *36*, 855-866.

Kojima, K. (1957), Viscous compression of natural snow layer III, *Low Temp. Sci. Ser. A*, *16*, 167-196.

Kojima, K. (1967), Densification of seasonal snow cover, *Physics of Snow and Ice : proceedings*, *1*, 929-952.

Kojima, K. (1975), A field experiment on the rate of densification of natural snow layers under low stresses, paper presented at *Snow Mechanics Symposium*, Grindelwald, Bernese Oberland (Switzerland), April 1974, *International Association of Hydrological Sciences Publication*, *114*, 298-308.

Komárková, V. (1979), Alpine vegetation of the Indian Peaks area, Front Range, Colorado Rocky Mountains, in *Flora et vegetatio mundi, VII*, edited by R. Tuxen, pp. 1–591, J. Cramer, Vaduz, Germany.

Kronholm, K., and K. W. Birkeland (2005), Integrating spatial patterns into a snow avalanche cellular automata model, *Geophys. Res. Lett.*, *32*(19).

Kuchment, L. S., and A. N. Gelfan (2001), Statistical self-similarity of spatial variations of snow cover: verification of the hypothesis and application in the snowmelt runoff generation models, *Hydrol. Processes*, *15*(18), 3343-3355.

Li, L., and J. W. Pomeroy (1997), Estimates of threshold wind speeds for snow transport using meteorological data, *J. Appl. Meteorol.*, *36*, 205-213.

Liston, G. E., and M. Sturm (1998), A snow-transport model for complex terrain, *J. Glaciol.*, *44*(148), 498-516.

Liston, G. E. (1999), Interrelationships among snow distribution, snowmelt, and snow cover depletion: Implications for atmospheric, hydrologic, and ecologic modeling, *J. Appl. Meteorol.*, *38*(10), 1474-1487.

Liston, G. E., R. A. Pielke, and E. M. Greene (1999), Improving first-order snow-related deficiencies in a regional climate model, *J. Geophys. Res. Atmos.*, *104*(D16), 19559-19567.

Liston, G. E. (2004), Representing subgrid snow cover heterogeneities in regional and global models, *J. Clim.*, *17*(6), 1381-1397.

Liston, G. E., C. A. Hiemstra, K. Elder, and D. Cline (2008), Mesocell Study Area snow distributions for the Cold Land Processes Experiment (CLPX), *J. Hydrometeor.*, *9*(5), 957-976, doi: 10.1175/2008JHM869.1.

Luce, C. H., D. G. Tarboton, and R. R. Cooley (1998), The influence of the spatial distribution of snow on basin-averaged snowmelt, *Hydrol. Processes*, *12*(10-11), 1671-1683.

Luce, C. H., D. G. Tarboton, and K. R. Cooley (1999), Sub-grid parameterization of snow distribution for an energy and mass balance snow cover model, *Hydrol. Processes*, *13*(12-13), 1921-1933.

Mandelbrot, B. (1982), *The Fractal Geometry of Nature*, 468 pp., Freeman, San Francisco.

Masselot, A., and B. Chopard (1998), A lattice Boltzmann model for particle transport and deposition, *Europhys. Lett.*, *42*(3), 259-264.

McGinnis, D. L. (1997), Estimating climate-change impacts on Colorado Plateau snowpack using downscaling methods, *Prof. Geogr.*, *49*(1), 117-125.

Miller, S. L. (2003), *CLPX-Airborne: Infrared Orthophotography and LIDAR Topographic Mapping*, National Snow and Ice Data Center, Digital Media, Boulder, CO.

Momiji, H., R. Carretero-Gonzalez, S. R. Bishop, and A. Warren (2000), Simulation of the effect of wind speedup in the formation of transverse dune fields, *Earth Surf. Processes Landforms*, *25*(8), 905-918.

Motoyama, H. (1990), Simulation of seasonal snow cover based on air temperature and precipitation, *J. Appl. Meteorol.*, *29*, 1104-1110.

Ning, C., and C. A. Reiter (2007), A cellular model for three-dimensional snow crystallization, *Comput. Graph.*, *31*(4), 668-677.

Sato, T., K. Kosugi, S. Mochizuki, and M. Nemoto (2008), Wind speed dependences of fracture and accumulation of snowflakes on snow surface, *Cold Reg. Sci. Technol.*, *51*(2-3), 229-239.

Shook, K., and D. M. Gray (1996), Small-scale spatial structure of shallow snowcovers, *Hydrol. Processes*, *10*(10), 1283-1292.

Shook, K., and D. M. Gray (1997), Synthesizing shallow seasonal snow covers, *Water Resour. Res.*, *33*(3), 419-426.

Trujillo, E., J. A. Ramirez, and K. J. Elder (2007), Topographic, meteorologic, and canopy controls on the scaling characteristics of the spatial distribution of snow depth fields, *Water Resour. Res.*, *43*, W07409, doi: 10.1029/2006WR005317.

Trujillo, E., J. A. Ramirez, and K. J. Elder (2009), Scaling Properties and Spatial Organization of Snow Depth Fields in Sub-alpine Forest and Alpine Tundra, *Hydrol. Processes, In Press.*

Turcotte, D. L. (1987), A fractal interpretation of topography and geoid spectra on the Earth, Moon, Venus, and Mars, *J. Geophys. Res. Solid Earth Planets*, *92*(B4), E597-E601.

Turcotte, D. L. (1989), Fractals in geology and geophysics, *Pure Appl. Geophys.*, *131*(1-2), 171-196.

Walker, D. A., W. D. Billings, and J. G. De Molenaar (2001), Snow-vegetation interactions in tundra environments, in *Snow Ecology*, edited by H. G. Jones, et al., pp. 266-324, Cambridge University Press, New York.

Weitzenkamp, B., T. Sauter, A. Kraemer, R. Roth, and C. Schneider (2008), Spatial downscaling of snow cover as a tool for projections of snow availability for winter sports in 2030 in the Black Forest using Remote Sensing and GIS Methods, *Geophys. Res. Abstr.*, *10*, EGU2008-A-06206.

Werner, B. T. (1995), Eolian dunes: Computer simulations and attractor interpretation, *Geology*, *23*(12), 1107-1110.

Wolfram, S. (2002), *A new kind of science*, First ed., 1197 pp., Wolfram Media, Champaign, IL.

Xu, H., J. O. Bailey, E. C. Barrett, and R. E. J. Kelly (1993), Monitoring snow area and depth with integration of remote sensing and GIS, *Int. J. Rem. Sens.*, *14*(17), 3259-3268.

5 Summary and Final Remarks

LIDAR snow depths, bare ground elevations and elevations filtered to the top of vegetation, together with the analysis of synthetically generated profiles and fields of snow depth obtained using Fourier filtering and spectral techniques, and simulations performed using a cellular automata model for redistribution of snow by wind, were used to characterize the spatial organization and scaling properties of snow depth in different environments. The analyses show that the power spectra of snow depth behave as $k^{-\beta}$ within two distinct frequency intervals, each with different spectral exponent. The spectral exponents found for each of the intervals indicate that the snow depth surface is more variable (or rougher) when observed at scales larger than the corresponding scale break, while much smaller variations appear when looked at scales smaller than such break. The larger scales explain the majority of the variability. The scales that separate these two intervals are located at wavelengths of the order of meters to tens of meters. None of the scale breaks in the snow depth spectra were observed in the power spectra of bare ground elevation, or in the spectra of topography + vegetation. Neither the power spectrum exponents nor the scale breaks can be explained based on the power spectrum of the underlying topography and topography + vegetation. On the other hand, the spectrum of vegetation height exhibits very similar behavior as the snow depth spectrum, with a low-frequencies interval with mild slopes, and a high-frequencies interval with steeper slopes. These two intervals are separated by a scale break located at scales of the order of 10 m.

170

When the spectra of snow depth are compared to the spectra of the corresponding vegetation height, two distinct scaling behaviors can be identified. In the areas in which snowfall interception is dominant and snow redistribution by wind is minimal, the scale breaks in the snow depth spectra occur at similar scales as those of the corresponding vegetation. On the other hand, in areas where snow redistribution by wind is dominant, the scale breaks in the snow depth spectra are displaced towards scales larger than those of the corresponding vegetation. Redistribution of snow by wind leads to the formation of snowdrifts and scour areas over larger scales, affecting the scaling characteristics of the snow depth surface after the snow is initially deposited. The scales at which the switch in the scaling properties of snow depth occurs are comparable to the separation distance between peaks (local maxima above a threshold) in the snow depth profiles. These characteristics support the conclusion that the break in the scaling behavior of snow depth is controlled by the vegetation characteristics (e.g., height, area covered by the canopy, and separation between trees) when wind redistribution is minimal and canopy interception is dominant, and by the interaction of winds with features such as surface concavities and vegetation when wind redistribution is dominant. Such effect of wind redistribution is also evidenced in the directional spectra, with the lowest low-frequencies exponents and the largest scale breaks occurring along the predominant wind directions, as sign of scaling anisotropy and directionality in wind-dominated environments. Until this study, evidence of the links between these processes and the scaling behavior observed in the power spectrum of snow depth in these two types of environments had not been provided.

The detailed analysis of the snow depth fields in the sub-alpine forest and alpine tundra environments show how and why differences in the controlling physical processes induced by variations in vegetation cover and wind patterns lead to the observed differences in spatial organization between the snow depth fields of these environments. In the sub-alpine forest area, the mean of snow depth increases with elevation, while its standard deviation remains uniform. In the tundra subarea, the mean of snow depth decreases with elevation, while its standard deviation varies over a wide range. The two-dimensional correlations of snow depth indicate little spatial memory and quasi-isotropic conditions in the forested area, while they show a marked directional bias that is consistent with the predominant wind directions and the location of topographic ridges and depressions in the tundra subarea. The spectral density functions of the snow depth fields follow a bilinear behavior with two scale intervals, each characterized by a different spectral exponent. The locations of the scale breaks in the forested area coincide with those of the vegetation height field, while the breaks in the snow depth scaling are displaced towards larger scales in the tundra subarea with respect to those observed in the corresponding vegetation height field. These observations and the synthetic snow depth fields generated with one- and two-dimensional spectral techniques show that the scale at which the break occurs increases with the separation distance between snow depth maxima, and that the correlation structure of the profiles and fields for the different scale intervals increases with the spectral exponent.

The results obtained using the cellular automata model for simulating wind redistribution of snow illustrate the response of the system to the different processes represented in the model. Simulation results show that the correlation structure of the

172

snow depth fields becomes stronger as the amount of snow transported increases, while the probability distributions of the fields progress from a Gaussian distribution for small transport values to positively skewed probabilities for high transport values. The analysis of the standard deviation of snow depth as a function of the transport volumes indicates a steep increase in the standard deviation at low transport values, while the rate of increase decreases for the higher transport volumes. However, the standard deviation did not reach a stabilization point within the transport volume ranges analyzed. These results indicate that in a given location, changes in wind regimes between seasons induce changes in the statistical properties of the snow depth fields, and that those changes are less significant between seasons with already high transport volumes. The simulation performed using synthetic topography with low relief and meadow vegetation shows that this type of vegetation acts, until fully buried, as a trap for snow directly deposited in the meadow and the snow blown from the upwind bare portions. Also, the snow field in the vegetated area exhibits higher means and a relatively uniform standard deviation, while in the bare areas, the field shows an increase in the standard deviation with time, indicating increases in the variability through time. Additional snow fields simulated using synthetic topography generated to follow a power-law spectrum with slopes similar to the ones observed in the study areas in Colorado reproduce the time and space variations of snow cover properties previously observed in wind dominated environments in several locations. The spatial patterns of the simulated snow depth fields, the anisotropy in the two-dimensional correlation function, and the time progression of the snow cover (i.e., standard deviation as a function of the mean snow depth, and density changes throughout the season) resemble the observations presented in several studies, illustrating the

173

potential of the model for studying the effect of changes in atmospheric conditions (i.e., precipitation, temperature and winds) and physiographic conditions (i.e., topography and vegetation) on the spatial organization of snow cover properties (i.e., snow depth, snow density and SWE) during the accumulation period.

The results obtained in this research have important implications with respect to processes, measurement and model scales. The existence of a break in the scaling of snow depth at scales of the order of meters to tens of meters indicates a switch in the characteristics of the variability above and below the break. Within each scale interval, similar processes are controlling the variability. In forested environments, the location of the scale break is controlled by the separation between trees that induce local minima in the snow surface caused by canopy interception. In environments with significant wind redistribution of snow, the break is associated with the separation between snow drifts and depressions caused by the interactions of the blowing snow with topographic features (e.g., ridges and depressions) and vegetation. If the objective is to reveal small-scale processes such as vegetation interception by individual trees and wind interaction with small features such as surface concavities, trees and rocks, measurement and model scales should be selected within the high-frequency range. In this way, the details of the snow depth surface between the peaks can be revealed. If the objective is to represent the average effect of processes such as canopy interception of snowfall and snow redistribution due to wind, measurement and model scales should be selected within the low-frequency range. For practical purposes in hydrologic applications, accurate description of the small-scale interactions might not be necessary and the detailed information required to reproduce such processes might not be available. Model and

measurement scales should be selected according to such objectives. Also, the simulation results show that the statistical properties of snow depth fields throughout the accumulation period in wind dominated environments depend on the transport volumes of snow, which are dependent on meteorological conditions (e.g., winds and temperature). The inter-seasonal consistency of the spatial organization of snow covers in wind-dominated environments documented in several studies is conditioned to the consistency of wind patterns and wind transport potential. Years with differences in wind regimes and meteorological conditions (e.g., wind speeds and directions, temperatures) will exhibit differences in the spatial statistical properties of snow cover properties (e.g., depth and SWE). The magnitudes of these differences depend on the magnitudes of the differences in the meteorological conditions.

Finally, the research reported here opens future possibilities for the analysis of the variability of snow cover properties over scales between 1 m and 1000 m. This range of scales is of relevance for applications in snowmelt modeling, interpolation of point measurements, remote sensing, and design strategies for measuring and monitoring snow properties, among others. For example, analyses of the subgrid heterogeneity for different grid sizes can be performed using the spectral techniques used for the generations presented in here, given that these techniques allow for reproducing the spectral characteristics observed in the fields of snow depth. Other applications include: extending the processes simulated in the cellular automata model to other types of vegetation that also affect the distribution of snow through the horizontal obstruction of wind flow (e.g., conifer trees), and coupling the model with a snowmelt model to analyze melting

patterns, broadening the time frame beyond the accumulation period through the ablation period.